Earth's core composition and core formation

Rebecca A. Fischer*[1] and William F. McDonough†[2,3,4]

[1]Department of Earth and Planetary Sciences, Harvard University, Cambridge, MA 02138, USA
[2]Department of Geology, University of Maryland, College Park, MD 20742, USA
[3]Department of Earth Science, Tohoku University, Sendai, Miyagi 980-8578, Japan
[4]Research Center for Neutrino Sciences, Tohoku University, Sendai, Miyagi 980-8578, Japan

Wednesday 10th April, 2024

Abstract

The inaccessible and enigmatic core of the Earth comprises 1/3 of the planet's mass, gives rise to the magnetic field, and holds clues to the Earth's formation and the nature of its building blocks. It is comprised mainly of an Fe–Ni alloy, plus ∼10% lighter elements whose identities and abundances remain unknown. Here we describe several distinct approaches to constraining the core's composition. A geo-/cosmochemical approach involves comparing the compositions of the bulk silicate Earth and the Earth's building blocks to determine the core's composition, especially for moderately volatile elements. High pressure–temperature mineral physics data can be used to identify which light elements, at specific abundance levels, are able to match the core's seismic properties (e.g., density, sound velocities, liquidus phase relations). The range of light element contents can also be constrained by incorporating metal–silicate partitioning results into models of Earth's core formation, which offers insight into not only the Earth's core composition but also the conditions and mechanisms of core formation.

Key points/objectives:

- The chemical depletion trend in NC meteorites can be used to constrain the abundances of non-refractory elements in the Earth's core
- Comparing the densities and sound velocities of iron, Fe alloys, and the core gives bounds on the core's light element abundances
- Liquidus phase relations indicate which light element(s) are plausible
- Incorporating metal–silicate partitioning data into core formation models allows for possible ranges of core compositions to be established

*Corresponding author. Email: rebeccafischer@g.harvard.edu
†Email: mcdonoug@umd.edu

Keywords: core composition, light elements, chemical depletion trend, bulk silicate Earth (BSE), Earth = BSE + core, NC meteorites, core density deficit, phase relations, core formation, iron alloys, partitioning, high pressure, equations of state, sound velocities, geoneutrinos

1 Introduction

At 1/2 the radius, 1/3 the mass, and 1/6 the volume of the Earth, the Earth's core is big and important. The convective fluid of the outer core creates dynamo action that generates a protective magnetic shield (magnetosphere) surrounding the planet, which attenuates the flux of harmful cosmic rays and makes the Earth habitable. The core is made up of an Fe–Ni alloy with about 10% of lighter elements, accounting for the density difference between the core and the expected density of Fe–Ni alloy at these conditions (Birch, 1952). There is a sizable, solid inner core (70% of the Moon's radius) that may have started growing early in Earth's history, or more recently (e.g., 1 ± 0.5 billion years ago; Labrosse et al., 2001). Beyond this, details of the core are complicated, and there is no consensus on the light element component.

Determining the core's composition depends on understanding the composition of the bulk silicate Earth (BSE), particularly for the siderophile elements. Once this has been determined, a reasonable estimate of the bulk Earth composition can be established from cosmochemical and meteorite data. Given these steps, the core's composition can be extracted (bulk Earth = BSE + core).

The deeper one goes into the Earth, the greater the uncertainties become regarding our understanding of the nature, structure, and processes of the seemingly inaccessible interior. Knowledge of the nature of the core is based on direct evidence (e.g., seismology, geodesy, paleomagnetism) and indirect evidence (e.g., experimental petrology, mineral physics, geodynamics, geochemistry, cosmochemistry, meteoritics). There are feedbacks between all of these datasets that refine our understanding of the current state and evolution of the Earth's core.

Here we briefly review the seismological, geodetic, and paleomagnetic information about the core. Following that, we discuss the inner core, its crystallization, and the timing of its formation, as well as the energy budget of the core. We review details of compositional modeling of the bulk planet and core with insights from the bulk silicate Earth and cosmochemistry. Section 4 reviews the mineral physics constraints on the core's light element composition based on the core's density, seismic velocities, phase diagram, and other properties. Section 5 discusses the timing and nature of core formation, and how much of each light element may have gone into the core as it was forming. Finally, we finish with a discussion of the prospects in geoneutrino science in section 6.

2 Properties

The Earth is an oblate spheroid with a 21 km difference between its polar and equatorial radii (Table 1) due to hydrostatic equilibrium of gravity at the surface of the Earth and as a function of latitude. In 1914, Beno Gutenberg established the core–mantle boundary (CMB) at 2900 km depth, which is amazingly close the current accepted value (2891 ± 5 km).

2.1 Seismology and geodetics

First order dimensional attributes of the Earth are listed in Table 1, based on fundamental constraints from seismology. The outer core (OC) is liquid (absence of shear waves) and the inner core (IC) is solid,

given observable PKJKP waves (i.e., a type of compressional wave that travels through the mantle and OC, converts to an S-wave as it enters the IC at the inner core boundary (ICB), then converts back to a compressional wave as it leaves the IC). Geodesy documents the planet's moment of inertia (i.e., a dense core surrounded by a less dense silicate shell) (Table 1), whereas the Earth's libration confirms the liquid state of the outer core, as established by seismological observations.

Table 1: **Earth's dimensions**

	Value	Units	Ref	% of planet
Mass				
Earth	$5.97218(60) \times 10^{24}$	kg	1	100%
Inner core	9.68×10^{22}	kg	2	1.6%
Outer core	1.84×10^{24}	kg	2	30.7%
Core	1.93×10^{24}	kg	2	32.3%
Mantle	4.015×10^{24}	kg	1–3	67.7%
Crust (ocean + continental)	$2.73(48) \times 10^{22}$	kg	3	0.46%
Inner core relative to core				5.0%
Radius				
Inner core boundary	1220(10)	km	4	19%
Core–mantle boundary	3483(5)	km	4	55%
Mean radius of the Earth	6371.23(1)	km	1	100%
Polar radius	6357	km	1	
Equatorial radius	6378	km	1	
Volume				
Inner core	7.61×10^{9}	km^3		0.7%
Outer core	1.69×10^{11}	km^3		16%
Core	1.77×10^{11}	km^3		16%
Bulk silicate Earth	9.14×10^{11}	km^3		84%
Earth	1.083×10^{12}	km^3		100%
Moment of inertia				
Equatorial moment of inertia	0.3299765	Ma^2	2	
Mean moment of inertia	0.330690(9)	MR_0^2	1	

[1]Chambat et al. (2010); [2]Yoder (1995); [3]Huang et al. (2013); [4]Masters and Shearer (1995)

PREM (Preliminary Reference Earth Model; Dziewonski and Anderson, 1981) is a 1D seismic reference model for the Earth based on a global evaluation of body waves and free oscillation data. It provides a first-order structure for the mantle (identifying seismic discontinuities that are associated with major phase changes in the Earth's mineralogy) and core, as well as density and velocity profiles for the Earth's interior (Fig. 1). The ak135 model (Kennett et al., 1995) is a spherically-averaged seismic velocity model of the Earth. It was a refinement of the IASP91 model (Kennett and Engdahl, 1991), which was an update of the original 1940s Jeffreys–Bullen Seismological Tables (Jeffreys and Bullen, 1940). The ak135 model is often used as a reference state for the outer core, as the PKP differential travel times are well-resolved, along with density and Q (Montagner and Kennett, 1996), where Q is the quality factor or attenuation factor, the ratio of stored energy to dispersed energy.

The physical properties of the core are listed in Table 2. These properties are derived from seismological data (i.e., density and CMB shape) and interpreted thermodynamic data. The Earth's maximum gravitational acceleration occurs just above the CMB, where being close to the high density core has its greatest effect on the gravity field. The acceleration due to gravity (g) increases in a roughly linear

fashion from the center of the Earth to the CMB (i.e., approximately a uniform density sphere). The excess ellipticity of the core is small (∼0.2 km), and Earth's dynamic figure for the gravitational field is known to six significant figures. The CMB surface is relatively smooth, with a long-wavelength, peak-to-peak topographic amplitude of <4.7 km (Table 2).

Table 2: **Physical properties of the Earth's core**

	Value	Units	Ref
Density (ρ)			
Outermost inner core (solid)	12,830	kg/m^3	1
Innermost outer core (liquid)	12,010	kg/m^3	1
ICB density contrast†	300–1000	kg/m^3	1
Average outer core density	11,160(60)	kg/m^3	1
Average inner core density	13,070(260)	kg/m^3	1
Acceleration due to gravity (g)			
Surface	9.82	m/s^2	2
Above the CMB	10.69	m/s^2	2
At the ICB	4.40	m/s^2	2
CMB shape			
Peak-to-peak topography	<4.7	km	3
CMB ellipticity	∼0.2	km	4
Thermal and pressure data			
Top of the outer core, pressure	136	GPa	
Top of the outer core, temperature	4000(500)	K	5–6
Top of the inner core, pressure	329	GPa	
Top of the inner core, temperature	5350(1000)	K	5–6
Outer core adiabatic gradient	∼0.6	K/km	
Heat flux across the CMB	5–15	TW	7–8
Heat flux across the CMB	30–100	mW/m^2	

[1]Masters and Gubbins (2003); [2]Yoder (1995); [3]Koelemeijer (2021) [4]Sze and van der Hilst (2003); [5]Tsuchiya et al. (2016); [6]Fischer (2016); [6]Lay et al. (2008); [6]Jaupart et al. (2015) †See Section 4 for further discussion.

Seismically-identified anomalous regions of the core include: (1) the outermost outer core (E′ layer in the Jeffreys-Bullen Tables); (2) the F layer of Jeffreys-Bullen, a region at the base of the outer core that immediately surrounds the inner core; (3) the top 1/4 of the inner core, which is anisotropic and shows distinct differences between the eastern and western hemispheres; and (4) the innermost 1/4 to 1/2 of the inner core, which is again seismically distinct. There is no consensus in the seismological literature on these first two anomalous layers. Irving et al. (2018) concluded that their recently constrained model for the outer core did not require an anomalously slow 90–450 km thick layer at the top of the outer core (E′ layer). This does not reject the hypothesis of such a layer, but must give us pause regarding its existence and thickness. One of the challenges for seismologists is to resolve significant structures on the mantle side of the CMB (e.g., Russell et al., 2022), while simultaneously resolving the E′ layer.

2.2 Inner core

Relative to the bulk core, the inner core takes up some 4% by volume and 5% by mass, and it is less dense than pure iron. Thus, it too has a light element component, and, like in the outer core, there are significant uncertainties in the amount and composition of this light element component. Likewise, the

issue of constraining the F layer that surrounds the inner core is also fraught with difficulties for seismologists. Both the ak135 and PREM seismic models do not include an F layer. Identifying the thickness and properties of the F layer is challenging given that fewer normal modes can be used to characterize this region, and also because there are tradeoffs in characterizing this layer versus structures in the inner core. Moreover, there are few body waves that skirt the inner core, adding to this challenge.

The innermost inner core was initially identified by Ishii and Dziewoński (2002), with further evidence and characterization from later studies (e.g., Pham and Tkalčić, 2023). Estimates of its size range from about 1/4 to 1/2 of the inner core radius. The distinctive anisotropic properties of the inner and innermost inner core may be remnants of the core's evolution, including a possible unique early history for the innermost inner core (e.g., Ishii and Dziewoński, 2002).

It is worth considering growth models of the inner core. Ofttimes it has been argued that generation of the Earth's dynamo is not dependent on the presence of an inner core (Landeau et al., 2017; Bono et al., 2019; Frost et al., 2021; Zhou et al., 2022); thus, documentation of an early Earth paleomagnetic record cannot be used to support the early existence of an inner core. Most thermal and paleomagnetic models of core dynamics consider inner core growth to be relatively recent, having started on the order of a billion years ago (Labrosse et al., 2001; Landeau et al., 2017; Bono et al., 2019; Frost et al., 2021). In contrast, some geochemical models had proposed a much earlier start to inner core crystallization (i.e., 2–4 Ga), interpreting Os isotopic compositions of some ocean island basalts as reflecting fractionation of Re/Os and Pt/Os ratios due to inner core crystallization, followed by core contamination of these basalt sources (Walker et al., 1995; Brandon et al., 1998, 2000). However, no supporting evidence has been found from $^{182}W/^{184}W$ isotopic data (Mundl et al., 2017).

A simple example of inner core growth can be calculated with some basic assumptions (Table 3). The model presented here assumes that the inner core began crystallizing and growing about a billion years ago (Labrosse et al., 2001) under continuous homogeneous conditions with exothermic energy production of ~1 TW (Jaupart et al., 2015). This calculation illustrates a potential uniform surface layer growth rate of about a half millimeter per year. Alternatively, focused topographic growth may provide relief to the inner core's surface with a surface gravity field (4.4 m/s^2) that is comparable to that at the surface of Mars (3.7 m/s^2). However, the temperature field and phase boundaries at these pressures may work against production of topographic relief.

Table 3: **Simple continuous growth model for the inner core**

	Value	Units
Growth rate by mass	3.15×10^6	kg/s
Growth rate by volume	240	m^3/s
Growth rate by radius[1]	$3.86t^{1/3}$	m/s
Latent heat of crystallization[2]	320	kJ/kg

[1]where t is time in seconds; [2]assumes 1×10^{12} W generated by core crystallization

2.3 Temperature and geodynamics

Another poorly-constrained property of the core is its thermal structure (e.g., Williams, 2018) (Fig. 1). The two firm pieces of observational evidence constraining the core's temperature are: (1) the convecting mantle's adiabatic gradient, which projects to ~2600 K at ~2800 km depth (i.e., the region just above the core–mantle boundary; Katsura, 2022), combined with the fact that the lower mantle remains mostly below its solidus temperature (approximately ≥3950 K; Pradhan et al., 2015; Pierru et al., 2022); and (2) the inner core is solid and represents a pressure-dependent phase boundary.

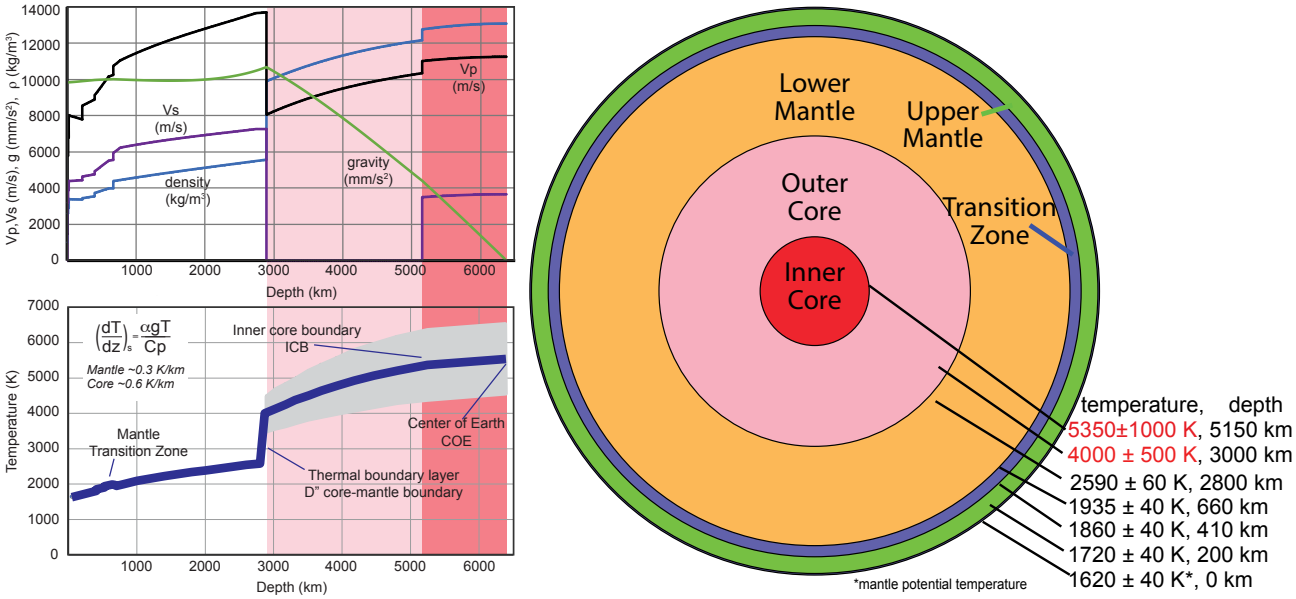

Fig. 1: The PREM density and velocity profiles (Dziewonski and Anderson, 1981), and the approximate thermal structure of the Earth's interior (left panel). The latter is constructed from the silicate Earth temperature data (right panel; Katsura, 2022) and assumptions about core temperatures at the CMB, ICB, and COE (the center of the Earth). The mantle has two thermal boundary layers: the lithospheric lid at the top (not shown; roughly 100–300 km thick) and the D" layer at the base of the mantle, which is approximately 200 km thick. This model assumes whole mantle convection with no compositional boundary layer between the upper and lower mantle, which would otherwise require a third thermal boundary layer. The adiabatic gradient in the core is estimated to be ∼2× that of the mantle.

The lower bound for the ICB temperature is ∼5350 ± 1000 K (Table 2), which is based on a CMB temperature of ∼4000 K and an adiabatic temperature gradient calculated from the equation of state for hcp Fe (Dewaele et al., 2006). This temperature uncertainty estimate is based on systematic and statistical uncertainties associated with experimental temperature measurements, pressure scales, assumed equations of state, and assumptions associated with ab initio calculations. At the ICB, where the solid inner core is crystallizing from the liquid outer core, the temperature should be equal to the core's melting temperature. Though the core is mostly iron, the ICB temperature will be less than the melting point of pure iron, due to melting point depression caused by the core's light element component. An upper bound for the ICB temperature is ∼6400 ± 1500 K, based on experimental constraints of the melting curve for pure Fe at high pressures (e.g., Li et al., 2020a; Turneaure et al., 2020; Kraus et al., 2022). Clearly, our reported core thermal structure reflects our biases, systematic differences between studies, and the challenges inherent in experimental temperature measurements, pressure calibrations, and the detection of melting.

The region between the convective mantle and convective core is a conductive layer at the core–mantle boundary. This conductive boundary layer is likely to have a temperature gradient equivalent to or greater than that of the surface lithosphere, with a sharp rise in temperature of ≥1200 K across the D" layer. This thermal structure is consistent with seismic and petrological observations that find negligible evidence for widespread melting in the deep mantle, although there may be a thin partial melt layer (0–5 km thick) at the base of the mantle (e.g., Russell et al., 2022). At some time earlier in Earth's history, however, melting of the lower mantle may have been significant.

The convective regions of the mantle and core are assumed to have adiabatic gradients ($\left(\frac{\partial T}{\partial z}\right)_S = \alpha g T / C_p$), where T is temperature, z is depth, S is entropy, α is the coefficient of thermal expansion, g is the gravitational acceleration, and C_p is the isobaric heat capacity. The adiabatic gradient of the mantle is ~0.3 K/km throughout most of the mantle, with the upper mantle having a higher gradient (up to 0.5 K/km near the surface; Katsura, 2022). The core's adiabatic gradient is likely to be twice that of the mantle. Assuming outer core temperatures of 4000 K at the CMB and 5350 K at the ICB, the outer core's radial temperature gradient would be ~0.6 K/km (cf. Williams, 2018; Nimmo, 2015).

The heat flux from the core is a function of its initial conditions, conductive cooling (regulated by the surrounding mantle, which insulates the core), energy consumed by dynamo production, exothermic energy of inner core crystallization, and possible radiogenic heat sources. There are many unknowns, which make understanding core geodynamics one of our biggest challenges. Several studies have proposed that there are radioactive heat-producing elements (i.e., K, Th, U) in the Earth's core to help drive the core's dynamo. Chidester et al. (2022) found limited incorporation of some lithophile elements (including K, Th, and U) into the core. However, their experiments produced metal–silicate fractionation between Th and U, and this finding is inconsistent with chemical and isotopic data for a wide range of crustal and mantle rocks; for example, some >23,000 crustal rocks were found to exhibit a narrow range of κ_{Pb} values (see Table 1 and Fig. 3 in Wipperfurth et al., 2018). Likewise, the incorporation of a few to a couple tens of μg/g (or less) of potassium can be accommodated in the core (Corgne et al., 2007; Watanabe et al., 2014). Overall, there appears to be limited evidence for the incorporation of radiogenic elements in the core at levels that would contribute significantly to driving the geodynamo.

Over the last ~15 years, there has been considerable discussion in the literature regarding the electrical and thermal conductivities of core materials (e.g., Zhang et al., 2020; Ohta and Hirose, 2021; see also discussions about the new core paradox in Driscoll and Davies, 2023). The issue remains unresolved with uncertainties of about a factor of two, with significant dependencies on the core's light element composition. The core's electrical and thermal conductivities have a significant influence on its dynamo stability and power. The paleomagnetic record for surface rocks dates back to 3.5 billion years and older for zircons, providing early recordings of the Earth's dynamo action, and it appears to document dynamo action comparable in power and stability over almost all of Earth's history (Tarduno et al., 2020). However, while the paleomagnetic record documents the existence of dynamo action, it does not necessarily indicate the presence of an inner core (Landeau et al., 2017; Bono et al., 2019; Frost et al., 2021; Zhou et al., 2022).

These observations are consistent with current estimates of the core's heat flux of 10 ± 5 TW (Lay et al., 2008; Jaupart et al., 2015); assuming a homogeneous surface flux, this is equivalent to an outer core surface flux of 65 ± 35 mW/m^2 at the CMB. This estimate of the CMB heat flux is comparable to the average surface heat flux for the continents (Lucazeau, 2019). The Earth's heat budget can be expressed as:

$$\begin{array}{lllllllll} {}^{total}Q_{surface\ flux} & = & {}^{core}Q_{cooling} & + & {}^{mantle}Q_{cooling} & + & {}^{mantle}Q_{radiogenic\ heating} & + & {}^{crust}Q_{radiogenic\ heating} \\ 46\ \text{TW} & = & 10\ \text{TW} & + & 16\ \text{TW} & + & 13\ \text{TW} & + & 7\ \text{TW} \end{array} \quad (1)$$

where values for the radiogenic contributions are from McDonough et al. (2020). This equation shows, given uncertainties, that the core and mantle heat fluxes due to secular cooling are sub-equal. If this is the case, then the core's heat flux represents a significant amount of bottom heating of the mantle.

3 Composition of the Earth and its core

Estimating the composition of the Earth's core can be approached from three perspectives: (1) combining geochemical and cosmochemical insights with from mantle samples and meteorites; (2) comparing mineral physics data on core materials with seismological observations for the core (Section 4); and (3) incorporating metal–silicate partitioning data of light elements into models of core formation (Section 5). Here we address the first approach, and show how determining the bulk Earth's composition provides an avenue to determining the core's composition.

Many unknowns remain regarding the core's composition. Given its mostly fluid state, conductive nature, and dynamo generation, it must be a metal that is cosmically abundant (i.e., Fe, and to a lesser extent, Ni). Its chemical and isotopic composition is first and foremost established by comparisons with the compositions of the solar photosphere, chondrites, and the silicate Earth, as these materials represent the reference state, the building blocks, and the complementary component to the bulk planet, respectively.

3.1 Building compositional models of terrestrial planets and their cores

To establish a compositional model for the core of a terrestrial planet, it is essential to understand the the first-order constraints on the properties of the planet and its potential building blocks. Below are the standard rules for planet building:

Bulk silicate Earth

- Define the planet's physical state with rotational and gravitational data and seismic constraints
- Constrain the mantle's potential chemical and isotopic composition using observations and data from the solar photosphere and chondritic meteorites
- Assume chondritic proportions for the refractory elements (elements with half-mass condensation temperatures >1350 K at 10 Pa of hydrogen; e.g., Ca, Al, REEs, etc.)
- Model absolute refractory element abundances based on observed chemical trends from available samples (basalts and peridotites)
- Model the absolute abundances of Mg, Fe, Si, and O, the "non-refractory" major elements; these elements make up >90% by mass (and atomic fraction) of the rocky planets. These elements (except O) have half-mass condensation temperatures of 1300–1350 K at 10 Pa of H
- Define the Mg# (atomic Mg/(Mg+Fe)) and Ni content of the mantle, noting that Mg is concentrated in the mantle and Ni is concentrated mostly in the core, with the planet having a chondritic Fe/Ni = 17.4 ± 0.5 (weight ratio; atomic ratio is 18.3 ± 0.5)
- Model the relative and absolute abundances of moderately volatile elements (elements with half-mass condensation temperatures of ≤1250 K at 10 Pa of H; e.g., alkali metals)

Planet

- Use the composition of the solar photosphere to establish the bimodal compositional difference between the gas giants and rocky planets
- Use observable heliocentric gradients in redox conditions and temperature as a guide
- Define the bulk planet's physical state with rotational and gravitational data and seismic constraints

- Define the relative mass fractions of silicate and metal
- Define the core's density, which then defines its fraction of light elements, depending on an assumed core temperature
- Compare element volatility trends for chondrites with those observed in the BSE for lithophile element abundances
- Establish a volatility trend for siderophile and chalcophile elements in chondrites
- Establish the planet's absolute abundances of Mg, Fe, Si, and O (major elements) and Ca, Al, Ni, and S (minor elements); the eight most abundant elements in chondrites and terrestrial planets

Core

- Define constant siderophile element weight ratios (e.g., Fe/Ni = 17.4 ± 0.5, Ni/Co = 20.4 ± 0.6) in chondrites and apply these principles to the estimating their abundances in the core
- Having defined the chondritic reference trend for the non-refractory, siderophile, and chalcophile elements in the bulk Earth and defined the abundances of these elements in the BSE, then one can establish their abundances in the core
- Subtract the BSE composition from the bulk planet's composition to calculate element abundances in the core

---

A review of the physical state of the Earth was covered in Section 2. In this section, compositional modeling of terrestrial planets is first approached using constraints derived from the solar photosphere and chondrites, the most primitive rocks of the solar system. From this perspective we can establish some constraints using the four most abundant elements in the rocky planets (O, Mg, Si, and Fe). However, we are still left with an important question – which chondrites provide the best analogues for the Earth? This fundamental question remains unresolved.

The sub-group CI1 carbonaceous chondrites have the most primitive composition of the various chondrites. When compared to other chondrite groups, the CI1 type most closely matches the composition of the solar photosphere for all but H, C, N, O, and the noble gases (McDonough, 2016; see also Fig. 5 of Magg et al., 2022 for an updated solar abundance data set and a resolution to the solar metallicity problem). The element abundance curve for the solar photosphere (Asplund et al., 2009; Magg et al., 2022) for at least the most abundant elements (i.e., out to the Fe-peak; elements up to iron that are produced via the alpha process during stellar nucleosynthesis) is comparable to that of other nearby stars in the galaxy (Asplund et al., 2009), and thus the principles developed here are also applicable for building exoplanets.

Taking this approach, we can use the Sun's element abundance curve to understand the chemical fractionation of elements in the Solar System between the volatile element-rich (C, N, O, H, He) gas giant planets and the condensable refractory element-rich (O, Mg, Si, Fe) rocky planets (Fig. 2). The latter planets have an average oxide condensation temperature of ≥1300 K at 10 Pa of H (the inner portion of a protoplanetary disk environment), whereas the former's average condensation temperatures are <200 K (an outer disk region), and together they document a compositional and thermal gradient in the Solar System.

Meteorites are now classified as belonging to either the non-carbonaceous (NC) or carbonaceous (CC) meteorite groups (Trinquier et al., 2007, 2009; Warren, 2011; Kruijer et al., 2017) based on their mass-independent, nucleosynthetic isotopic compositions, which documents radial variations in the distri-

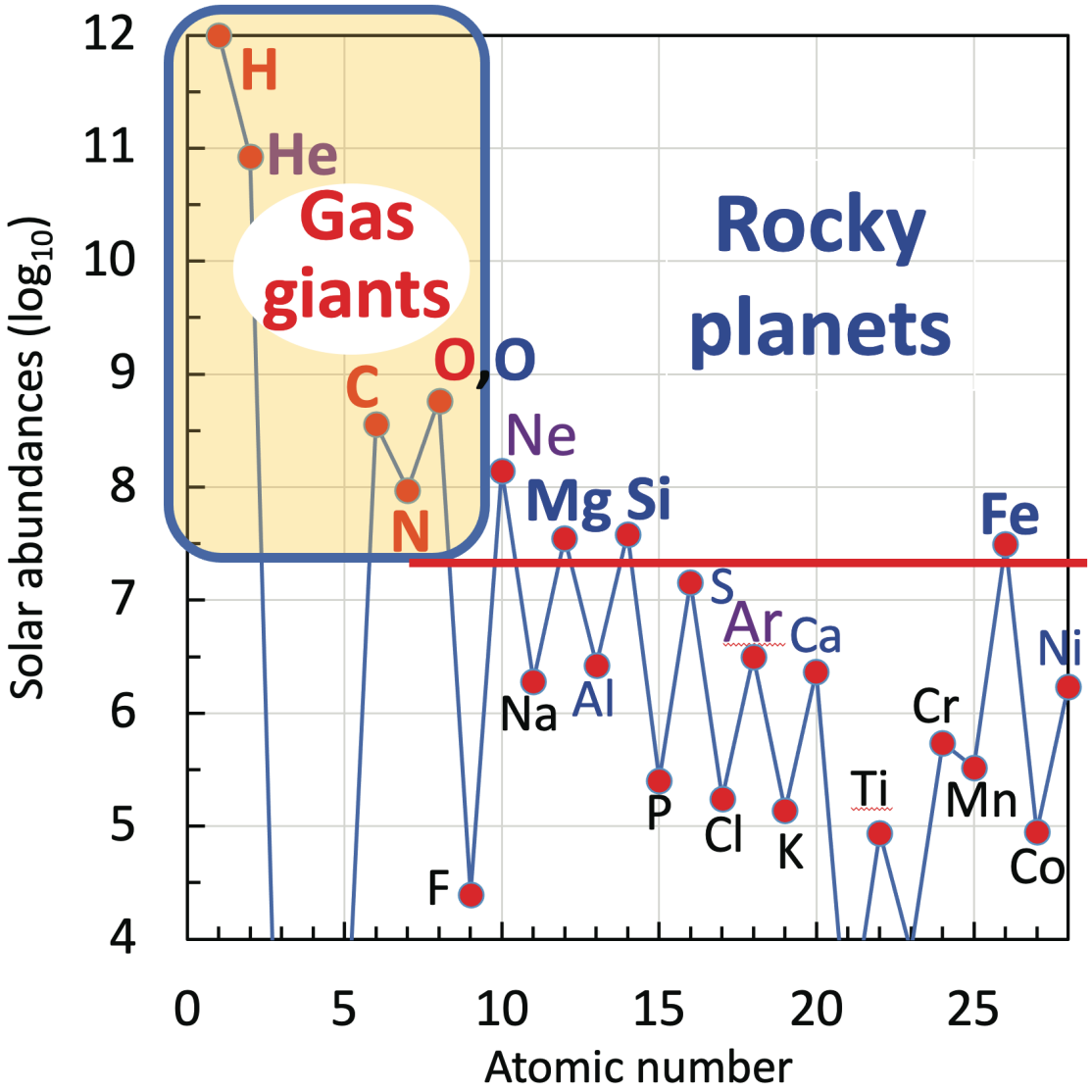

Fig. 2: The solar chemical abundance curve on an astronomical scale. The solar abundance A of an element i is expressed as $A_i = \log_{10}(N_i/N_{\rm H}) + 12$, where N_i is the number of atoms of element i, plotted here as a function of atomic number. This ordinate expresses abundances on a logarithmic scale relative to $N_{\rm H} = 10^{12}$ atoms. Data for He, Li, Be, and B are from Asplund et al. (2009); all other data are from Magg et al. (2022). Noble gases are labeled in purple. The horizontal red line separates the four most abundant elements (O, Mg, Si, Fe) that make up >90 wt% (or atomic%) of the rocky planets, with bold blue labels. The gas giants are predominantly composed of volatile elements (C, N, O, H, He, ±Ne), with bold red or purple labels. For the rocky planets, the next four most abundant elements (Al, S, Ca, Ni) are labeled in blue; together these eight elements make up >99 wt% of these planets.

butions of planetary building materials through the Solar System. The NC group includes ordinary, enstatite, and rumuruti chondrites, most achondrites (e.g., aubrites, mesosiderites, acapulcoites, lodranites, winonaites, brachinites, and ureilites) and some irons, while the CC includes carbonaceous and kakangari chondrites, few achondrites, and some irons. The two isotopically-distinct reservoirs were present in the early Solar System, with NC meteorites most likely coming from the inner Solar System (between the Sun and the asteroid belt), and CC meteorites likely sampling the outer Solar System (from the Trojan asteroids and beyond Jupiter's orbit) (Walsh et al., 2011; Kruijer et al., 2017). Typically, these isotopic distinctions support the concept that the Earth and enstatite chondrites share a dominant

(though not exclusive) genetic heritage, while Mars and ordinary chondrites share a common heritage (e.g., Trinquier et al., 2007, 2009; Javoy et al., 2010; Warren, 2011; Dauphas, 2017).

Chondrites provide plausible models to describe the compositions of the silicate and metal fractions of a planet. However, McDonough and Sun (1995) emphasized that no group of meteorites yet found has a bulk composition matching that of the Earth. Appeals for making the Earth strictly from any one observable chondrite, especially enstatite chondrites (e.g., Javoy et al., 2010), still require some ad hoc additions and subtractions to fit Earth's observable constraints. More recent appeals invoke mixtures of different groups of chondrites to make up the Earth, with a dominance of the enstatite-chondrite-like material (Dauphas, 2017; Piani et al., 2020).

The solar chemical abundance curve (Fig. 2) reveals that O, Mg, Si, and Fe are the most abundant elements (the major elements) in the rocky planets and they are the most abundant condensable elements. These four elements make up more than 90% by mass or atomic fraction of the rocky planets and chondritic meteorites. Together with Ni, S, Ca, and Al (the minor elements), these two groups of elements constitute 99% of the compositions of the rocky planets and chondrites. Such a simple model does not, however, specify the absolute or relative abundances of these two groups of elements (major and minor) or their individual proportions. Fig. 3 shows the compositional variations seen in the Earth, Mars, and NC meteorites (red outlined symbols) and CC (blue symbols) meteorites.

Additional constraints can be placed on these eight abundant elements. Chondritic meteorites, and presumably rocky planets, have a constant Fe/Ni weight ratio of 17.4 ± 0.5 (McDonough, 2014), and this uniformity of Fe/Ni holds despite the vast differences in oxidation states between chondrites (e.g., see Fig. 2b in Yoshizaki and McDonough, 2021). CI and most CM chondrites have no metallic Fe, only oxidized Fe, whereas the opposite is true for EL and EH chondrites, whose silicates are virtually free of Fe. Ca and Al, along with 36 other elements, are refractory and are known to be present in fixed chondritic relative proportions in all chondrites (to within ±15% for the lithophiles (Wasson and Kallemeyn, 1988)). Therefore, knowing the abundance of one of these elements allows one to calculate the abundances of the others. Beyond that, if we know the mantle's Mg# (the Earth's value is 0.89 ± 0.01, based on data from basalts and peridotites (McDonough and Sun, 1995; Palme and O'Neill, 2014)) and the size of the core, we can more narrowly constrain the planet's abundances of Mg, Fe, and Ni. However, there remains a debate over this question – what is the Earth's (mantle and bulk) Mg/Si composition?

3.2 Bulk silicate Earth (BSE)

The BSE includes the solid Earth and hydrosphere minus the core. For models finding similar major element compositions for the upper and lower mantle (i.e., pyrolite; Ringwood, 1991), there is considerable agreement about the element abundances in the primitive mantle (e.g., McDonough and Sun, 1995; Palme and O'Neill, 2014). However, for models that invoke compositional layering in the mantle (e.g., Turcotte et al., 2001; Javoy et al., 2010; Ballmer et al., 2017), there is debate remaining over the BSE's Mg/Si ratio and other compositional details.

It has long been considered by some that the mantle seismic discontinuity at 660 km depth represents not just a phase change, but also a distinct compositional boundary between the upper and lower mantle. If so, this boundary would necessarily have an isolating conductive layer and thus a marked discontinuity in the mantle's thermal gradient. Evidence for this boundary is not forthcoming. Recently, it has been proposed that this compositional boundary layer is instead at 800–1,200 km depth (Fei et al., 2023). In either case, the upper mantle composition is taken to be pyrolitic, while the lower mantle composition is less well established, with the bulk Earth being fitted to either a CI chondrite or enstatite chondrite composition.

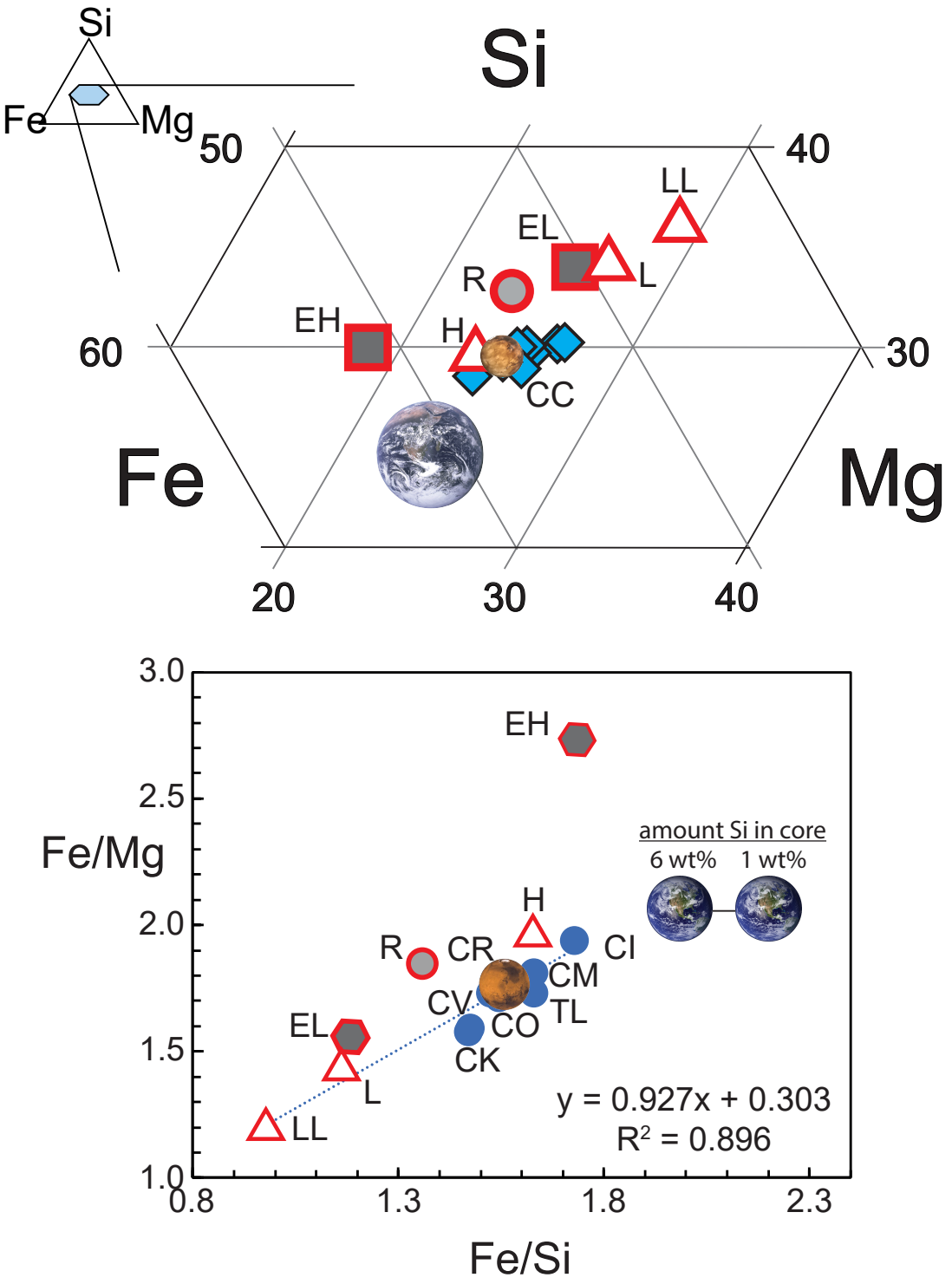

Fig. 3: Major element variations (in wt%) in chondrites, the Earth, and Mars. Blue symbols are CC meteorites and red outlined symbols are NC meteorites, with white, dark grey, and light grey filling representing ordinary, enstatite, and R chondrites, respectively. Note that the compositional model for the Earth plots outside of the range of chondritic meteorites. In the lower figure, we plot two Earth compositional models: one with 1 wt% Si dissolved into the metallic core, and the other with 6 wt% Si. Data for the chondrites are from Alexander (2019a,b). The estimate for the Earth's bulk composition comes from McDonough (2014) and this study. That of Mars is based on Yoshizaki and McDonough (2020), modified to account for the slightly larger martian core (Irving et al., 2023).

Enstatite chondrites are Si-enriched and have a low Mg/Si atomic ratio (0.71–0.93; (Kallemeyn and Wasson, 1986)) relative to CI (1.04 ± 0.02; (Lodders, 2020)) and pyrolitic BSE (1.24 ± 0.02; (McDonough and Sun, 1995)) (Fig. 4). The solar photosphere has a Mg/Si ratio of 0.99 ± 0.09 (Magg et al., 2022). (Note that there is no one "chondritic Mg/Si" value.) Fitting a bulk Earth model to a CI composition with a pyrolitic upper mantle requires having a Si-enriched lower mantle and/or Si in the core. Fitting a bulk Earth model to an enstatite chondrite composition presents even greater challenges, given the larger amount of Si needed in the lower mantle and/or core to offset the low Si content of pyrolite. A striking observation as shown in Fig. 4 is that all NC chondrites plot on the Si-enriched side of the solar photosphere and CI compositions, implying there might be a complementary reservoir on the Si-depleted side (e.g., the Earth).

There are several important aspects to keep in mind regarding the early Solar System, predicting the Mg/Si of planets, and constraining the compositions of planetary building blocks. First, a major consideration is that the problem is 4-dimensional in nature. However, we typically have a simple picture of three spatial dimensions, with some insights on timing. Moreover, while the formation ages of many NC objects (Hellmann et al., 2019) and Mars (Dauphas and Pourmand, 2011) are comparable, the Earth may have formed much later; previous estimates based on the Hf–W isotopic system range from 30 Ma (e.g., Kleine et al., 2002), to 60 Ma (e.g., Touboul et al., 2007), to as late as 160 Ma (e.g., Rudge et al., 2010; Fischer and Nimmo, 2018) (Section 5.3.8). Therefore, NC meteorites and related samples may (or may not) mostly represent the initial 10% of the mass accreted by the Earth (i.e., a Mars mass). Second, Kirkwood gaps in the asteroid belt are locations of orbital resonances with Jupiter, and they tell us that the current meteorite sampling is already biased, given large mass losses associated with these gaps. Third, our temporal bias may or may not be significant. For the most part, our current inventory of meteorites (both falls and finds) came to Earth in the last 10^5 years, with falls (meteorites that were observed falling) being from the last 10^3 years. Among the meteorite falls, the ordinary chondrites represents >80% of the samples. Fortunately, a few older meteorites have been identified in the geological record. And fourth, the Mg/Si ratio was controlled by nebular condensation processes.

Typically, variations in Mg/Si reflect the proportion of olivine (relatively higher condensation temperature; 2:1 Mg:Si by mole) to pyroxene (1:1 Mg:Si) condensed in the protoplanetary disk. Being the higher temperature phase, olivine would condense earlier than an iron–magnesium pyroxene in the inner part of a cooling disk. However, the mass and rate of condensation in the early Solar System are unknown. Spectroscopic studies of accretion disk compositions show that some inner disk regions are richer in olivine (van Boekel et al., 2004), whereas others have more olivine in the outer disk, with differences in disk mineralogy potentially relating to type of star (e.g., T Tauri vs. Herbig Ae/Be stars; Bouwman et al., 2010). In summary, many factors can control a planet's Mg/Si, Fe/Mg, and Fe/Si ratios, and no simple assertion can be made to establish these ratios. For example, the EH chondrite group stands out as being anomalously depleted in Mg (Fig. 3, lower panel); the reason for this depletion is unclear.

There are compelling observations that support whole mantle convection and a simple pyrolite compositional model throughout the Earth's mantle. Although the mantle appears not to be compositionally layered, it contains continental scale and smaller structures (e.g., the LLSVPs and ULVZ, see Garnero et al. (2016)) that seem to be compositionally distinct. The nature and origin of these structures are under discussion. In support of a non-layered mantle compositional model, first and foremost are the abundant tomographic images produced by seismologists of subducting slabs stagnating above, penetrating through, and trapped below the 660 km discontinuity (e.g., Fukao and Obayashi, 2013). These seismic images capture Earth's convective dynamics in action and document mass exchange between the upper and lower mantle, with the ultimate fate for some slabs being transportation to the deepest parts of the lower mantle. Other seismic images capture mantle plumes rising from the base of the mantle up through to about 1000 km depth and spread out as they penetrate the 660 and 410 km seismic

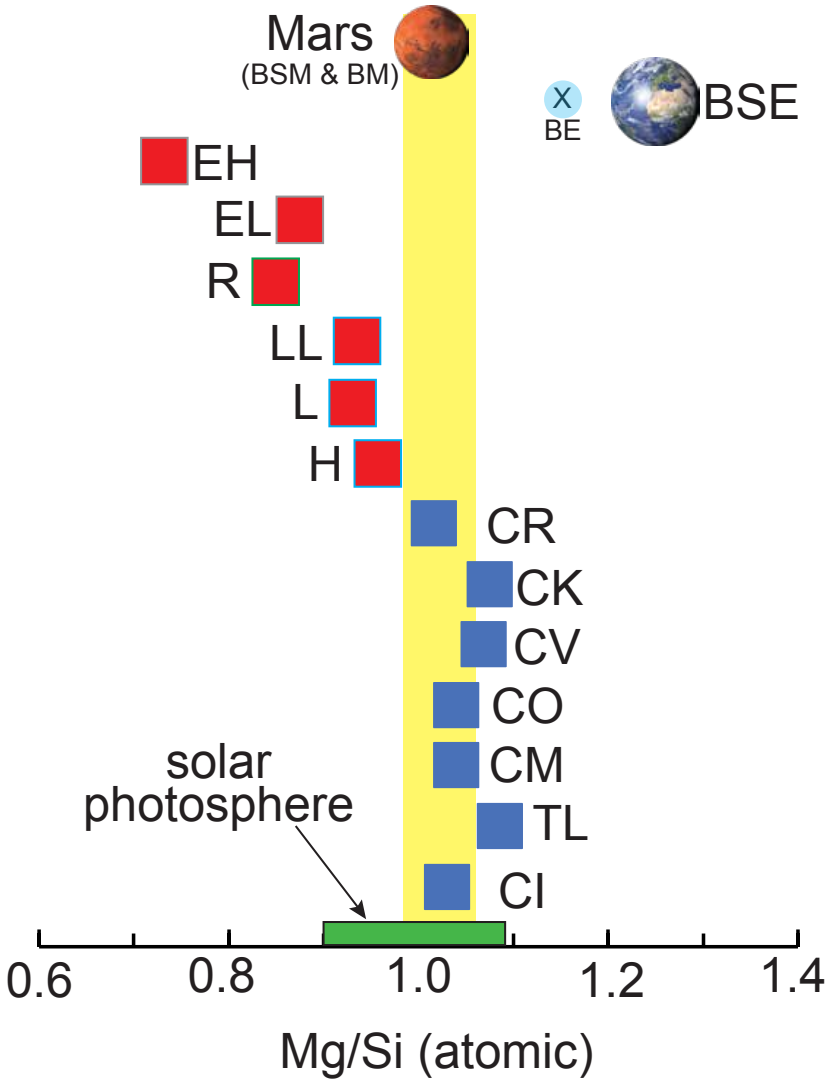

Fig. 4: Mg/Si (atomic) variations in the major chondrite groups, bulk silicate Earth (BSE), and Mars. The bulk Earth's Mg/Si (atomic) is 1.16 (see Table 4) and is identified as light blue circle with an x. The Mg/Si (atomic) value for the solar photosphere is 0.99 ± 0.09 (Magg et al., 2022) and is identified as green box on the axis. Blue symbols are CC meteorites and red symbols are NC meteorites. The Earth and Mars formed in within the inner solar system as did the NC meteorites. The size of each symbol is about the size of its uncertainty. Yellow shaded region is for the compositional range seen CI chondrites. Chondrite labels and data are from Wasson and Kallemeyn (1988) and Alexander (2019a,b), bulk silicate Earth is from McDonough and Sun (1995), and Mars is from Yoshizaki and McDonough (2020). Following Yoshizaki and McDonough (2020), we assume no Si or Mg in the Martian core; thus the bulk silicate Mars (BSM) and bulk Mars (BM) model compositions have the same Mg/Si value.

discontinuities (e.g., French and Romanowicz, 2015). Second, Rudnick and Gao (2014) concluded that the continental crust contains ≥40% of the Earth's budget of K, Th, and U and ≥50% of the most highly incompatible elements. To explain these crustal abundances requires processing much more than the top 27% of the mass of the mantle (i.e., the mantle above 660 km depth). Finally, the latest data from geoneutrino studies indicate that the BSE has 20 TW of radiogenic energy, with 7 TW stored in the continents and the remaining 13 TW stored in the mantle (Sammon and McDonough, 2022). Again these numbers are consistent with a pyrolite compositional model for the BSE.

Given these observations, we adopt the BSE models of McDonough and Sun (1995) and Palme and O'Neill (2014). For many elements, especially the major elements, there are negligible differences between these two models; greater differences exist for Cl, Br, and some of the moderately volatile siderophiles. Disagreements in these latter element abundances are reflected in their estimated uncertainties in both models. We have updated the absolute and relative abundances of the refractory elements in McDonough and Sun (1995) using the CI chondritic reference composition of Lodders (2020) for most elements, and that of Becker et al. (2006) and Fischer-Gödde et al. (2011) for the highly siderophile elements (HSEs: Re, Os, Ir, Pt, Au, Ru, Rh, Pd). Other updates abundances include those of K (Farcy et al., 2020), W (Arevalo Jr and McDonough, 2008), and Th (Wipperfurth et al., 2018). See Table 4 for details.

3.3 Bulk Earth (BE)

Based on the chemical properties and observed BSE abundances of the lithophile elements (i.e., those with metal–silicate partition coefficients of $\ll 0.01$), we conclude that these elements are approximately excluded from the Earth's core and concentrated in the BSE. The refractory lithophile elements (RLEs; e.g., Al) are enriched in the bulk Earth over CI chondrites by a factor of:

$$^{BE/CI}RLE_{EF} = \frac{\mathrm{Al}_{BE}}{\mathrm{Al}_{CI}} = \frac{0.0155\ g/g}{0.00838\ g/g} = 1.85 \tag{2}$$

These elements are enriched in the BSE relative to the bulk Earth and CI chondrites by factors of:

$$\begin{aligned} ^{BSE/BE}RLE_{EF} &= \frac{\mathrm{Al}_{BSE}}{\mathrm{Al}_{BE}} = \frac{0.0229\ g/g}{0.0155\ g/g} = 1.48 \\ ^{BSE/CI}RLE_{EF} &= \frac{\mathrm{Al}_{BSE}}{\mathrm{Al}_{CI}} = \frac{0.0229\ g/g}{0.00838\ g/g} = 2.73 \end{aligned} \tag{3}$$

The enrichment factor (EF) in the first part of equation 3 is equivalent to the mass ratio of mantle/bulk Earth (i.e., enrichment due to core formation). Multiplying this factor times that from equation 2 results in the 2.73 factor for BSE/CI enrichment. The Earth's $^{BE/CI}RLE_{EF}$ of 1.85 is intermediate between that based on H (1.42; Kallemeyn et al. (1989)) and CV (2.00; Kallemeyn and Wasson (1981)) chondrites. Yoshizaki and McDonough (2021) observed that the Earth and Mars are equally enriched in refractory elements (1.9 × CI), with the Earth being more volatile depleted and less oxidized. This refractory element enrichment factor for the bulk Earth establishes the planetary abundances of some thirty refractory lithophile elements and eight refractory siderophile elements (Table 5).

Based on the BSE composition given in Table 4 and the masses of the Earth, bulk silicate Earth, and core (Table 1), we can determine the major element composition of the planet with a few assumptions. Using the Earth's volatility trend for lithophile elements and assuming a chondritic value for the refractory

Table 4: **Compositional models of the bulk silicate Earth (BSE), bulk Earth (BE), and core**

Element	BSE	BE	Core	Element	BSE	BE	Core
H (ppmw)	100	260	600	Rh	0.0012	0.246	0.756
Li	1.6	1.1	0	Pd	0.0071	0.95	2.90
Be	0.060	0.041	0	Ag	0.008	0.15	0.45
B	0.30	0.20	0	Cd	0.04	0.13	0.32
C	120	730	2000	In	0.011	0.011	0.011
N	2	25	75	Sn	0.13	0.41	1.0
O %	44.0	30.0	1.0	Sb	0.0055	0.10	0.31
F	25	17	0	Te	0.012	0.580	1.80
Na	2670	1800	0	I	0.010	0.070	0.20
Mg %	22.8	15.4	0	Cs	0.021	0.014	0
Al %	2.29	1.55	0	Ba	6.520	4.41	0
Si %	21.0	15.3	3.5	La	0.666	0.450	0
P	90	1470	4350	Ce	1.712	1.16	0
S %	0.025	1.12	3.34	Pr	0.260	0.175	0
Cl	17	11	0	Nd	1.289	0.871	0
K	260	176	0	Sm	0.418	0.282	0
Ca %	2.41	1.63	0	Eu	0.158	0.106	0
Sc	15.9	10.7	0	Gd	0.568	0.384	0
Ti	1230	830	0	Tb	0.104	0.070	0
V	82	99	135	Dy	0.688	0.465	0
Cr	2625	4500	8400	Ho	0.154	0.104	0
Mn	1045	1350	2000	Er	0.448	0.303	0
Fe %	6.26	31.9	85.3	Tm	0.071	0.048	0
Co	105	900	2550	Yb	0.456	0.308	0
Ni %	0.196	1.83	5.24	Lu	0.068	0.046	0
Cu	30	98	240	Hf	0.289	0.195	0
Zn	55	80	135	Ta	0.0404	0.027	0
Ga	4.0	6.0	10	W	0.013	0.190	0.55
Ge	1.1	15	45	Re	0.00035	0.0753	0.231
As	0.05	1.6	4.8	Os	0.0039	0.908	2.79
Se	0.075	4.5	14	Ir	0.0035	0.855	2.63
Br	0.050	0.035	0	Pt	0.0071	1.74	5.36
Rb	0.600	0.405	0	Au	0.0017	0.198	0.607
Sr	21.3	14.4	0	Hg	0.010	0.023	0.050
Y	4.10	2.77	0	Tl	0.0035	0.020	0.054
Zr	10.3	6.96	0	Pb	0.150	0.620	1.60
Nb	0.762	0.515	0	Bi	0.0025	0.030	0.09
Mo	0.050	1.80	5.5	Th	0.0819	0.055	0
Ru	0.007	1.27	3.91	U	0.0218	0.015	0

Concentrations reported in ppm by weight unless indicated by %. See text for further details.

Table 5: **Element classification scheme, based on condensation temperatures and chemical affinities**

Lithophile elements	
refractory	Be, Al, Ca, Sc, Ti, V*, Sr, Y, Zr, Nb, Ba, REEs, Hf, Ta, Th, U
	REEs = La, Ce, Pr, Nd, Sm, Eu, Gd, Tb, Dy, Ho, Er, Tm, Yb, Lu
transitional	Mg, Si*, Cr*
moderately volatile	Li, B, Na, K, Mn*, Rb, Cs
volatile	F, Cl, Br, I, Zn
Siderophile elements	
refractory	Mo, W, Ru, Rh, Re, Os, Ir, Pt
transitional	Fe, Co, Ni, Pd
moderately volatile	P, Cu, Ga, Ge, As, Ag, Sb, Au
volatile	Tl, Bi
Chalcophile elements	
volatile	S, Se, Cd, In, Sn, Te, Hg, Pb
Atmophile elements	
highly volatile	H, He, C, N, O, Ne, Ar, Kr, Xe
50% condensation temperatures (K) at 10 Pa	
refractory elements	≥1400 K
transitional elements	∼1250 to ∼1350 K
moderately volatile	∼800 to ∼1250 K
highly volatile	<800 K

**Elements that appear to have been partially siderophile during core formation*

Mo/W ratio of 10.7 (Wasson and Kallemeyn, 1988), we find Fe/Mo = 1.54×10^5 and Fe/W = 1.63×10^6 for the bulk Earth. From this, we establish the planet's Fe content as 31.9 wt%; applying chondritic Fe/Ni and Ni/Co ratios yields Ni and Co contents of 1.83 wt% and 900 ppm, respectively. Likewise, knowing their concentrations in the BSE, we can use a mass balance to calculate the core's composition. Assuming no Mg in the core and the mantle's Mg# of 0.89, we find that the bulk Earth contains 15.4 wt% Mg. The ${}^{BE/CI}RLE_{EF}$ sets the Al and Ca contents in the bulk Earth. Significantly, this approach independently establishes the bulk Earth's Fe/Al = 20, a conclusion previously reached by McDonough and Sun (1995); Allègre et al. (1995).

3.4 The Core

Of the eight elements that account for 99 wt% of the Earth's mass, we have thus far determined the abundances of five (Fe, Mg, Ni, Ca, and Al), leaving three elements (O, Si, and S) whose abundances must be modeled in the bulk Earth and core. These are among the most dominant elements considered to comprise the light element budget of the Earth's core. We recognize that H, C, and perhaps N and other elements might be present in the Earth's interior, but for reasons given below, we consider these highly volatile gases to be trace components in the planet.

The Si, O, and S contents of the core, and hence the bulk Earth, are best estimated by a combination of insights from cosmochemistry, mineral physics (Section 4), and core formation (Section 5). The sulfur content of the planet can be estimated from volatile element depletion trends in NC meteorites (Fig. 5).

A wide range of trace siderophile and chalcophile elements exists in the core, specifically those that are moderately volatile and volatile. In many instances, thermodynamic modeling of the absolute and

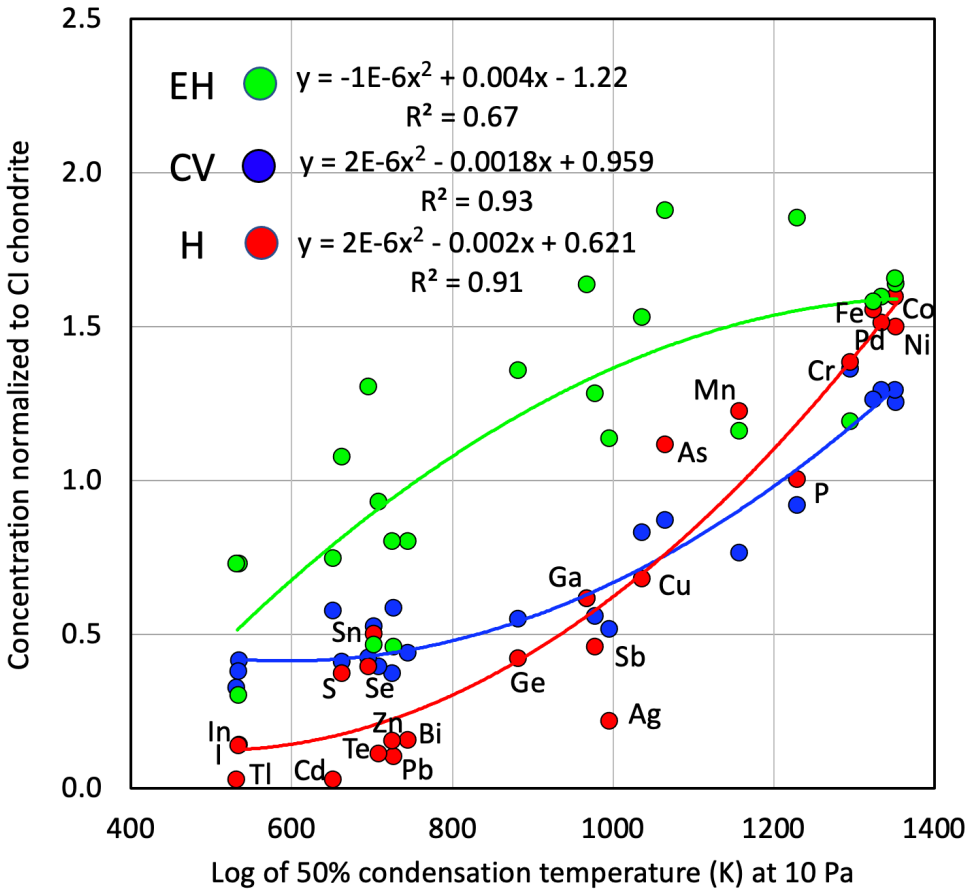

Fig. 5: The half-mass condensation temperatures (Lodders, 2003) versus CI-normalized concentrations for the moderately volatile elements in EH enstatite chondrites (green), CV carbonaceous chondrites (blue), and H ordinary chondrites (red). These are the basis for the siderophile and chalcophile abundance curves for these select chondrites. Data are from Wasson and Kallemeyn (1988). Element labels are given for the H chondrites. Data have been fit with a second order polynomial. Data for Au in chondrites (Fischer-Gödde et al., 2010) have not been included in these regression analyses, as they have CI-normalized values that are markedly enriched relative to their half-mass condensation temperatures.

relative abundances of these elements in the core and mantle have set the limits on the P–T–X–$f\mathrm{O}_2$ (pressure–temperature–composition–oxygen fugacity) conditions of metal–silicate partitioning during core separation (e.g., Wade and Wood, 2005; Corgne et al., 2008).

Estimating the trace element compositions of the bulk Earth and its core requires understanding the chemical systematics of the abundance curves of these elements in chondrites and the BSE. For example, do the NC and CC meteorites display a smooth and continuous decrease in elemental abundances as a function of condensation temperature? The method developed by McDonough and Sun (1995) and McDonough (2014) used only CC meteorites to estimate these trace element abundances, as this method was developed before the introduction of the binary classification of meteorites into NC and CC groups. Given that the NC meteorite group provides a better compositional model for the terrestrial planets, we now present a model based on the chemical systematics seen in the NC meteorites.

Fig. 5 shows the abundance curves for the moderately volatile and volatile, siderophile and chalcophile elements in NC and CC meteorites. The CV (CC-type) and H (NC-type) chondrites have similar depletion trends, whereas EH (and EL, both NC-type) chondrites have a markedly different depletion trend, which is consistent with the enstatite chondrites having formed in a more highly reduced environment

Table 6: **Major element compositional models of the bulk Earth, core, and bulk silicate Earth**

Element	BE	core (wt%)	BSE	Element	BE	core (at%)	BSE
Fe	31.9	85.3	6.3	Fe	15.0	80.0	2.4
O	30.0	1.00	44.0	O	49.5	3.28	58.4
Mg	15.4	0	22.8	Mg	16.7	0	19.9
Si	15.3	3.50	21.0	Si	14.4	6.53	15.9
Ni	1.83	5.24	0.20	Ni	0.82	4.68	0.1
Ca	1.71	0	2.53	Ca	1.13	0	1.3
S	1.10	3.34	0.03	S	0.90	5.46	0.017
Al	1.59	0	2.53	Al	1.55	0	2.0
Co+Cr+P*	0.66	1.46	0.64	Co+Cr+P*	0.0004	0.02	0.002
	99.6	99.8	100.0		100.0	100.0	100.0

**Co, Cr, and P contents were summed for the BE and core, whereas Cr, Na, and Mn contents were summed for the BSE*

(i.e., (C/O) > 0.8–1.0 versus $(C/O)_{solar}$ = 0.52 (Larimer and Bartholomay, 1979)) that allows for the condensation of high temperature sulfides (e.g., oldhamite (CaS). There is no evidence for this highly reduced stage having occurred at any significant level during the accretion of the Earth. For example, early condensation of oldhamite in the proto-planetary disk can quickly lead to non-chondritic ratios of refractory lithophile elements in the BSE, which is not seen in the Earth's mantle geochemical record (Allègre et al., 1995; McDonough and Sun, 1995; Palme and O'Neill, 2014). The lack of isotopic evidence of non-chondritic ratios of La/Ce, Sm/Nd, and Lu/Hf in the BSE demonstrates that the condensation sequence recorded in enstatite chondrites is not applicable to the Earth.

We fit curves to the elemental abundance trends for H and CV chondrites using polynomial, exponential, and power law forms. These calculated compositional models are indistinguishable from one another within the uncertainties of the fits. We chose the fit with the highest R-squared value (i.e., second order polynomial). The compositional model derived from these simple fits (Fig. 5) provides abundance estimates for the moderately volatile, volatile, siderophile, and chalcophile elements in the bulk Earth. Using the bulk Earth and BSE concentrations of these elements, the concentrations of these elements in the core (Table 4) can be determined from a simple mass balance calculation.

With the BSE containing only about 250 ppmw S, the vast majority of the Earth's S budget is contained in the core. Assuming early core formation occurred under reduced fO_2 conditions, and later accretion and core differentiation occurred at more oxidized conditions, our preferred multi-stage model envisages an evolving fO_2. Consequently, our core compositional model as reported in Table 6 reflects this changing fO_2 scenario (see Section 5.4.1 for further details). In this scenario, Si is more strongly partitioned into a core-forming metal liquid under reducing conditions. Later, as the fO_2 conditions become more oxidized, more O is partitioned into the core. Additionally, both Si and O partition more strongly into the core at higher P–T later in the Earth's growth. In this reduced-then-oxidized scenario, both O and Si are incorporated into the core, with more Si than O in the core, though exact numbers are model-dependent. The core composition reported in this section (Table 6) was determined by first setting the amount of S based on the depletion curve, and then setting the relative proportions of Si and O from the guiding principles summarized in Table 12.

Alternative core compositional models exist. For example, Young et al. (2023) developed a model in which hydrogen is the dominant light in the Earth's core. Their model views the Earth as having formed

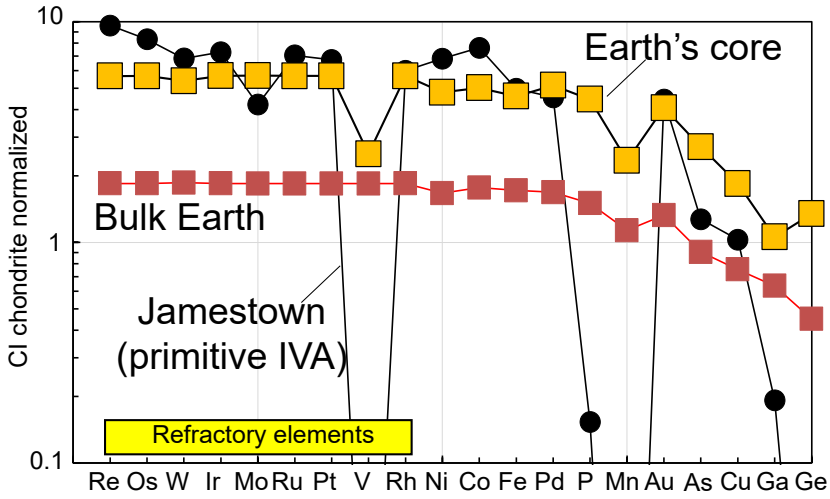

Fig. 6: Comparison between the composition of the bulk Earth, its core, and the most primitive IVA (NC-type) Fe meteorite, Jamestown. Data for Jamestown (black circles) are from McCoy et al. (2011); data for the bulk Earth (red squares) and its core (yellow-orange squares) are from Table 4. Elements are ordered on the horizontal axis following a temperature-dependant scale for half-mass condensation temperatures at 10 Pa of H (Lodders, 2003).

from smaller (Mars-sized) bodies with hydrogen-rich primary atmospheres. They show that reactions with hydrogen-rich atmospheres and metal–silicate equilibrium in magma oceans can explain the Earth's composition.

3.5 Comparisons between the compositions of Earth's core and iron meteorites

Here we compare the composition of the bulk Earth and our estimated composition for the Earth's core with that of iron meteorites, representing candidate core compositions. We chose a primitive sample (Jamestown) from the IVA group, an NC-type iron meteorite. The IVA core is estimated to have a low S content (McCoy et al., 2011; Hilton et al., 2022), comparable to what we have estimated for the Earth.

Fig. 6 shows the CI-normalized composition of Jamestown compared to that of the bulk Earth and its metallic core. The marked depletions in V and Mn seen in the IVA sample reflects more oxidized conditions of its formation (i.e., less V, P, and Mn were incorporated into the segregating metallic phase during core formation, as compared to the behavior of these elements in the Earth). The IVA irons are well established as being depleted in the moderately volatile elements (e.g., Ga and Ge). Although the Earth is depleted in some moderately volatile elements, its depletion is markedly less than that of IVA irons.

For many elements, the match between the Earth's core composition and that of IVA irons is strong (Fig. 6), including the relative depletions of Mo, V, P, and Mn. Hilton et al. (2022) observed that the relative masses of the cores of NC bodies were between 19 and 22%. These core mass fractions are similar to that of Mars (∼23%; Huang et al., 2022; Irving et al., 2023), whereas they differ from that of the Earth, which has a much more massive core (∼33%). McDonough and Yoshizaki (2021) showed that the metallic iron content of terrestrial planets, their core mass fractions, and their uncompressed densities correlate with heliocentric distance, and that these observations follow a simple model of magnetic field strength in the protoplanetary disk. It is possible that midplane transport may have controlled the

distribution of iron outward from the Sun, resulting in decreasing core sizes of the terrestrial planets with increasing radial distance (McDonough and Yoshizaki, 2021).

3.6 Budget of elements in the core

Studies in experimental petrology and mineral physics seek to understand the thermodynamic parameters controlling the distribution of elements between the metallic core and silicate mantle. Hence, a great deal of effort is invested in measuring metal–silicate partition coefficients (equation 20) using experiments that simulate core formation over a range of P–T–X–$f\mathrm{O}_2$ conditions (Section 5.2). Observations from these studies can be used to constrain the conditions under which metal–silicate equilibration and core segregation occurred (Section 5.3). The compositional model shown in Table 4 for the bulk Earth, BSE, and core provides effective average, time-integrated partition coefficients for the bulk metal–silicate system.

Table 7: **Enrichment budget of elements in the core**

% of Earth's inventory in the core		Metal/silicate enrichment factor	
HSEs, Se, Te, Sb, Mo	≥99	HSEs	≥200
Ag, Ge, Bi, As, S, P	≥95	S, Se, Te, Mo, As	45–90
Ni, Co, W, I	≥90	Ag, Sb, P, Ge, W, Bi	17–27
Fe, Pb, Tl, Cd	≥80	Co, I, Tl, Pb	5–12
Cu, Sn, Hg	≥70	Cd, Sn, Cu	∼3.8
Cr, Zn, Ga	≥55	Cr, Ga, Zn, Mn, V	0.8–1.5
Mn, V	≥40		
In	≥30		

In Table 7 we report the mass fraction (in %) of an element's budget that is stored in the core. The metal/silicate enrichment factors listed in Table 7 are effectively the bulk metal–silicate partition coefficients for each element, integrated over Earth's protracted core formation process. Notably, V, Cr, and Mn, along with Zn and Ga, all have bulk partition coefficients close to unity. Ringwood et al. (1990) observed that depletions of V, Cr, and Mn in the BSE could be attributed to their partitioning into a core-forming metal, given their moderately siderophile behaviors at high pressure (e.g., lower mantle) conditions.

Also of note are our predictions for Zn and Ga (Table 7). Previously, McDonough (2014) had predicted wholly lithophile behavior for Ga, using CC chondrites as a guide to determining the abundances of the moderately siderophile elements. However, in the approach used here, Ga is recognized as having a bulk metal–silicate partition coefficient of 1.2 and is sub-equally partitioned between the metal and silicate portions of the Earth. A Ga-bearing metallic core is more compatible with the ubiquitous observations of Ga in iron meteorites.

Zinc has a bulk metal–silicate partition coefficient of ∼1.2, which also represents a revised understanding of the core's composition from using NC chondrite samples to create a compositional model for the Earth. Dreibus and Palme (1996) observed that the zinc content of the Earth's mantle is well-established, proposed that the core is most likely free of Zn, and calculated the bulk Earth's sulfur content (0.56 wt%), from which they concluded that the Earth's core contains 1.7 wt% S. Based on the depletion trend using NC chondrites (Fig. 5), our revised estimates for sulfur in the bulk Earth and core are double those of Dreibus and Palme (1996): 1.1 wt% and 3.3 wt%, respectively (Table 4).

3.7 Uncertainties in the compositional model

Now that we have a compositional model for the core, BSE, and bulk Earth, we need to address uncertainties in these models. Their are two types of uncertainties: statistical and systematic, with the former being easier to assess than the latter. Systematic uncertainties come from the many assumptions made in building the model, whereas the statistical uncertainties can be propagated from the errors in measurements and ratios (e.g., Fe/Ni, Ni/Co, Mg#, and the regression curve used to establish the bulk Earth concentrations of moderately volatile and volatile elements). Given uncertainties in the chondrite compositions, specifically for key elements and their ratios, we assign a ±15% statistical uncertainty for the bulk Earth and core abundances of: Fe, Ni, Co, W, Mo, and the remainder of the refractory elements. For the moderately volatile and volatile elements, specifically the siderophiles and chalcophiles, we assess the statistical uncertainties at ±25% or greater. As a general rule, the more volatile and/or less abundant elements are tougher to constrain.

Uncertainties for the O, Si, and S contents of the bulk Earth and core are among our greatest challenges. The compositional trend for the moderately volatile and volatile elements (Fig. 5) provides a guide for the uncertainty (∼15%) in the S contents of the bulk Earth and core. However, we do not have such a constraint for Si and O. After establishing the abundances of these elements in the BSE (McDonough and Sun, 1995; Palme and O'Neill, 2014), systematic uncertainties dominate their estimates in the bulk Earth and core. Here we have to depend on mineral physics data (Section 4) and experiments and models of core formation (Section 5) to provide insights into the absolute and relative proportions of Si and O in the core. Conservatively, we suggest 25% to 50% uncertainties on their estimated abundances in the core, and proportionally less for the bulk Earth.

3.8 Inner core composition

Assessing the composition of the inner core from geochemical and cosmochemical observations is also challenging, beyond that it is composed of ∼95 wt% Fe–Ni alloy and ∼5 wt% light elements. Seismological data provide constraints on the density jump across the inner core boundary (Fig. 7b; Section 4.3) and document that the inner core has a low shear wave velocity (Fig. 7c; Section 4.2). Geodectic data also constrain the ICB density jump (e.g., An et al., 2023). Beyond these observations, the inner core's composition can be established using a combination of seismology and mineral physics data for appropriate Fe-rich alloys.

The solid inner core is denser than the outer core, as is clear from their relative depths. The inner core represents only 5% by mass and 4% by volume of the bulk core (Table 1). The inner core is about 70% the size of the Moon and may only be ∼1 ± 0.5 billion years old (Labrosse et al., 2001). The pressure at the top of the inner core is 329 GPa and its surface gravity is 4.0 m/s^2, which is only slightly greater than that of Mars (3.7 m/s^2). This pressure represents a phase boundary in pressure–temperature–compositional space. Given this liquid-to-solid phase boundary, it is unlikely that this surface has much topographic relief. The solid inner core likely has an hcp (hexagonal close-packed) crystal structure (Tateno et al., 2010; Fei et al., 2016; Sakamaki et al., 2016) or a mixture of hcp + bcc (body-centered cubic; or similarly, B2) (Belonoshko et al., 2003, 2019, 2022; Vočadlo et al., 2003a; Dubrovinsky et al., 2007; Fischer et al., 2023; Ikuta et al., 2021b).

The amount of light elements in both the inner and outer core depends strongly on core temperature (Anderson and Isaak, 2002), which is one of its most uncertain properties. A higher temperature outer (or inner) core results in a lower light element content needed to match the density deficit (Section 4.1.5). A more detailed understanding of core composition would provide important constraints on the core's thermal structure, since the temperature at the ICB should be equal to the melting point of the core alloy at the ICB pressure, which is strongly dependent on composition. An upper limit on the ICB

temperature is the melting/crystallization temperature for pure Fe (∼6200 K at 329 GPa; Anzellini et al. (2013)) and assuming a conductive thermal gradient (Fischer, 2016). Currently, Fe-rich alloy melting curves extrapolated to 329 GPa span a temperature range of ∼1500 K (Fischer, 2016). Nonetheless, given the uncertainties in the core's light element composition and its corresponding uncertain melting point depression, an ICB temperature of ∼5600 ± 1000 K covers the range of estimates reviewed in Fischer (2016) and incorporates potential systematic uncertainties. Estimates of the density jump ($\Delta\rho$) at the inner core boundary range from about 300 to 1000 kg/m^3 (Fig. 7b). This $\Delta\rho$ implies that the inner core has about half the density deficit of the outer core, and correspondingly it implies that the inner core has approximately half the amount of light elements relative to the outer core. This $\Delta\rho$ constraint, however, does not significantly restrict the compositional range of light elements (Section 4.3; e.g., Hirose et al., 2021).

3.9 Core–mantle exchange

Based on Hf–W and U–Pb isotopic systematics, Earth's core formation is thought to have lasted for a few 10s of Ma to 100–200 Ma after the formation of the Solar System (Stacey and Kramers, 1975; Kleine et al., 2002; Touboul et al., 2007; Rudge et al., 2010; Kleine and Walker, 2017; Fischer and Nimmo, 2018) (Section 5.3.8). Subsequent to this time frame, the core and mantle are assumed to be isolated, essentially having zero or negligible mass transfer. However, the concept of mass exchange (on the order of 0.1% to 1%) between the core and mantle, post-core formation, has been in the literature for more than 30 years (Walker et al., 1995). Some studies have put forth chemical and isotopic evidence as documentation of mass exchange between the core and mantle. In our view, more compelling data would be needed to demonstrate this type of mass exchange, except for perhaps the latest data from the ^{182}Hf–^{182}W isotopic system (Mundl et al., 2017).

McDonough and Sun (1995) observed that ratios involving siderophile/lithophile elements provide the most sensitive tracers of core–mantle exchange. Such ratios leverage compositional contrasts between the core and the bulk silicate Earth. It was further noted that constant ratios of P/Nd, P/Ti, Pd/Ti, W/Ba, W/U, Mo/Ce, Pb/Ce, and others in basalts and peridotites are robust evidence for negligible (i.e., <0.5 wt%) or zero core–mantle exchange (Arevalo Jr and McDonough, 2008; Ireland et al., 2009). Identification of a core–mantle exchange signature in Hawaiian lavas using Fe/Mn (Humayun et al., 2004) is an insensitive measure, because there is only a factor of ∼10 difference between the core and mantle abundances of these elements, whereas W/U, for example, exhibits a factor of ∼10^5 difference in concentration levels (Arevalo Jr and McDonough, 2008).

In the 1990s and early 2000s, the ^{186}Os/^{188}Os isotopic signatures found in some Hawaiian basalts and other ocean island basalts were interpreted as evidence of core–mantle exchange (e.g., Walker et al., 1995; Brandon et al., 1998, 2000). These studies proposed that these lavas had their source regions at the base of the mantle, and that they were incorporating small amounts of differentiated outer core material. In their model, the Os isotopic composition of the outer core had evolved due to early (before 2.5 Ga) inner core growth and differences in the partitioning of Re, Os, and Pt between the inner and outer core. However, Mundl et al. (2017) and subsequent studies have shown that there is no correlation of Os isotopic signatures with anomalous ^{182}W/^{184}W compositions that are of putative core origin. Interpreting the ^{182}W isotope story is not without its own challenges (Walker et al., 2023), however, as these authors note the Os isotopic record does not support core–mantle exchange, given the lack of Os–W isotopic correlations. In addition, evidence for a young age (< 2 Ga) for the inner core is inconsistent with ancient fractionation processes needed to satisfy the Os isotopic story (Section 2.2).

4 Mineral physics constraints on the core's light element composition

Cosmochemical and geochemical evidence suggests a small number of major candidate core light elements: Si, O, S, C, and H (e.g., Section 3; Poirier, 1994; Allègre et al., 1995). They are sufficiently abundant in the Solar System, can alloy with Fe, and are less dense than iron, so that they most likely account for a majority of the core's density deficit. To further constrain the abundances of these elements in the core, one approach is to consider which Fe–light element alloys best match the observed physical properties of the Earth's core.

The physical properties of iron and Fe-rich alloys have been studied at the extreme pressure–temperature (P–T) conditions of Earth's deep interior, using computational methods, large volume presses (LVPs), laser-heated diamond anvil cells (LH-DACs), and shock wave techniques. Some of the alloy properties that are most often compared to those of the core are density, sound velocities, and phase diagram topology, and how they change with pressure and temperature. Here we review the available literature data on these properties and summarize how they can be used to constrain the core's composition.

4.1 Density and equations of state

The Earth's core is less dense than pure iron. This observation may be used to assess the abundances of light elements in the core, provided that we know the density structure of the core, the density of iron at core pressures and temperatures, and how this density changes with the incorporation of different candidate light elements. An Fe-rich alloy with the right abundances of the right combination of light elements should have the same density and compressibility as the Earth's core at the same P–T conditions.

4.1.1 The density of Earth's core

The density structure of Earth's core has been constrained by seismological studies (Fig. 1; Table 2). Some of these models of core density are shown in Fig. 7a. All models report an outer core density of ~9.9–10.0 g/cm^3 at the core–mantle boundary (CMB), increasing with depth to ~12.1–12.3 g/cm^3 at the inner core boundary (ICB). The inner core is more dense than the outer core, both because it is solid and because it has a different composition (Section 4.3). It has a density of ~12.7–12.8 g/cm^3 at the ICB, increasing to ~13.0–13.1 g/cm^3 at the center of the Earth.

There is some disagreement between seismological models of the core's density structure, particularly for the outer core. The models EPOC-Vinet (Irving et al., 2018) and SC-REM (Kemper et al., 2023) have higher densities in the outer core than PREM (Dziewonski and Anderson, 1981) or ak135 (Kennett et al., 1995), for example. In the inner core, PREM has a slightly higher density than SC-REM or ak135, resulting in a different density contrast across the ICB; in general, the reported ICB density contrast has a fair amount of variability across different seismological studies and methods (Fig. 7b; Section 4.3). Seismic approaches can more directly constrain the core's velocity structure than its density structure (Section 4.2), but comparisons to the core's density structure are common due to a greater extent of experimental constraints on the densities of Fe alloys at core P–T.

4.1.2 Equations of state

Equations of state (EoS) are used to describe how a particular phase's molar volume (V) or density (ρ) responds to changes in pressure and temperature. Fitting an equation of state requires a dataset in which P and T were varied and the resulting volume was measured precisely; for example, by using

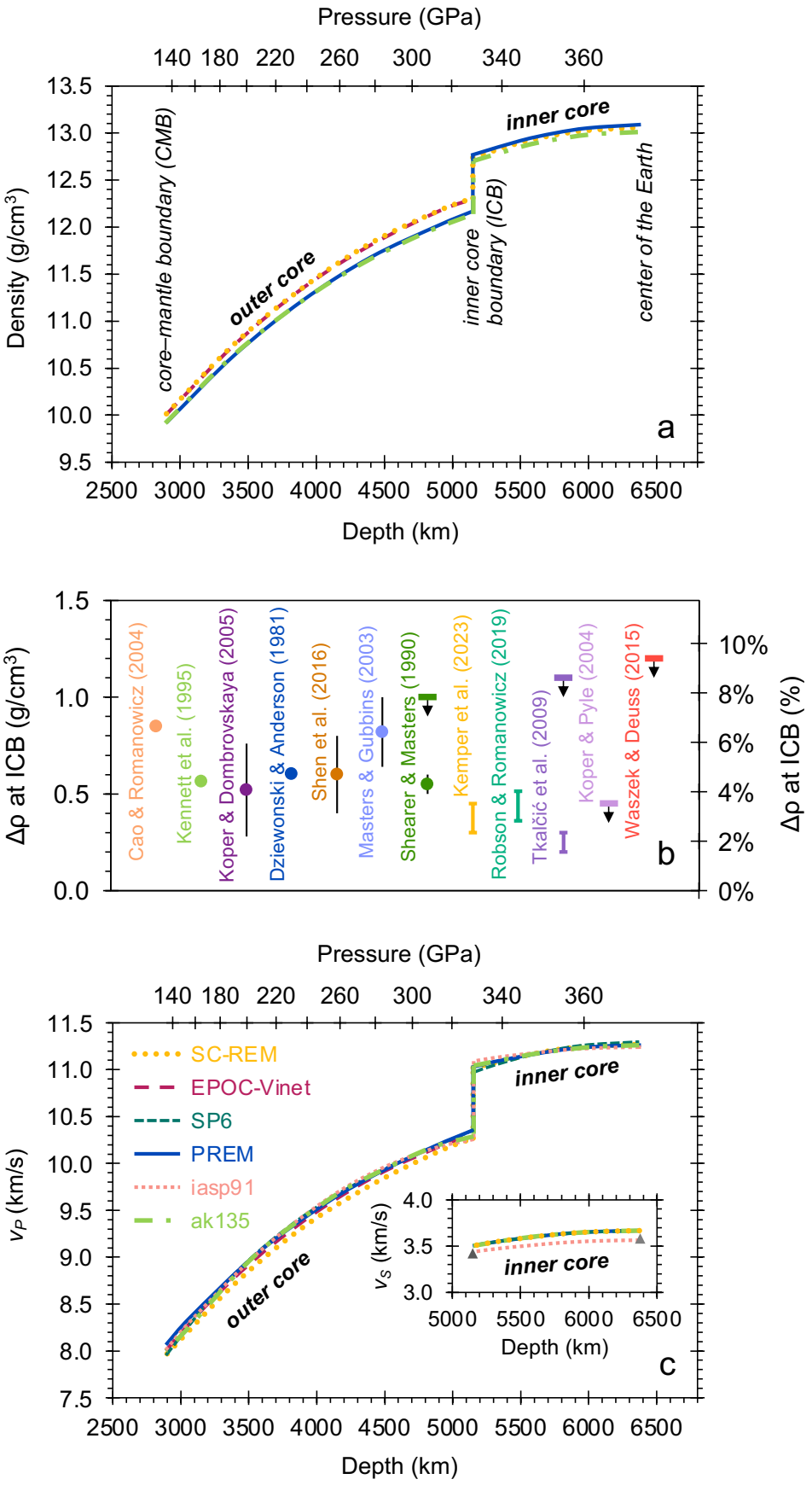
Pressure (GPa)
140 180 220 260 300 340 360
Density (g/cm³)
core–mantle boundary (CMB)
outer core
inner core boundary (ICB)
inner core
center of the Earth
a
Depth (km)
Δρ at ICB (g/cm³)
Δρ at ICB (%)
Cao & Romanowicz (2004)
Kennett et al. (1995)
Koper & Dombrovskaya (2005)
Dziewonski & Anderson (1981)
Shen et al. (2016)
Masters & Gubbins (2003)
Shearer & Masters (1990)
Kemper et al. (2023)
Robson & Romanowicz (2019)
Tkalčić et al. (2009)
Koper & Pyle (2004)
Waszek & Deuss (2015)
b
Pressure (GPa)
v_P (km/s)
SC-REM
EPOC-Vinet
SP6
PREM
iasp91
ak135
outer core
inner core
v_S (km/s)
inner core
Depth (km)
c
Depth (km)

Fig. 7 *(previous page)*: Seismological models of the density and velocity structure of Earth's core. a: Density variations with depth in the core. b: Density contrast between the inner core and outer core at the ICB. Circles are reported values (with uncertainties, if reported), horizontal bars with arrows are upper bounds, and vertical bars are reported ranges. Estimated conversion from g/cm^3 to % is based on an inner core density at the ICB of 12.764 g/cm^3. c: Seismic velocities in Earth's core. Main: v_P variations with depth through the core. Inset: v_S in the inner core. Grey triangles are v_S at the ICB and the center of the Earth from Tkalčić and Phạm (2018). Calculation of pressure from depth is based on PREM (Dziewonski and Anderson, 1981). Different line types/colors correspond to different seismological models: SC-RAM (Kemper et al., 2023), EPOC-Vinet (Irving et al., 2018), SP6 (Morelli and Dziewonski, 1993), PREM (Dziewonski and Anderson, 1981), iasp91 (Kennett and Engdahl, 1991), and ak135 (Kennett et al., 1995). Additional estimates of ICB density contrast are from: Shearer and Masters (1990); Masters and Gubbins (2003); Cao and Romanowicz (2004); Koper and Pyle (2004); Koper and Dombrovskaya (2005); Tkalčić et al. (2009); Waszek and Deuss (2015); Shen et al. (2016); Robson and Romanowicz (2019). Typical uncertainties (as reported in the original studies) are approximately ±0.1–0.2 g/cm^3 for density in the inner and outer core, ±0.2 km/s or less for outer core v_P, ±0.1 km/s or less for inner core v_P, and ±0.05 km/s for inner core v_S (Kennett et al., 1995; Irving et al., 2018; Kemper et al., 2023).

synchrotron X-ray diffraction to measure the volume of a sample in a laser-heated diamond anvil cell or a large volume press as a function of P and T, or by using ab initio methods to recreate this process. In theory, once the equation of state of a phase is sufficiently well-established, it can be used to calculate the density of that material at any P–T. The equations of state of various Fe-rich alloys can be measured experimentally and compared to the seismologically-determined density structure of the Earth's core (Section 4.1.1) to place bounds on core composition. Mie-Grüneisen equations of state, which describe pressure as the sum of an isothermal 300 K pressure (P_{300}) and a thermal pressure component (P_{th}), are most commonly used for this purpose:

$$P = P_{300} + P_{th} = P_{300} + \frac{\gamma}{V}\Delta E \tag{4}$$

where γ is the Grüneisen parameter and $\Delta E = E_{th} - E_{300}$ is the difference in energy between 300 K (E_{300}) and the temperature of interest (E_{th}). Note that while all of these equations are written here relative to isothermal compression at 300 K, as in room temperature experimental measurements, they may also be expressed relative to other temperatures; for example, higher temperatures are sometimes used to describe isothermal compression with external heating, and 0 K is often used in ab initio calculations.

One of the most commonly-used forms for the isothermal pressure is the third order Birch-Murnaghan equation of state (Birch, 1947):

$$P_{300} = 3K_{T0}f\left(1+2f\right)^{5/2}\left[1+\frac{3}{2}\left(K'_{T0}-4\right)f\right] \tag{5}$$

where f is the Eulerian strain:

$$f = \frac{1}{2}\left[\left(\frac{V}{V_0}\right)^{-2/3} - 1\right] \tag{6}$$

K_T is the isothermal bulk modulus, K'_T is its pressure derivative, and a subscript 0 indicates a value at atmospheric pressure. Another widely-used expression for isothermal compression is the Vinet equation

of state (Vinet et al., 1987):

$$P_{300} = 3K_{T0}\left(\frac{V}{V_0}\right)^{-2/3}\left[1-\left(\frac{V}{V_0}\right)^{1/3}\right]e^{\frac{3}{2}\left(K'_{T0}-1\right)\left[1-\left(\frac{V}{V_0}\right)^{1/3}\right]} \tag{7}$$

In both the Birch-Murnaghan and Vinet equations of state, the behavior of the material undergoing isothermal compression can be described by three parameters: V_0, K_{T0}, and K'_{T0}. If the phase is stable or metastable at ambient conditions, its V_0 can be measured directly, leaving only two parameters to fit.

The thermal pressure term, $\frac{\gamma}{V}\Delta E$ in equation 4, can also be expressed in various ways. The Grüneisen parameter is a function of volume:

$$\gamma = \gamma_0\left(\frac{V}{V_0}\right)^q \tag{8}$$

where q is a constant, equal to $\frac{d\ln\gamma}{d\ln V}$. A Debye model of vibrational thermal energy is often used:

$$E_{th} = \frac{9nRT}{(\theta_D/T)^3}\int_0^{\theta_D/T}\frac{x^3}{e^x-1}dx \tag{9}$$

where R is the ideal gas constant, n is the number of atoms per formula unit, and θ_D is the Debye temperature:

$$\theta_D = \theta_0 e^{\frac{\gamma_0}{q}\left[1-(V/V_0)^q\right]} \tag{10}$$

E_{300} can be found by evaluating equation 9 at $T = 300$ K. Alternatively, the Grüneisen parameter may be expressed as:

$$\gamma = \gamma_\infty + (\gamma_0-\gamma_\infty)\left(\frac{V}{V_0}\right)^\beta \tag{11}$$

(e.g., Dorogokupets and Oganov, 2007), where γ_∞ is the Grüneisen parameter at infinite compression and β is a constant. This leads to:

$$\theta_D = \theta_0\left(\frac{V}{V_0}\right)^{-\gamma_\infty}e^{\frac{\gamma_0-\gamma_\infty}{\beta}\left[1-\left(\frac{V}{V_0}\right)^\beta\right]} \tag{12}$$

$$q = \beta\left(\frac{V}{V_0}\right)^\beta\frac{\gamma_0-\gamma_\infty}{\gamma} \tag{13}$$

Using these expressions, we can describe the thermal pressure component as a function of a few parameters: θ_0, γ_0, and q, or θ_0, γ_0, γ_∞, and β, in addition to the three parameters describing the isothermal pressure. Various other formulations of thermal pressure are also widely used (e.g., Dorogokupets and Oganov, 2007). Some are more complex and depend on more parameters, such as those that incorporate contributions from anharmonic and/or electronic thermal energy. Others are more simple, with fewer parameters to fit, such as:

$$P_{th} = \alpha K_T\Delta T = \alpha K_T(T-300\text{ K}) \tag{14}$$

where $\alpha = \frac{1}{V}\left(\frac{\partial V}{\partial T}\right)_P$ is the coefficient of thermal expansion and ΔT is the difference between the temperature of interest (T) and the temperature of the reference isotherm (often 300 K). In this formalism, it is common to assume that αK_T is a constant (e.g., Andrault et al., 1998).

Often, any of these varieties of equations of state can be used to adequately describe a P–V–T dataset. However, the resulting fitted parameters may not be strictly correct for that material due to large tradeoffs between parameters, so it is generally unwise to extrapolate equations of state very far beyond

the data used in the fitting. For this reason, and because experimental measurements at inner core P–T remain very challenging, comparisons of Fe-rich alloy properties are sometimes better made to the outer core. But this approach is also imperfect; the outer core is a liquid, while most measurements of Fe-rich alloy properties are made on solids due to experimental limitations.

The quality of an equation of state depends on several factors, including:

- The P–T range of the data (which is sometimes limited by the stability field of the phase of interest)
- The degree of hydrostaticity of the pressure-transmitting medium used, especially at room temperature
- The quality of the P, V, and T measurements, including the choice of pressure calibration

Even with a high-quality P–V–T dataset, it is often not possible to resolve all ~5–7 (or more) thermal equation of state parameters simultaneously. Common strategies include using measured parameters at ambient conditions (especially V_0) if the phase is stable or metastable, taking some values from previous studies, or fixing $K'_{T0} \equiv 4$ or $q \equiv 1$ to reduce the number of fitted parameters.

4.1.3 The density of pure Fe at core conditions

The equations of state of solid (hcp) and liquid iron have been measured using a variety of experimental and computational approaches. Fig. 8a shows the calculated densities of iron at core pressures using equations of state from several previous studies (Dewaele et al., 2006; Bouchet et al., 2013; Ichikawa et al., 2014; Komabayashi, 2014; Fei et al., 2016; Dorogokupets et al., 2017; Kuwayama et al., 2020). For ease of comparison, all densities are calculated along the same adiabatic temperature profile, where the temperature at each depth increment i (T_i) is given by:

$$T_i = T_{i-1} \left(\frac{V_i}{V_{i-1}} \right)^{-\gamma} \tag{15}$$

using the equation of state of hcp Fe from Dewaele et al. (2006) and a core–mantle boundary temperature of 4000 K, and neglecting any thermal boundary layers.

At CMB conditions of 135.8 GPa and 4000 K, selected equations of state of hcp Fe (Dewaele et al., 2006; Bouchet et al., 2013; Fei et al., 2016) give densities of 11.04–11.17 g/cm^3, while those of liquid Fe (Ichikawa et al., 2014; Komabayashi, 2014; Dorogokupets et al., 2017; Kuwayama et al., 2020) give densities of 10.66–10.84 g/cm^3 (Fig. 8a), corresponding to a density difference between solid and liquid Fe ($\Delta\rho_{solid-liq}$) of 1.8–4.6%. Similar calculations for different depths in the core, as well as for different CMB temperatures, are shown in Table 8. Reported ranges in ρ and $\Delta\rho$ for each set of conditions only reflect the variations between equations of state used, and do not include any other sources of uncertainty.

4.1.4 The core density deficit relative to pure Fe

These densities of pure solid and liquid iron at Earth's core conditions (Fig. 8a, Table 8) can be compared to seismological constraints on the core's density (Fig. 7a) to evaluate the magnitude of the core density deficit (Table 9). While it is clear that there is a significant density deficit relative to pure iron, which is larger in the outer core than in the inner core (in terms of relative densities, expressed at a percentage deficit), there remains considerable uncertainty in the magnitude of the density deficit. This uncertainty is due to uncertainties in the core's thermal structure and density, and the choice of iron equation of state (uncertainties and covariances in equation of state parameters are also significant,

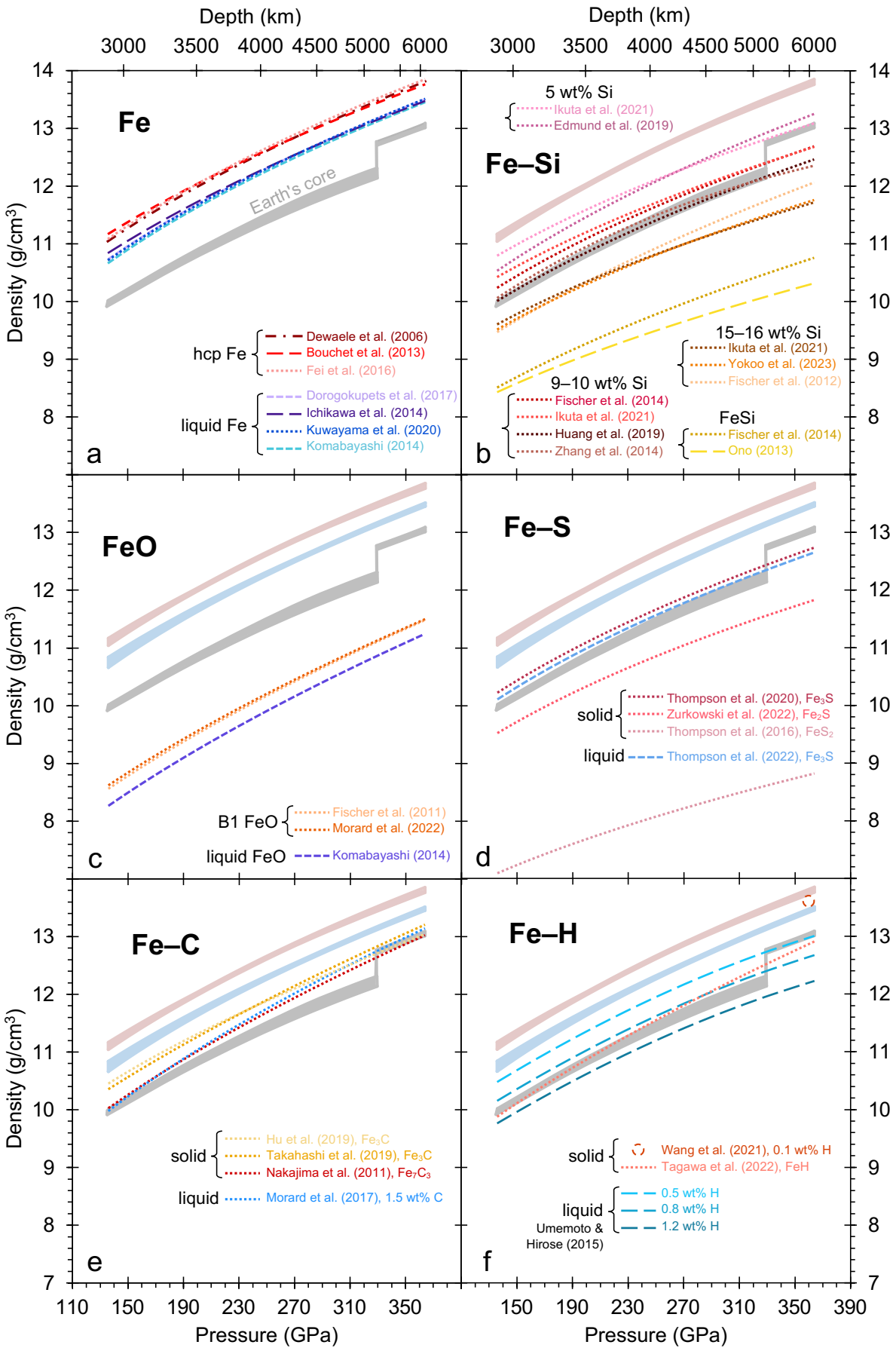
Depth (km)
3000 3500 4000 4500 5000 6000
Density (g/cm³)
Pressure (GPa)
Fe
Earth's core
hcp Fe
Dewaele et al. (2006)
Bouchet et al. (2013)
Fei et al. (2016)
liquid Fe
Dorogokupets et al. (2017)
Ichikawa et al. (2014)
Kuwayama et al. (2020)
Komabayashi (2014)
a
Fe–Si
5 wt% Si
Ikuta et al. (2021)
Edmund et al. (2019)
15–16 wt% Si
Ikuta et al. (2021)
Yokoo et al. (2023)
Fischer et al. (2012)
9–10 wt% Si
Fischer et al. (2014)
Ikuta et al. (2021)
Huang et al. (2019)
Zhang et al. (2014)
FeSi
Fischer et al. (2014)
Ono (2013)
b
FeO
B1 FeO
Fischer et al. (2011)
Morard et al. (2022)
liquid FeO
Komabayashi (2014)
c
Fe–S
solid
Thompson et al. (2020), Fe3S
Zurkowski et al. (2022), Fe2S
Thompson et al. (2016), FeS2
liquid
Thompson et al. (2022), Fe3S
d
Fe–C
solid
Hu et al. (2019), Fe3C
Takahashi et al. (2019), Fe3C
Nakajima et al. (2011), Fe7C3
liquid
Morard et al. (2017), 1.5 wt% C
e
Fe–H
solid
Wang et al. (2021), 0.1 wt% H
Tagawa et al. (2022), FeH
liquid
0.5 wt% H
0.8 wt% H
1.2 wt% H
Umemoto & Hirose (2015)
f

Fig. 8 *(previous page)*: Densities of iron and Fe–light element alloys at core conditions. Densities are calculated from equations of state along an adiabat, with this adiabat determined from the equation of state of hcp Fe (Dewaele et al., 2006) for a CMB potential temperature of 4000 K. Conversion of pressure to depth is based on PREM (Dziewonski and Anderson, 1981). Warmer colors (e.g., pink, red, orange, yellow) represent densities of solid phases, while blue/purple curves represent densities of liquids. Grey shaded regions in all panels indicate the approximate range of core densities reported by different seismological studies (Fig. 7a). Pink shaded regions in panels b–f and blue shaded regions in panels c–f show the approximate ranges of densities for pure hcp Fe and liquid Fe, respectively (from panel a). Most equations of state have been extrapolated in P and/or T, and may be plotted beyond the stability field of the phase. Equations of state are based of data from experiments (dotted curves), ab initio calculations (long dashed curves), combined experimental and ab initio methods (dot-dashed curves), or thermodynamic calculations (short dashed curves). a: Densities of pure hcp iron (Dewaele et al., 2006; Bouchet et al., 2013; Fei et al., 2016) and pure liquid iron (Ichikawa et al., 2014; Komabayashi, 2014; Dorogokupets et al., 2017; Kuwayama et al., 2020). b: Densities of solid Si-bearing alloys with variable silicon contents: 5 wt% Si (Edmund et al., 2019; Ikuta et al., 2021a), 9–10 wt% Si (Fischer et al., 2014; Zhang et al., 2014; Huang et al., 2019; Ikuta et al., 2021a), 15–16 wt% Si (Fischer et al., 2012; Ikuta et al., 2021a; Yokoo et al., 2023), or stoichiometric FeSi (equivalent to 33 wt% Si; Ono, 2013; Fischer et al., 2014). c: Densities of FeO (22 wt% O) in the solid B1 phase (Fischer et al., 2011; Morard et al., 2022) or liquid phase (Komabayashi, 2014). d: Densities of solid Fe_3S (16 wt% S; Thompson et al., 2020), Fe_2S (22 wt% S; Zurkowski et al., 2022), and FeS_2 (53 wt% S; Thompson et al., 2016), and liquid Fe_3S (Thompson et al., 2022). e: Densities of solid Fe_3C (7 wt% C; Hu et al., 2019; Takahashi et al., 2019a), solid Fe_7C_3 (8 wt% C; Nakajima et al., 2011), and liquid Fe–C alloy with 1.5 wt% carbon (Morard et al., 2017). f: Densities of Fe–H compounds: solid Fe–H alloy with 0.1 wt% H (circle symbol at 360 GPa; Wang et al., 2021a), solid stoichiometric FeH (1.8 wt% H; Tagawa et al., 2022), and liquid Fe–H alloys containing 0.5 wt%, 0.8 wt%, and 1.2 wt% hydrogen (Umemoto and Hirose, 2015).

but are not considered here due to inconsistencies in reporting). We neglect the effects of nickel in this analysis; the core likely contains ∼5 wt% Ni (e.g., Table 4). However, this quantity of nickel has an extremely small effect on the density of hcp Fe, perhaps decreasing the density by ∼0.04 g/cm^3 at CMB pressures (e.g., Morrison et al., 2018), well within the uncertainties on the density of pure Fe (Table 8).

For example, comparing lower seismological estimates of the outer core's density (Dziewonski and Anderson, 1981; Kennett et al., 1995) to the density of liquid iron (Ichikawa et al., 2014; Komabayashi, 2014; Dorogokupets et al., 2017; Kuwayama et al., 2020) yields a density deficit of $\frac{\rho_{Fe}-\rho_{core}}{\rho_{core}}$ = 7.5–9.3% at the core–mantle boundary for T_{CMB} = 4000 K, or 6.1–8.5% for T_{CMB} = 4500 K (Table 9). This uncertainty due to temperature is comparable to the uncertainty due to the choice of Fe equation of state (indicated by the ranges). It is also comparable to variations between seismological models; for example, using a higher seismological estimate of the outer core's density (Irving et al., 2018; Kemper et al., 2023) for T_{CMB} = 4000 K decreases the density deficit at the CMB to 6.5–8.3% (Table 9).

The inner core density deficit is constrained to a similar extent, and is smaller than the outer core density deficit. Using an adiabatic temperature profile with T_{CMB} = 4000 K, a comparison between seismological models (Dziewonski and Anderson, 1981; Kennett et al., 1995; Kemper et al., 2023) and hcp Fe equations of state (Dewaele et al., 2006; Bouchet et al., 2013; Fei et al., 2016) implies a density deficit of 5.2–6.4% in the inner core at the ICB (Table 9).

Table 8: **Densities of solid and liquid iron at Earth's core conditions**

Conditions	**hcp Fe ρ** (g/cm^3) references[1]	**liquid Fe ρ** (g/cm^3) references[2]	$\Delta\rho_{solid-liq}$
Core–mantle boundary			
135.8 GPa, 3500 K	11.15–11.26	10.79–10.91	2.2–4.2%
135.8 GPa, 4000 K	11.04–11.17	10.66–10.84	1.8–4.6%
135.8 GPa, 4500 K	10.93–11.07	10.53–10.76	1.6–4.9%
Inner core boundary			
329 GPa, 5350 K[3]	13.44–13.51	13.11–13.17	2.0–3.0%
Center of the Earth			
364 GPa, 5550 K[3]	13.76–13.85	13.45–13.51	1.8–2.9%

[1]Dewaele et al. (2006); Bouchet et al. (2013); Fei et al. (2016); [2]Ichikawa et al. (2014); Komabayashi (2014); Dorogokupets et al. (2017); Kuwayama et al. (2020); [3]Temperature along an adiabat for T_{CMB} = 4000 K, calculated using the equation of state parameters of Dewaele et al. (2006)

4.1.5 Effects of light elements on the density of Fe

Alloying of iron with lighter elements, such as Si, O, S, C, and H, is thought to be responsible for the core's density deficit (Section 4.1.4). Fig. 8b–f shows the densities of Fe–light element compounds calculated from equations of state of various solid and liquid phases, compared to the densities of solid and liquid Fe and the density of the Earth's core. Most of the experimental equations of state shown in Fig. 8 are significantly extrapolated in P and/or T (and are often shown outside the stability fields of these phases), which may at least partly explain the variations in slopes; here we assess how different light elements affect the density of iron at the CMB, to minimize extrapolations.

Fig. 8b highlights density calculations from equations of state of solid Fe–Si alloys (some also containing Ni) with various crystal structures. These alloys have silicon contents ranging from 5 wt% (Edmund et al., 2019; Ikuta et al., 2021a), to 9–10 wt% (Fischer et al., 2014; Zhang et al., 2014; Huang et al., 2019; Ikuta et al., 2021a), to 15–16 wt% (Fischer et al., 2012; Ikuta et al., 2021a; Yokoo et al., 2023), to 33 wt% (stoichiometric FeSi; Ono, 2013; Fischer et al., 2014). Comparing to the density of solid hcp Fe at 135.8 GPa and 4000 K (11.04–11.17 g/cm^3, Table 8; Dewaele et al., 2006; Bouchet et al., 2013; Fei et al., 2016), these Fe–Si equations of state indicate that the addition of 1 wt% Si lowers the density of solid Fe by 0.09–0.10 g/cm^3, on average (standard deviation of 0.02 g/cm^3, range of 0.05–0.13 g/cm^3).

Density calculations for stoichiometric FeO (equivalent to 22 wt% oxygen) are shown in Fig. 8c, based on equations of state of FeO in the solid B1 structure (Fischer et al., 2011; Morard et al., 2022) and the liquid phase (Komabayashi, 2014). Comparing the densities of solid Fe and FeO at the core–mantle boundary (analogous to the previous comparison with Fe–Si alloys), the addition of 1 wt% O decreases the density of solid iron by 0.11–0.12 g/cm^3. Using the density of liquid iron under the same conditions (10.66–10.84 g/cm^3, Table 8; Ichikawa et al., 2014; Komabayashi, 2014; Dorogokupets et al., 2017; Kuwayama et al., 2020), the equation of state of liquid FeO (Komabayashi, 2014) indicates that adding 1 wt% oxygen to liquid Fe lowers its density by the same amount (0.11–0.12 g/cm^3).

Fig. 8d shows the densities of solid Fe_3S (16 wt% S; Thompson et al., 2020), Fe_2S (22 wt% S; Zurkowski et al., 2022), and FeS_2 (53 wt% S; Thompson et al., 2016), as well as liquid Fe_3S (Thompson et al., 2022), at Earth's core conditions. Comparing the densities of solid Fe–S compounds to that of pure Fe at the core–mantle boundary, the addition of 1 wt% sulfur to solid Fe decreases its density by 0.05–0.08 g/cm^3. Equations of state of compounds containing more sulfur imply that S has a larger effect on the density of iron (e.g., density decrease of 0.07–0.08 g/cm^3 per wt% S based on FeS_2 from Thompson

Table 9: **Earth's core density deficit relative to pure iron**

Conditions	Core ρ (g/cm^3)	Fe ρ (g/cm^3)	$\Delta\rho_{Fe-core}$*
Core–mantle boundary			
135.8 GPa, 3500 K, OC	9.92[1], 10.01[2,3]	10.79–10.91[4]	8.8–10.0%[1], 7.8–9.0%[2,3]
135.8 GPa, 4000 K, OC	9.92[1], 10.01[2,3]	10.66–10.84[4]	7.5–9.3%[1], 6.5–8.3%[2,3]
135.8 GPa, 4500 K, OC	9.92[1], 10.01[2,3]	10.53–10.76[4]	6.1–8.5%[1], 5.2–7.5%[2,3]
Inner core boundary			
329 GPa, 5350 K[5], OC	12.15[1], 12.31[2,3]	13.11–13.17[4]	7.9–8.4%[1], 6.5–7.0%[2,3]
329 GPa, 5350 K[5], IC	12.70–12.77[1,3]	13.44–13.51[6]	5.2–6.4%[1,3]
Center of the Earth			
364 GPa, 5550 K[5], IC	13.01–13.09[1,3]	13.76–13.85[6]	5.1–6.5%[1,3]

*The density deficit is calculated as: $\Delta\rho_{Fe-core} = \frac{\rho_{Fe}-\rho_{core}}{\rho_{core}}$; [1]Dziewonski and Anderson (1981); Kennett et al. (1995); [2]Irving et al. (2018); [3]Kemper et al. (2023) [4]Liquid Fe densities calculated from the equations of state of Ichikawa et al. (2014); Komabayashi (2014); Dorogokupets et al. (2017); Kuwayama et al. (2020); reported ranges only reflect differences between studies, and not other sources of uncertainty; [5]Temperature along an adiabat for T_{CMB} = 4000 K, calculated using the hcp Fe equation of state parameters of Dewaele et al. (2006); [6]Solid hcp Fe densities calculated from the equations of state of Dewaele et al. (2006); Bouchet et al. (2013); Fei et al. (2016); reported ranges only reflect differences between studies, and not other sources of uncertainty

et al., 2016; or 0.05–0.06 g/cm^3 per wt% S based on Fe_3S from Thompson et al., 2020), which may be due to differences in crystal structures. The density of liquid Fe_3S at the CMB (Thompson et al., 2022) indicates that adding 1 wt% S to liquid Fe decreases its density by 0.04–0.05 g/cm^3, similar to results based on solid Fe_3S.

Densities of various iron–carbon compounds are shown in Fig. 8e: solid Fe_3C (7 wt% C; Hu et al., 2019; Takahashi et al., 2019a), solid Fe_7C_3 (8 wt% C; Nakajima et al., 2011), and liquid Fe–C alloy containing 1.5 wt% C (Morard et al., 2017). The equations of state of solid Fe–C compounds show that the density of solid iron is decreased by 0.09–0.13 g/cm^3 per wt% C at core–mantle boundary conditions, while that of liquid Fe–1.5C indicates a much larger density decrease per wt% C in liquid iron, possibly due to the large extrapolation required to apply the pioneering equation of state data of Morard et al. (2017) at core conditions.

Fig. 8f illustrates the densities of solid stoichiometric FeH (1.8 wt% H; Tagawa et al., 2022) and liquid Fe–H alloys containing 0.5 wt%, 0.8 wt%, and 1.2 wt% hydrogen (Umemoto and Hirose, 2015) over the conditions of Earth's core, as well as the density of solid Fe–H alloy containing 0.1 wt% H at 360 GPa and 5500 K (interpolated in T from the results of Wang et al., 2021a). Comparing the densities of solid FeH (Tagawa et al., 2022) and Fe at the CMB indicates that adding 1 wt% H to solid Fe lowers its density by 0.65–0.72 g/cm^3, while comparing the densities of solid Fe–0.1H (Wang et al., 2021a) and Fe at 360 GPa and 5500 K yields a density decrease of 1.12–1.88 g/cm^3 per 1 wt% H in solid iron. The equations of state of liquid Fe–H alloys containing 0.5 wt%, 0.8 wt%, and 1.2 wt% hydrogen (Umemoto and Hirose, 2015) imply that the addition of 1 wt% H lowers the density of liquid Fe by 0.36–0.72, 0.62–0.85, or 0.74–0.88 g/cm^3, respectively, at the CMB. The fact that Fe–H equations of state seem to exhibit larger discrepancies between studies than in other Fe–light element systems is perhaps not surprising, given the unique and significant experimental difficulties when working with hydrogen-bearing materials at high P–T.

For a temperature of 4000 K, the outer core density deficit at the CMB is likely in the range of 6.5–9.3%, or 0.65–0.92 g/cm^3 (Table 9), depending on the choice of seismological model and liquid Fe equation of state. At the inner core boundary (329 GPa, 5350 K), the inner core density deficit is similarly 5.2–6.4%,

or 0.67–0.81 g/cm^3 (Table 9). With the simplifying assumption that light elements have similar effects on the densities of solid versus liquid Fe, we can estimate the quantities of various light elements needed to match these outer and inner core density deficits, as shown in Table 10. Since these calculations were performed considering only one light element in the core at a time, which is unrealistic, these values represent the maximum possible abundance of each light element in the core.

Table 10: **Maximum amount of each light element allowed in the core based on density**

Light element X	**$\Delta\rho$/wt% X** (g/cm^3)	**Maximum in OC** 135.8 GPa, 4000 K	**Maximum in IC** 329 GPa, 5350 K
relative to Table 9 values			
Si	0.09–0.10	6.5–10.2 wt%	6.7–9.0 wt%
O	0.11-0.12	5.4–8.4 wt%	5.6–7.4 wt%
S	0.05–0.08	8.1–18.4 wt%	8.4–16.2 wt%
C	0.09–0.13	5.0–10.2 wt%	5.2–9.0 wt%
H	0.36–1.88	0.3–2.6 wt%	0.4–2.3 wt%
relative to PREM[1] *and select Fe EoS*[2]			
Si	0.09–0.10	7.9–8.8 wt%	7.0–7.7 wt%
O	0.11-0.12	6.6–7.2 wt%	5.8–6.3 wt%
S	0.05–0.08	9.9–15.8 wt%	8.7–13.9 wt%
C	0.09–0.13	6.1–8.8 wt%	5.4–7.7 wt%
H	0.36–1.88	0.4–2.2 wt%	0.4–1.9 wt%

[1]Dziewonski and Anderson (1981); [2]Liquid Fe density in OC from Kuwayama et al. (2020), solid Fe density in IC from Dewaele et al. (2006)

The maximum amount of each light element that the core could contain based on its density (considering only one light element at a time) has significant uncertainty, as shown by the large ranges for these upper bounds reported in Table 10. This is primarily due to uncertainties in the magnitude of the core density deficit (Section 4.1.4, Table 9), though uncertainties in each light element's effects on the density of iron can also be considerable, especially for hydrogen. The maximum amounts of each light element in the outer core versus the inner core based on density are extremely similar, due to the similar ranges of density deficits throughout the core when expressed in absolute units (g/cm^3, as opposed to a percentage of the density). The extent of this similarity depends on the choice of seismological model and Fe equations of state; for example, comparing PREM (Dziewonski and Anderson, 1981) to the equations of state of Dewaele et al. (2006) and Kuwayama et al. (2020) leads to different amounts of light elements that match the density deficits in the outer versus inner core (different maximum abundances in Table 10), especially for Si and O.

4.2 Sound velocities

In addition to the density deficit, the Earth's core also exhibits different sound velocities than pure iron. In a similar fashion, the velocities of the core, pure iron, and various Fe–light element alloys can be compared to assess the possible abundances of light elements in the core.

4.2.1 Sound velocity structure of Earth's core

The compressional wave velocity (v_P) structure of Earth's core is shown in Fig. 7c, with the shear wave velocity (v_S) structure of the inner core shown in the inset. These velocities have been constrained by a variety of seismological studies (Dziewonski and Anderson, 1981; Kennett and Engdahl, 1991; Morelli

and Dziewonski, 1993; Kennett et al., 1995; Irving et al., 2018; Tkalčić and Phạm, 2018; Kemper et al., 2023). The outer core has a v_P of 7.94–8.06 km/s at the core–mantle boundary, increasing to 10.26–10.36 km/s at the inner core boundary. The inner core has higher P-wave velocities: 10.97–11.09 km/s at the ICB, increasing with depth to 11.24–11.30 km/s at the center of the Earth. There are no shear waves in the outer core, since the outer core is a liquid; the inner core has a v_S of 3.42–3.51 km/s at the ICB and 3.56–3.67 km/s at the center of the Earth.

4.2.2 Sound velocities of iron at core conditions

Some examples of constraints on the v_P of pure iron are shown in Fig. 9a. This is a so-called "Birch's Law" diagram (Birch, 1961), illustrating a linear relationship between v_P and density that simplifies extrapolations and comparisons between studies. The colored lines are calculated along isotherms for solid hcp Fe from the fit of Ikuta et al. (2022). This fit is based on experimental data from 300 K and some high temperature data up to 3000 K (Antonangeli et al., 2012, 2018; Ohtani et al., 2013; Sakamaki et al., 2016; Ikuta et al., 2022), with velocities obtained using inelastic X-ray scattering (IXS). Sound velocity measurements at high pressures can be made using a wide variety of techniques, and it is not uncommon for different experimental methods to yield contradictory results. This may be at least partly due to differing sensitivities to different material properties; for example, IXS provides a more direct probe of v_P than nuclear resonant inelastic X-ray scattering (NRIXS), with NRIXS being correspondingly more sensitive to v_S (e.g., Antonangeli and Ohtani, 2015). For more details on experimental methods for sound velocity determination, see reviews by Antonangeli and Ohtani (2015), Marquardt and Thomson (2020), and Bommannavar et al. (2022), for example. The IXS results shown in Fig. 9a are consistent with some (e.g., Vočadlo et al., 2009; Martorell et al., 2013b), but not all (e.g., Bouchet et al., 2022), ab initio calculations (Ikuta et al., 2022).

Fig. 9a also shows the range of seismologically-determined compressional wave velocities in Earth's core (from Fig. 7c) for comparison. The isothermal velocities of hcp Fe from Ikuta et al. (2022) have significantly steeper slopes than the core's velocity structure (i.e., v_P of hcp Fe increases more quickly with increasing density than in the core). This is partly due to the temperature gradient through the core; calculating the v_P–ρ curve for hcp Fe along an adiabat with T_{CMB} = 4000 K produces a shallower slope (solid black line in Fig. 9a), more parallel to at least some of the seismological models of inner core v_P structure (e.g., Kennett and Engdahl, 1991). This slope can also be affected by the quality of the v_P data and the equation of state used, the extrapolation in P and T, and the influence of light alloying elements (Section 4.2.3).

At inner core boundary conditions (along an adiabat with T_{CMB} = 4000 K), the v_P of hcp Fe from Ikuta et al. (2022) is lower than that of the Earth's inner core by ~0.4–0.6 km/s. This range is based on variations in seismological models, and it does not include uncertainties in mineral physics measurements, extrapolations, core temperature, or other sources of uncertainty, which can be considerable. The difference between the v_P of hcp Fe and the inner core increases slightly with depth, reaching ~0.6–0.7 km/s at the center of the Earth. This difference may be partly due to experimental limitations on sound velocity measurements at the pressures and temperatures of the inner core, but alloying elements also have a significant effect (Section 4.2.3).

Comparisons to the v_P of liquid iron are more relevant to the outer core, though v_P measurements at core conditions are even more challenging on liquids. In Fig. 9a, the P-wave velocity of liquid Fe along a T_{CMB} = 4000 K adiabat is also shown (black dashed curve), based on the thermodynamic model of Dorogokupets et al. (2017). Its v_P–ρ slope is fairly similar to that of the outer core, with the v_P of liquid Fe being ~0.3–0.4 km/s lower at the CMB and ~0.4–0.5 km/s lower at the ICB.

Fig. 9b shows the v_S of hcp iron at high P–T, compared to seismologically-determined values for the

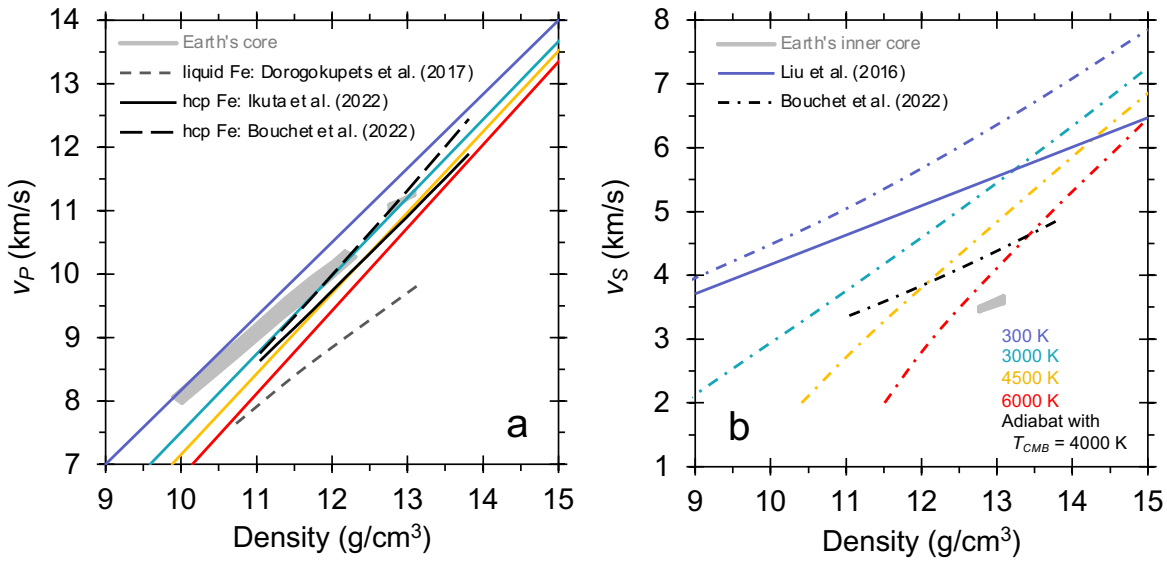

Fig. 9: Compressional wave velocities (v_P) and shear wave velocities (v_S) of iron at high P–T, compared to those of Earth's core. Core velocity bounds (grey shaded regions) are based on those shown in Fig. 7c (Dziewonski and Anderson, 1981; Kennett and Engdahl, 1991; Morelli and Dziewonski, 1993; Kennett et al., 1995; Irving et al., 2018; Kemper et al., 2023), with the conversion from depth to density based on PREM (Dziewonski and Anderson, 1981). Black curves represent the density of iron calculated along an adiabat with T_{CMB} = 4000 K using the equation of state parameters of Dewaele et al. (2006). a: v_P of pure iron at various temperatures, shown as a function of density (Birch's Law diagram; Birch, 1961). Solid colored curves are calculated along isotherms from the fit of Ikuta et al. (2022) for solid hcp Fe, based on experimental data from a variety of IXS studies (Antonangeli et al., 2012, 2018; Ohtani et al., 2013; Sakamaki et al., 2016; Ikuta et al., 2022). Uncertainties in fitted v_P are approximately ±0.2 km/s (Ikuta et al., 2022). Solid curves: Ikuta et al. (2022), hcp Fe, IXS experiments. Long dashed curve: Bouchet et al. (2022), hcp Fe, ab initio calculations. Short dashed curve: Dorogokupets et al. (2017), liquid Fe, thermodynamic model. b: v_S of solid hcp iron at various temperatures. 300 K fit (solid blue curve) is from Liu et al. (2016), based on NRIXS data from Murphy et al. (2013) and Liu et al. (2016). Colored and black dot-dashed curves are v_S of hcp Fe calculated along higher-temperature isotherms and an adiabat, respectively, from the ab initio calculations of Bouchet et al. (2022).

Earth's inner core. The fit to 300 K isothermal data (Liu et al., 2016) is based on NRIXS data from Murphy et al. (2013) and Liu et al. (2016) (which report slightly lower velocities than Gleason et al., 2013). Given the limited temperature range of v_S measurements on hcp iron in the literature, the v_S curves along higher temperature isotherms and a T_{CMB} = 4000 K adiabat were calculated using the ab initio results of Bouchet et al. (2022). The temperature dependence reported by Bouchet et al. (2022) is consistent with that measured experimentally by Lin et al. (2005) at lower P–T.

The v_S of hcp Fe at core densities, even at 6000 K, is significantly higher than the shear velocity of the Earth's inner core (Fig. 9b). As with v_P, the v_S–ρ slope of the inner core is more similar to that of hcp Fe when the velocity of Fe is calculated along an adiabat rather than an isotherm. For ICB conditions of 329 GPa and 5350 K, and an adiabatic temperature profile in the inner core (using equation of state parameters of Dewaele et al., 2006), the Earth's inner core has a slower v_S than pure iron by ∼1.1–1.2 km/s at the ICB, increasing to ∼1.2–1.3 km/s at the center of the Earth (364 GPa, 5550 K) (Fig. 9b).

While the presence of ∼5 wt% Ni in the core alloy has only a small effect on the density of Fe (e.g., Morrison et al., 2018), it may have more significant effects on sound velocities. For example, 300 K

NRIXS measurements indicate that alloying with ∼9 wt% Ni decreases v_S by ∼6% (or equivalently, ∼0.2–0.3 km/s) (Morrison et al., 2019) relative to pure Fe (e.g., Murphy et al., 2013; Liu et al., 2016) (Fig. 10b). Ni also decreases the v_P of iron; for example, Wakamatsu et al. (2018) found that alloying with 5 wt% or 15 wt% Ni lowers v_P by ∼1% or ∼3%, respectively, at 300 K based on femtosecond pulsed laser pump–probe techniques (Fig. 10a). However, the ab initio calculations of Martorell et al. (2013a) indicate that the effects of Ni on the v_S and v_P of hcp iron may nearly disappear at the high temperatures of the Earth's core.

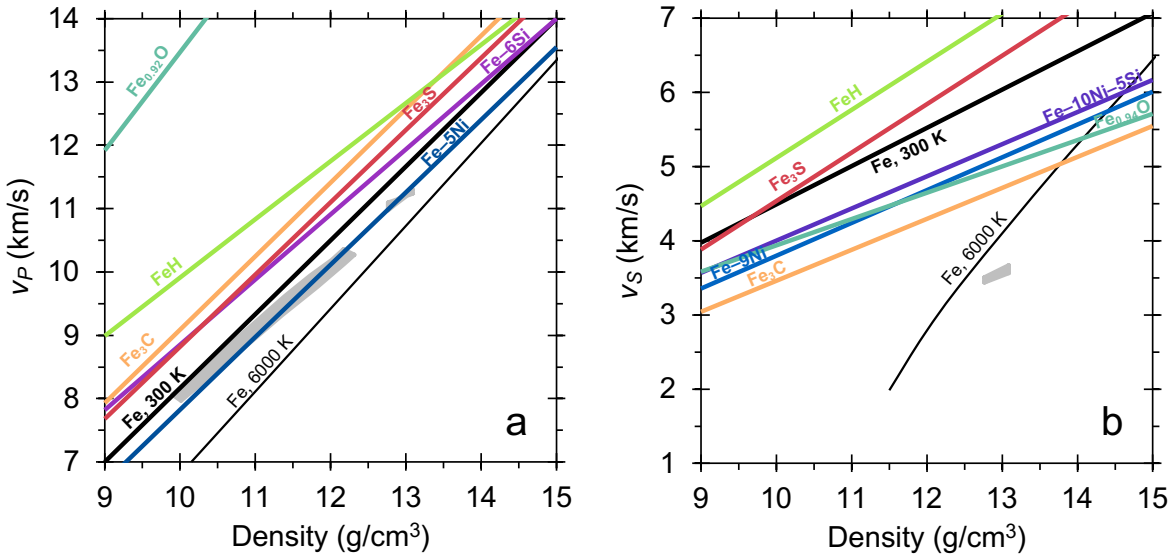

Fig. 10: Compressional wave velocities (a, v_P) and shear wave velocities (b, v_S) of iron alloys at high P and 300 K, compared to those of pure iron and the Earth's core. Core velocity bounds (grey shaded regions) are based on those shown in Fig. 7c (Dziewonski and Anderson, 1981; Kennett and Engdahl, 1991; Morelli and Dziewonski, 1993; Kennett et al., 1995; Irving et al., 2018; Kemper et al., 2023), with the conversion from depth to density based on PREM (Dziewonski and Anderson, 1981). Bold black lines: Fe at 300 K (Bouchet et al., 2022; Ikuta et al., 2022). Thin black lines: Fe at 6000 K (Bouchet et al., 2022; Ikuta et al., 2022). Bold colored lines are velocities of various Fe alloys at 300 K. Blue: hcp Fe–Ni alloys with 5 wt% Ni (v_P; Wakamatsu et al., 2018) or 9 wt% Ni (v_S; Morrison et al., 2019). Purple: hcp Fe–Si(–Ni) alloys with 6 wt% Si (v_P; Sakairi et al., 2018) or 5 wt% Si and 10 wt% Ni (v_S; Morrison et al., 2019). Teal: $Fe_{1-x}O$ with $x = 0.08$ (24 wt% O, v_P; Tanaka et al., 2020) or 0.06 (23 wt% O, v_S; Wicks et al., 2017). Red: Fe_3S (16 wt% S). v_P is from Kamada et al. (2014), v_S is from Lin et al. (2004) with densities calculated from the equation of state of Thompson et al. (2020). Orange: Fe_3C (7 wt% C). v_P is from Takahashi et al. (2019b), v_S is from Chen et al. (2018). Lime green: FeH (∼1.8 wt% H). v_P is for the non-magnetic dhcp phase (Shibazaki et al., 2012), while v_S is for the fcc phase (Thompson et al., 2018). Many of the lines shown in this figure have been extrapolated significantly beyond the coverage of experimental data.

4.2.3 Effects of light elements on the sound velocities of Fe

Fig. 10 shows the effects of candidate core light elements Si, O, S, C, and H on the v_P and v_S of iron at 300 K. For each Fe–light element binary material, its v_P–ρ and v_S–ρ relationships are plotted as straight lines (Birch's Law plot; Birch, 1961). These lines are either fits reported by the original studies or refit to their data, and most are extrapolated significantly. In general, IXS studies were favored for v_P measurements, and NRIXS studies were favored for v_S measurements (e.g., Antonangeli and Ohtani, 2015). These measurements were all made on solids; they cannot be directly applied to the liquid

outer core, while applying them to the solid inner core requires a very large extrapolation in density (or pressure) as well as temperature. Many of these materials likely have different crystal structures at the pressures, temperatures, and compositions of the Earth's core. However, despite these limitations, experimental high pressure sound velocity measurements on Fe–light element compounds (Fig. 10) may provide important insights into the direction and relative magnitude of each light element's effects.

Table 11 lists the 300 K linear v_P–ρ and v_S–ρ fits shown in Fig. 9–10 for pure iron and various Fe–light element alloys. Many Fe–light element binary materials have not been studied using these techniques at high temperatures (with a few exceptions; e.g., Sakairi et al., 2018; Takahashi et al., 2019b; Tanaka et al., 2020). Due to a general dearth of high temperature sound velocity data, the temperature dependencies of these materials' velocities were sometimes approximated by previous studies as being the same as that of pure Fe (e.g., Chen et al., 2018), or as following a linear velocity–ρ relationship independent of temperature (e.g., Prescher et al., 2015), or as having various imposed linear temperature dependencies (e.g., Thompson et al., 2018), while many studies restricted comparisons with pure iron to 300 K (e.g., Kamada et al., 2014; Morrison et al., 2019).

Table 11: **Velocity–density systematics for iron and Fe–light element alloys at 300 K**

Material and reference	$\boldsymbol{v_P}$ (km/s)[1]	**Material and reference**	$\boldsymbol{v_S}$ (km/s)[1]
Fe (Ikuta et al., 2022)	$1.162\rho - 3.450$	Fe (Liu et al., 2016)	$0.46\rho - 0.43$
Fe–6Si (Sakairi et al., 2018)	$1.030\rho - 1.45$	Fe–9Si (Morrison et al., 2019)[2]	$0.433\rho - 0.334$
$Fe_{0.92}O$ (Tanaka et al., 2020)	$1.55\rho - 2.03$	$Fe_{0.94}O$ (Wicks et al., 2017)[2]	$0.355\rho + 0.389$
Fe_3S (Kamada et al., 2014)	$1.14\rho - 2.58$	Fe_3S (Lin et al., 2004)[2,3]	$0.653\rho - 1.997$
Fe_3C (Takahashi et al., 2019b)	$1.16\rho - 2.51$	Fe_3C (Chen et al., 2018)[2]	$0.418\rho - 0.716$
FeH (Shibazaki et al., 2012)	$0.92\rho + 0.71$	FeH (Thompson et al., 2018)[2]	$0.649\rho - 1.371$

[1]Velocity equations are for densities in units of g/cm^3; [2]Refit to the data of that study; [3]Pressure–density conversion based on the equation of state of Thompson et al. (2020)

These sound velocity measurements can be used to constrain the core's composition, because the correct mixture of pure Fe plus Fe–light element alloys that matches the core's composition should be able to reproduce the density, v_P, and v_S of the core at every depth. Many previous studies have considered a linear mixing model for Fe and one Fe-alloy by solving the following system of equations:

$$\rho_{core} = t\rho_{alloy} + (1-t)\rho_{\mathrm{Fe}} \tag{16}$$

$$v_{core} = \frac{v_{alloy}v_{\mathrm{Fe}}}{(1-t)v_{alloy} + tv_{\mathrm{Fe}}} \tag{17}$$

where ρ_{core}, ρ_{Fe}, and ρ_{alloy} are the densities of the Earth's core (constrained by seismology), pure Fe, and an Fe–light element alloy, respectively, at the same conditions; v_{core}, v_{Fe}, and v_{alloy} are the corresponding sound velocities (either v_P or v_S); and t is the volume fraction of the alloy (Badro et al., 2007; Fiquet et al., 2009; Shibazaki et al., 2012).

However, with disagreements between studies and methods, data spanning a limited pressure range, limited data on liquids (cf. e.g., Nakajima et al., 2015), a poor understanding of the effects of high temperatures, and uncertainties in the properties of pure Fe and the Earth's core, this type of calculation cannot place definitive constraints on core composition at this time. Future studies that address these limitations may allow for greater insights into the composition of the core, especially through combining sound velocity data with the other approaches discussed in this chapter.

4.3 Liquidus phase relations

The density structure of the Earth's core (Fig. 7a) shows an abrupt increase at the ICB. Seismological studies of core density differ in the exact magnitude of this density jump, with most reporting values in the range ∼0.5–0.9 g/cm^3 (or equivalently, ∼4–7%) (Fig. 7b). A portion of this density jump is due to the fact that the inner core is a solid, while the outer core is a liquid, and solids are typically denser than liquids of the same composition under the same conditions. However, this $\Delta\rho_{melting}$ is not sufficient to explain the observed density increase. For example, comparing densities from several equations of state of hcp and liquid Fe obtained using a variety of methods (Dewaele et al., 2006; Bouchet et al., 2013; Ichikawa et al., 2014; Komabayashi, 2014; Fei et al., 2016; Dorogokupets et al., 2017; Kuwayama et al., 2020) implies that iron has a $\Delta\rho_{melting}$ of only ∼2.0–3.0% at ICB conditions (329 GPa, 5350 K; Table 8). Fig. 11 summarizes estimates of the $\Delta\rho_{melting}$ of Fe from several previous studies (Laio et al., 2000; Alfè et al., 2002c; Vočadlo et al., 2003b; Komabayashi and Fei, 2010; Luo et al., 2011; Dorogokupets et al., 2017), which indicate values of 1.1–2.3%. The $\Delta\rho_{melting}$ of Fe is thought to not be significantly affected by alloying with a geochemically-relevant quantity of nickel (e.g., Alfè et al., 2002a).

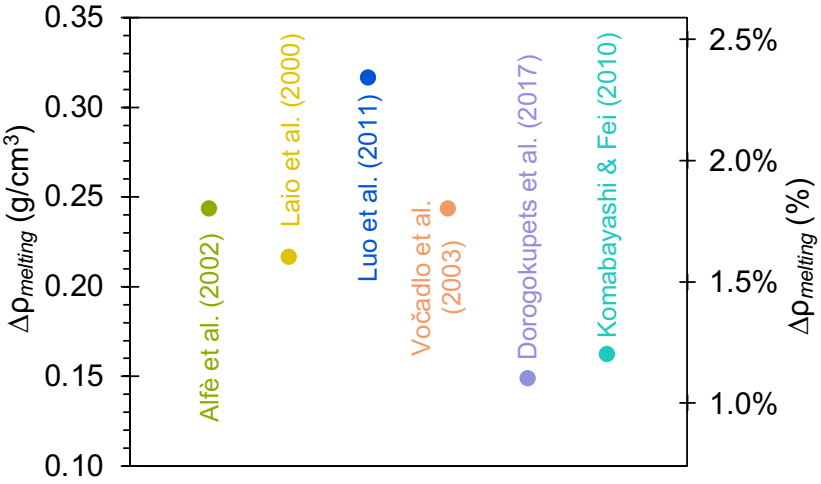

Fig. 11: Previous results on the density change upon melting for pure Fe at the ICB pressure (329 GPa). Most studies report $\Delta\rho_{melting}$ as a percentage change (right axis); the estimated values for absolute density change (in g/cm^3, left axis) were calculated using a density of hcp Fe of 13.47 g/cm^3 at 329 GPa and 5350 K (Dewaele et al., 2006). Some of the $\Delta\rho_{melting}$ values shown here are based on ab initio calculations (Laio et al., 2000; Alfè et al., 2002c; Vočadlo et al., 2003b; Luo et al., 2011), while others are based on thermodynamic modeling of experimental datasets (Komabayashi and Fei, 2010; Dorogokupets et al., 2017).

The larger density jump at the Earth's inner core boundary can be reconciled with the smaller $\Delta\rho_{melting}$ of Fe(–Ni) if the core's light elements are present in higher abundances in the outer core than in the inner core. This implies that as the core cools over time and the inner core crystallizes, the core's light elements are preferentially partitioning into the liquid outer core. They are released at the ICB, where they rise buoyantly and drive compositional convection in the outer core, providing an important energy source to help maintain the Earth's dynamo (e.g., Gubbins et al., 1979; Nimmo, 2007).

Since the core likely contains multiple light elements, every one of these elements does not necessarily have to strongly partition into liquid iron relative to solid iron. Rather, the exact combination of light elements in the core must be behaving in such a way that inner core crystallization enriches the outer core in at least some light elements, in abundances that can account for the ICB density contrast.

The behavior of a light element during core crystallization can be thought of in terms of partitioning

(i.e., its abundance in solid iron compared to liquid iron when the solid and liquid are in equilibrium), or equivalently, in terms of melting phase relations (Fig. 12). The most basic requirement of the core alloy's phase diagram is that the core composition must lie on the iron-rich side of the eutectic, so that core cooling and crystallization will produce a more iron-rich, denser, solid inner core (the liquidus phase) and a more iron-poor, less dense, liquid outer core. In detail, the width of the partial melting region on the Fe-rich side of the eutectic (the distance between the solidus and liquidus curves) must lead to solid and liquid compositions with the same amounts of light elements as the inner and outer core, respectively, that can thus account for the observed ICB density contrast.

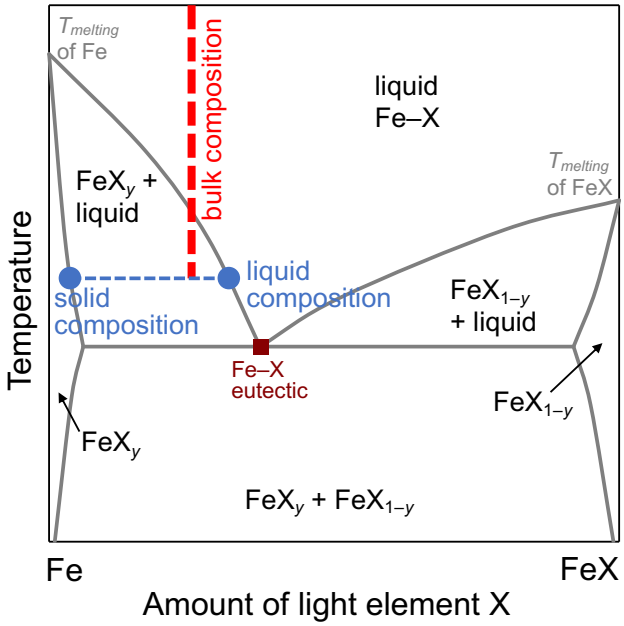

Fig. 12: Schematic cartoon of a simple binary Fe–X phase diagram at constant pressure, conceptually illustrating the constraints from seismology on the melting phase relations of the core alloy. Compositions are shown between pure Fe and an endmember Fe–light element alloy (FeX). Gray lines are phase boundaries, with stability fields labeled with black text. y indicates a small fraction; e.g., FeX_y is iron containing a small amount of light element X, while FeX_{1-y} is FeX with a small amount of excess iron. One constraint on the core alloy's phase relations is illustrated in red: the bulk composition of the core (red dashed line) must be on the Fe-rich side of the eutectic composition (dark red square) in order to crystallize a solid inner core that is more iron-rich than the liquid outer core. The other constraint is illustrated in blue: the solid and liquid (blue circles) must contain abundances of light element X that can account for the density difference between the Earth's inner and outer core. In reality the picture is more complicated, since the core's composition has more than two components and the core has a complex thermal structure and history.

Several previous studies have examined which binary and ternary core compositions would crystallize an Fe-rich liquidus phase, as opposed to a phase containing more light elements that cannot account for the inner core's density and seismic velocities. For example, it has been shown experimentally that an Fe–Si (Ozawa et al., 2016), Fe–S (Mori et al., 2017), or Fe–C (Mashino et al., 2019) binary core composition with a plausible light element abundance would not lie on the Fe-rich side of the eutectic, while an Fe–O core would (Oka et al., 2019). Core compositions in the Fe–Si–S ternary would not crystallize an Fe-rich inner core (Tateno et al., 2018), while compositions in the Fe–S–O ternary would (Yokoo et al., 2019), as would an Fe–O–H composition with less than ∼0.75 wt% H (Oka et al., 2022) or an Fe–O–C composition with less than ∼3 wt% C (Sakai et al., 2022).

The partitioning of a light element X between solid and liquid iron can be described by a partition

coefficient D_X:

$$D_X = \frac{X_X^{sol}}{X_X^{liq}} \tag{18}$$

where X_X^{sol} and X_X^{liq} are the mole fractions of element X in the solid and liquid, respectively. D_{Si} has been determined to be ∼1 at ICB conditions using ab initio methods(Alfè et al., 2002a), indicating that an Fe–Si core would have identical Si abundances in the inner and outer core and could not account for the observed ICB density contrast. Experimentally, D_{Si} was found to be even greater than one in the Fe–Si binary system (Ozawa et al., 2016) and in the Fe–Si–C (Hasegawa et al., 2021) and Fe–Si–S (Tateno et al., 2018; Sakai et al., 2023) ternary systems. Ab initio studies have reported D_O of 0.01–0.02 (Alfè et al., 2002a,b), while in experimental studies on the Fe–O binary (Ozawa et al., 2010; Oka et al., 2019) and Fe–S–O ternary (Yokoo et al., 2019) systems, the oxygen content of the metal was too low to measure analytically, indicating a D_O of ∼0.

D_S is quite small at low P–T (e.g., Li et al., 2001), but it increases strongly with increasing pressure. For example, in the Fe–S binary, Kamada et al. (2010) report a D_S of ∼0.4 by 86 GPa, Mori et al. (2017) found a value of ∼0.7 at 254 GPa, and Alfè et al. (2000) calculated D_S = ∼0.9 at the ICB. Sulfur generally seems to exhibit lower D values in ternary systems; for example, Yokoo et al. (2019) estimate a value of ∼0.8 at the ICB in the Fe–S–O system. Sakai et al. (2023) similarly found that D_S decreases with increasing Si content in the Fe–S–Si system, with studies reporting values of ∼0.2–0.3 at ∼130 GPa (Tateno et al., 2018; Sakai et al., 2023), for example. Experimental studies of carbon partitioning have found that C preferentially partitions into the liquid, with the data of Mashino et al. (2019) indicating a D_C of ∼0.2 that is fairly independent of pressure over the pressure range of that study (23–255 GPa). Hasegawa et al. (2021) report a slightly lower D_C of ∼0–0.2 in the Fe–Si–C ternary, while Sakai et al. (2022) found that D_C decreases slightly with increasing oxygen content in the Fe–C–O ternary. However, an ab initio study on carbon found much stronger partitioning into the liquid, with a D_C on the order of $\sim 10^{-5}$ (Li et al., 2019).

A few studies have also looked at the solid–liquid partitioning of other candidate light elements in iron-rich systems. For example, Oka et al. (2022) experimentally investigated the Fe–H binary and Fe–O–H ternary systems, finding a D_H of ∼0.8–0.9. Li et al. (2018) used ab initio methods to study the Fe–Mg binary system, finding a D_{Mg} of ∼0.6 at the inner core boundary.

To summarize, Si partitions equally into the solid and liquid, or perhaps more strongly into the solid (Alfè et al., 2002a; Tateno et al., 2018; Hasegawa et al., 2021; Sakai et al., 2023), while oxygen partitions almost entirely into the liquid (Alfè et al., 2002a,b; Ozawa et al., 2010; Oka et al., 2019; Yokoo et al., 2019). Sulfur has a very weak preference for the liquid phase at ICB conditions (Alfè et al., 2000; Mori et al., 2017; Yokoo et al., 2019), though its preference for the liquid may be higher in the presence of Si (Tateno et al., 2018; Sakai et al., 2023). Carbon partitions fairly strongly into the liquid (Li et al., 2019; Mashino et al., 2019; Hasegawa et al., 2021; Sakai et al., 2022), while limited results on H (Oka et al., 2022) and Mg (Li et al., 2018) suggest that they exhibit slight and moderate preferences, respectively, for partitioning into the liquid. Taken together, silicon in the core does not help explain the ICB density jump (and may have the opposite effect, though this does not preclude its presence in the core); S and H in the core would help make the outer core less dense, but not to an extent that could fully account for the seismic observations; and an O- or C-rich core may lead to an outer core that is not dense enough. Therefore, the core must contain at least some (O, C) + some (Si, S, H) to result in more light elements in the outer core (and a lower density than expected from iron's $\Delta\rho_{melting}$) compared to the inner core.

Most studies of liquidus phase relations compare their partitioning results to understanding the core's density structure. But any proposed core composition must also match the core's velocity structure,

including the jump in v_P at the inner core boundary (Fig. 7c), which provides another constraint that can be used to narrow down the solution space (e.g., Badro et al., 2014). A more detailed understanding of v_P of solids and liquids at the ICB and how they change with composition will allow this approach to be increasingly utilized in future studies.

4.4 Other mineral physics constraints on core composition

In addition to comparisons to the core's density (Section 4.1), sound velocities (Section 4.2), and liquidus phase relations (Section 4.3), mineral physics data can be used to constrain the core's composition using a number of other approaches. Here we briefly describe how mineral physics results can be compared to seismological (or other) measurements of core properties to gain insights into Earth's core composition.

The Earth's inner core is seismically anisotropic, with seismic waves traveling faster parallel to the rotation axis and slower in the equatorial plane (e.g., Morelli et al., 1986). There are also more complex patterns in the anisotropy, including hemispherical variations (e.g., Tanaka and Hamaguchi, 1997) and an innermost inner core (Ishii and Dziewoński, 2002) and other variations with depth. For reviews of this topic, see Deguen (2012) or Deuss (2014), for example. The anisotropy is thought to be due to convective flow in the inner core. This flow causes crystallographic preferred orientation of the inner core's hcp Fe alloy crystals, which are elastically anisotropic (e.g., Jeanloz and Wenk, 1988). The inner core alloy must therefore deform in such a way that it can account for the observed seismic anisotropy. A number of experimental and ab initio studies have shown that the strength and deformation behavior of pure Fe make it a plausible candidate (e.g., Stixrude and Cohen, 1995; Wenk et al., 2000; Antonangeli et al., 2006; Miyagi et al., 2008; Li and Scandolo, 2022), while other studies have investigated the effects of Ni and/or Si, which were generally found to have minor effects on deformation but to increase the strength of iron (Reagan et al., 2018; Brennan et al., 2021; Vasin et al., 2023). Reproducing the inner core's seismic anisotropy depends on a number of other material properties, including the c/a ratio of the hcp crystal (e.g., Stixrude and Cohen, 1995; Fischer and Campbell, 2015).

A related physical property is the viscosity of the inner core, which has been determined using a variety of methods to be low — significantly lower than the viscosity of the mantle (e.g., Dumberry and Bloxham, 2002; Koot and Dumberry, 2011; Davies et al., 2014). Several studies have investigated the viscosity of hcp Fe at high pressures using both ab initio and experimental approaches (e.g., Van Orman, 2004; Ritterbex and Tsuchiya, 2020; Li and Scandolo, 2022; Nishihara et al., 2023), but their reported values at inner core conditions span several orders of magnitude.

The material properties of the particular alloy that comprises the core must also be consistent with all other seismically-observable properties of the Earth's core, such as structures and heterogeneities within both the outer and inner core (e.g., Waszek et al., 2023), seismic attenuation in the inner core (e.g., Tkalčić and Phạm, 2018), and the inner core's high Poisson's ratio (e.g., Dziewonski and Anderson, 1981; Kennett et al., 1995), which is a measure of the v_P/v_S ratio. While pure iron has a Poisson's ratio that is too low to match the inner core (e.g., Fig. 9), it can be increased by the addition of C (Prescher et al., 2015), H (Wang et al., 2021a), or Ni+Si (Liu et al., 2016), for example.

Paleomagnetic measurements can place constraints on the age of the Earth's magnetic field (e.g., Tarduno et al., 2010; Brenner et al., 2022). There are several mechanisms to generate a dynamo; tidal forces could have driven the dynamo in the early Earth, while outer core convection driven by thermal and compositional gradients is the most effective mechanism in the Earth today (e.g., Landeau et al., 2022). The feasibility of this mechanism depends strongly on the properties of the core alloy, such as its liquidus phase relations (Section 4.3), its melting curve (e.g., Fischer, 2016), and its thermal conductivity. The thermal conductivity of Fe at core conditions is controversial (e.g., de Koker et al., 2012; Gomi et al.,

2013; Pozzo et al., 2014; Konôpková et al., 2016; Ohta et al., 2016), and it can be significantly affected by its light element composition (e.g., de Koker et al., 2012; Gomi et al., 2013; Pozzo et al., 2013; Zhang et al., 2021).

4.5 Limitations and future work

To improve our understanding of Earth's core composition using mineral physics constraints, we need to better characterize the physical and chemical state of liquid Fe–Ni–X alloys (where X is one or more light elements) at core conditions. Most experimental results are measured on solid Fe–Ni–X alloys, not liquids, due to technical limitations. This is true of measurements of a wide variety of properties (e.g., density, sound velocities, composition, thermal conductivity, electrical conductivity, etc.), and it is commonly not straightforward to extrapolate these properties of solid alloys to those of the same alloy in a liquid state.

Furthermore, many properties of these alloys have not yet been measured at core conditions, only at lower pressures and temperatures. While measurements on solid Fe–Ni–X alloys are directly applicable to the inner core, they typically require very large extrapolations in P and/or T to make comparisons at inner core conditions. This is more of a limitation for sound velocity measurements (Sections 4.2.2–4.2.3) than for density measurements (Sections 4.1.3–4.1.5). It is relatively routine to measure densities at high pressures with in situ laser heating (e.g., Prakapenka et al., 2008), while there are more obstacles to measuring sound velocities at high temperatures. Several recent studies have measured velocities at high P–T (e.g., Sakairi et al., 2018; Takahashi et al., 2019b; Tanaka et al., 2020), though at pressures and temperatures significantly lower than those in the core, paving the way for future studies to push the conditions of those measurements. While large extrapolations of any kind should ideally be avoided, they are particularly problematic for compositions that undergo a phase transition at high P–T, because measurements on those alloys at lower P–T may be on a phase that is not stable at core conditions.

Solubility and partitioning studies would benefit from more in situ measurement capabilities, which may allow for avoiding the chemical and physical effects of quenching and decompression. In particular, hydrogen in Fe-rich alloys is known to diffuse out of the sample upon decompression, so that the H content of an alloy can only be estimated using in situ XRD to detect its effect of the lattice parameter of Fe (e.g., Thompson et al., 2018; Oka et al., 2022; Tagawa et al., 2022), a method that bears considerable uncertainties.

High pressure–temperature mineral physics experiments bear large uncertainties in P and especially T measurements. There is better agreement over pressure scales at conditions of the upper and lower mantle (Shen et al., 2020). However, there are larger discrepancies and more debate over pressure scales at core conditions and beyond (e.g., Ikuta et al., 2023), which has been the subject of a number of recent meetings and workshops; AIRAPT (International Association for the Advancement of High Pressure Science and Technology) is one organization that is advancing these efforts. Accurate temperature measurements in the LH-DAC require a careful optical design to minimize aberrations, along with benchmarking and regular calibrations. Even with these precautions, T uncertainties are typically ∼5–10%, due at least in part to axial and radial temperature gradients and instabilities in laser heating, all of which are difficult to avoid with current techniques.

5 The formation of Earth's core

The Earth's metallic core is generally thought to have segregated from its silicate mantle throughout the planet's formation roughly 4.5 billion years ago. The Earth grew through the accretion of many smaller objects, and the energy from these impacts would have caused large-scale melting on the planet's

surface, generating a local or global magma ocean(s). The molten metal in these impactors reacted with this molten silicate at high pressures and temperatures in a series of metal–silicate partitioning reactions before sinking down to join the growing core (e.g., Righter, 2003; Rubie and Jacobson, 2016) (Fig. 13). It is critical to understand this core formation process due to its role in establishing the compositions of the core and mantle, as well as setting the initial conditions for many deep Earth processes. In particular, it offers a different approach to understanding core composition that is independent of light element constraints from cosmochemistry (Section 3) and the core's physical properties (Section 4).

5.1 Physics of accretion and core formation

5.1.1 Earth's mass evolution

Because Earth's core formation occurred simultaneously with the planet's accretion, understanding core formation requires an understanding of the mass, timing, and source regions of material accreted by the Earth (Fig. 13b). Insights into the accretion process come primarily from N-body simulations, which model the orbital evolution of the inner Solar System (plus Jupiter and Saturn) during terrestrial planetary formation (e.g., Walsh et al., 2011; Fischer and Ciesla, 2014; Johansen et al., 2021; Woo et al., 2022). The outputs from such simulations have been used in several studies on Earth's core formation (e.g., Rubie et al., 2015a; Gu et al., 2023, 2024), providing constraints on the accretion process and a sense of the large stochastic variations that are possible (Fischer et al., 2017). N-body simulations can also be combined with cosmochemical data (Section 3) to provide greater insight into the compositions of the Earth's building blocks and how they may have evolved with time during the Earth's growth (e.g., Fischer et al., 2018; Carter and Stewart, 2022).

Some studies instead use a multi-stage model where mass is added to the Earth over time in a large number of steps (e.g., Wade and Wood, 2005; Badro et al., 2015), as in N-body simulations but following a prescribed growth history. This results in evolving core formation conditions as the planet grows, in contrast to earlier studies that modeled core formation as occurring at a single P–T (e.g., Li and Agee, 1996; Corgne et al., 2009; Righter, 2011), which may be thought of as some effective average of the varying core formation conditions that the Earth experienced.

5.1.2 Extent of melting

Knowledge of the physical mechanisms of core formation can come from a variety of numerical and experimental approaches. For example, the depth (P–T) of metal–silicate equilibration is often thought to depend on the volume of impact-generated melt as well as melt geometry (e.g., a shallower global magma ocean versus a deeper local magma pond). The fraction of the mantle that equilibrates with the impactor's metal (k_{mantle}) should also depend in part on the extent of mantle melting (Fig. 13c), since equilibration with solid silicates is prohibitively slow.

Estimates of the amount of melting caused by an impact can come from melt-scaling laws, based on analytical approaches and/or smoothed particle hydrodynamic (SPH) simulations (Abramov et al., 2012; Nakajima et al., 2021). These laws indicate that larger volumes of melt are produced by more head-on impact angles, higher initial mantle temperatures, more massive impactors, and higher velocities, with more localized melting produced by grazing impact angles. These melt-scaling laws are beginning to be coupled with outputs from N-body simulations to better understand the conditions of Earth's core formation (de Vries et al., 2016; Gu et al., 2023).

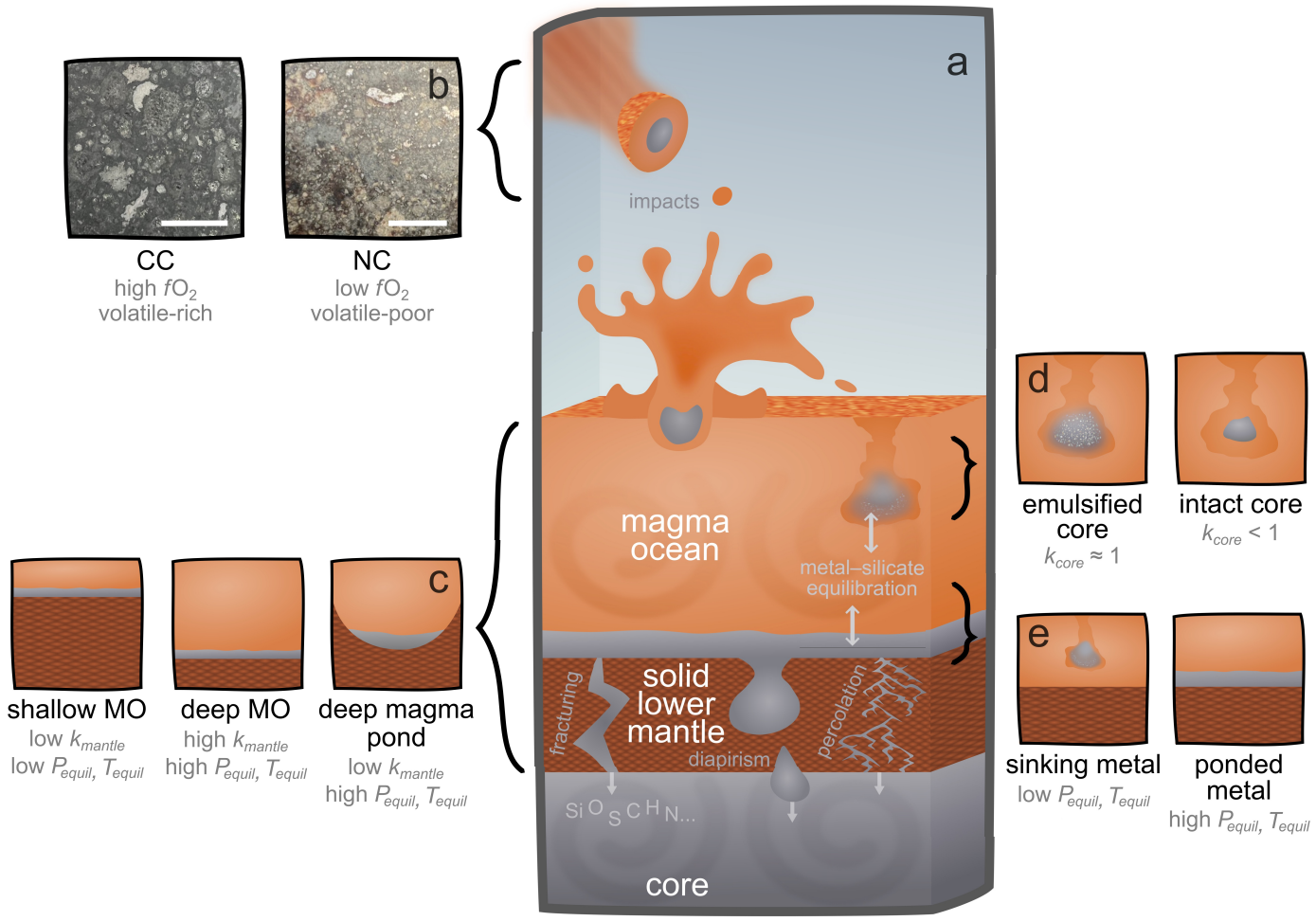

Fig. 13: An overview of Earth's core formation (a) with several examples of how physical processes are manifested in core formation models (side panels b–e). a: The Earth grew through a series of energetic impacts, contributing to the generation of a magma ocean (MO) on the surface. The impactors' metal sank through this magma ocean and pooled atop a rheologically-solid lower mantle at its base. Eventually this metal descended through the lower mantle via fracturing, diapirism, and/or percolation, forming the core and establishing its initial composition (Section 5.1). b: Examples of different impactor compositions. CC-like bodies are more oxidized and volatile-rich (left; photo of Allende, a CV carbonaceous chondrite), while NC-like bodies are more reduced and volatile-poor (right; photo of NWA869, an ordinary chondrite) (Section 3.1). Scale bars are ~0.5 cm. c: Effects of different extents and geometries of melting. A shallow magma ocean (left) would have exhibited a lower degree of silicate equilibration (k_{mantle}) and a lower pressure and temperature of metal–silicate equilibration (P_{equil} and T_{equil}) than a deeper magma ocean (middle). A deep but localized magma pond (right) may have had a similarly low k_{mantle} but with higher P_{equil} and T_{equil}. d: An undifferentiated impactor or one whose core emulsified as it sank through the magma ocean (left) would have exhibited near-complete metal equilibration (high k_{core}), while a large impactor core that remained mostly intact (right) would have had a lower k_{core}. e: If the metal equilibrated with the magma ocean while it was sinking (left), it would have recorded a relatively lower P_{equil} and T_{equil}, but if this signature was overprinted while the metal was ponded at the base of the magma ocean (right), it may have a signature of higher P_{equil} and T_{equil}.

5.1.3 Fluid dynamics of sinking impactor cores

The fraction of impactor metal that equilibrated (k_{core}) and the depth of equilibration were also affected by how the metal descended through the magma ocean, and how the timescales of these processes compared to diffusion timescales for chemical equilibration. An undifferentiated impactor would likely have exhibited $k_{core} \approx 1$ due to the small size of metal particles, while a differentiated impactor would have $k_{core} < 1$. The exact value should be dependant on the degree of impactor core fragmentation and turbulent mixing, which may be functions of impact velocity, impact angle, impactor and target masses, and other variables.

A giant impact (such as the Moon-forming impact) may have resulted in an impactor core that did not have time to fully emulsify as it sank; in this case, the mostly-intact core would have reached the base of the magma ocean within only a few hours (Canup, 2004; Deguen et al., 2014), resulting in a low k_{core} (e.g., Dahl and Stevenson, 2010) (Fig. 13d). Fluid dynamics experiments on analogue liquids show efficient turbulent entrainment once the impactor core sinks through the magma ocean a distance of 3–4 times its diameter, with shorter lengthscales and timescales of sinking required for equilibration for smaller impactors and faster sinking velocities (Fig. 14a) (Deguen et al., 2014).

Importantly, higher impact velocities result in increased metal–silicate mixing, with laboratory experiments indicating that at realistic velocities, $k_{core} \approx 1$ during Earth's core formation for impactor diameters of <100 km (Landeau et al., 2021). Kendall and Melosh (2016) similarly argued based on hydrocode simulations that the cores of differentiated impactors would have been significantly stretched and dispersed as they plunged through the magma ocean, especially in oblique impacts, possibly resulting in very high k_{core} even for large impactors.

If a sinking impactor core broke up into droplets, this may have been a rapid process producing droplet diameters of ∼1–20 cm, likely small enough to equilibrate with the magma ocean while descending (e.g., Rubie et al., 2003; Samuel, 2012; Deguen et al., 2014) with a terminal velocity of ∼0.5–2 m/s (Rubie et al., 2003; Ziethe, 2009). These metal droplets would have equilibrated continuously as they sank, so that their compositions were overprinted by equilibration within a small region just above/at the base of the magma ocean (Rubie et al., 2003). However, Rubie et al. (2003) argued that if the magma ocean did not convect vigorously, the equilibration depth signature recorded by the BSE's composition could represent an effective average pressure of polybaric equilibration between the magma ocean and falling metal droplets, which some convection models indicate may be plausible (Höink et al., 2006).

These types of fluid dynamical studies could also be used to constrain k_{mantle}. For example, Landeau et al. (2021) showed that more silicate (relative to the size of the impactor) mixes with the metal as it sinks through the magma ocean for smaller impactors and faster impact velocities (Fig. 14b).

5.1.4 Descent through a solid lower mantle

Whether or not the Earth today preserves a signature of metal–silicate equilibration while the metal was falling or entrained in the magma ocean depends on whether the metal remained ponded at its base, atop a rheologically solid ($\lesssim$40% melt; Solomatov, 2000) lower mantle, long enough to equilibrate with the overlying magma ocean before that magma ocean solidified (Fig. 13e). The mechanism(s) by which the molten metal moved through the solid silicate are somewhat controversial, with the three main hypotheses being fracturing/dyking, diapirism, and/or percolation (e.g., Karato and Murthy, 1997; Rubie et al., 2015b) (Fig. 13a).

Fracturing, or dyking, is the descent of the metal through brittle cracks in the silicate. Diapirism, or the sinking of the metal in one or a few large blobs through the solid silicate, may be a more plausible mechanism than fracturing, depending on silicate rheology. Percolation involves migration of liquid

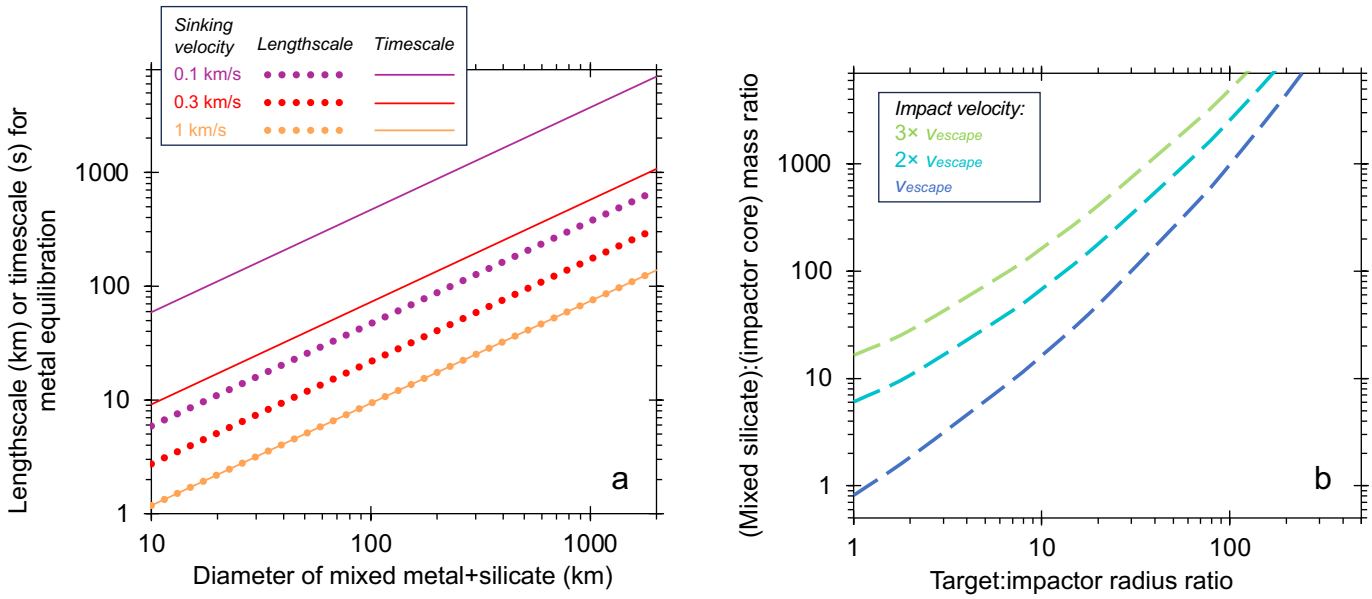

Fig. 14: Constraints on core formation from fluid dynamics experiments. a: Lengthscale (dotted lines) or timescale (solid lines) that an entrained mixture of metal and silicate has to sink through a magma ocean for the metal to equilibrate, as a function of the diameter of the metal+silicate mixture and the sinking velocity. After Deguen et al. (2014). b: The total mass of silicate that mixes with the sinking metal following an impact into a magma ocean (expressed as the ratio of this mixed silicate mass to the impactor's core mass). This quantity of mixed silicate is a function of the target:impactor radius ratio and the impact velocity, which is shown here as a multiple of the escape velocity v_{escape}. After Landeau et al. (2021).

metal along the grain boundaries of solid silicate and is generally thought to require a dihedral angle of $\lesssim 60°$ or a high melt fraction to produce an interconnected melt network. Many experimental studies on the dihedral angles of lower mantle minerals have reported values of $>60°$ (e.g., Shannon and Agee, 1998; Terasaki et al., 2007), though they decrease at higher P–T (Takafuji et al., 2004; Shi et al., 2013) and with increasing S and O in the metal (Terasaki et al., 2005, 2007), and it may be possible to form interconnected melts even with high dihedral angles and low melt fractions if the stress is sufficiently high (Walte et al., 2011; Wang and Fei, 2023).

Regardless of mechanism, the metal was likely ponded on the solid silicate interface for timescales of $\sim 10^3$–10^4 kyr before descending (Golabek et al., 2008, 2009; Lin et al., 2009; cf. Fleck et al., 2018). These timescales are longer than the timescale required for metal–silicate equilibration, which Rubie et al. (2003) estimates as $\sim 10^1$–10^2 kyr, for example, suggesting that equilibration at the base of the magma ocean may have overprinted any signature of equilibration from when the metal was sinking through the magma ocean.

However, that would also require the magma ocean crystallization timescale to be longer than the equilibration timescale. The timescale for a magma ocean to crystallize is highly uncertain, with estimates ranging from $\sim 10^{-2}$–10^0 kyr in the absence of an insulating atmosphere (Solomatov, 2000; Rubie et al., 2003) to $\sim 10^2$–10^3 kyr with an H_2O-rich atmosphere (Elkins-Tanton, 2008; Hamano et al., 2013; Nikolaou et al., 2019); the presence of a solid conductive lid would similar delay magma ocean solidification, though the formation of a long-lived conductive lid on Earth's magma ocean may have been unlikely (Elkins-Tanton, 2012). Therefore, the presence of an insulating atmosphere and/or conductive lid likely determined the extent to which the magma ocean equilibrated with the metal, and whether a large

impactor core had time to equilibrate at the base of the magma ocean, while any metal droplets would have likely equilibrated rapidly enough to only record the depth signature from near the base of the magma ocean regardless (Rubie et al., 2003).

5.2 Metal–silicate partitioning

5.2.1 Experimental techniques for metal–silicate partitioning

Another key prerequisite for assessing the effects of core formation on planetary composition is an understanding of the metal–silicate partitioning behaviors of major, minor, and trace elements during core–mantle reactions, and how these behaviors change with evolving pressure, temperature, composition (X), and oxygen fugacity (fO_2) conditions in a growing planet. These behaviors are typically studied via experiments in which mixtures of silicate (mantle analogue) and Fe-rich metal (core analogue), doped with element(s) of interest, are melted under high pressure, allowed to chemically react, then quenched and recovered to atmospheric conditions for chemical analysis.

There is a substantial amount of metal–silicate partitioning data in the literature derived from experiments in a large volume press (LVP; e.g., multi-anvil press or piston–cylinder apparatus). These methods allow for more control over experimental conditions and application of a wider variety of analytical techniques, providing greater insights into the effects of fO_2 and composition, for example, but they are limited in the P–T conditions they can reach (generally a maximum of ∼25 GPa).

To measure metal–silicate partitioning at the highest pressures and temperatures of Earth's core formation (up to ∼80–110 GPa; e.g., Rubie et al., 2015a; Fischer et al., 2017; Gu et al., 2023) requires experiments in a laser-heated diamond anvil cell. LH-DAC experiments can achieve these higher P–T conditions at the expense of larger uncertainties, little to no control over redox conditions, difficulty performing experiments at lower P–T conditions (such as those achievable in an LVP), and limited choices in sample recovery and analysis techniques, due primarily to the much smaller sample size required to achieve these pressures. An example of an LH-DAC run product is shown in the inset of Fig. 15.

Both LVP and LH-DAC data tend to exhibit strong covariances in pressure and temperature, with higher pressure data typically being obtained at higher temperatures too. This is primarily due to experimental limitations and/or temperature instability when heating far above the silicate liquidus. This correlation between P and T within a dataset can sometimes make it particularly difficult to disentangle the effects of these variables on partitioning. Elements whose metal–silicate partitioning behaviors are best understood are those with a large body of experimental data obtained using complementary LVP and LH-DAC techniques.

5.2.2 Elements with well-studied partitioning behaviors

Elements whose partitioning behaviors have been the best studied so far can be broadly categorized as refractory trace elements, candidate core light elements, and other groups of elements. The most useful refractory trace elements for studying core formation are those whose BSE abundances are well-constrained; that are relatively unaffected by volatile delivery/loss processes, so that their core abundances are also well-constrained by cosmochemical arguments (Section 3); and that exhibit some significant changes in metal–silicate partitioning behaviors with changing P–T–X–fO_2 (e.g., most of the moderately siderophile elements). These combined properties allow these elements' observed BSE abundances to act as signatures of Earth's core formation conditions, and some insight into these conditions can be obtained by considering combinations of multiple refractory trace elements. Some of the most well-studied elements in this category include, for example, Ni, Co, V, W, and Mo (e.g., Thibault and

Walter, 1995; Righter et al., 2010; Bouhifd and Jephcoat, 2011; Siebert et al., 2013; Fischer et al., 2015; Huang et al., 2021).

With this improved understanding of the conditions of core formation, partitioning data on candidate core light elements (Si, O, S, C, H) can be used to forward-model their most likely abundances in the core (Section 5.4). These elements are generally also well-studied (e.g., Tsuno et al., 2013; Fischer et al., 2015, 2020; Suer et al., 2017; Clesi et al., 2018; Grewal et al., 2019b; Tagawa et al., 2021; Blanchard et al., 2022), with less work on H at LH-DAC conditions due to experimental and analytical limitations.

The metal–silicate partitioning behaviors of many other groups of elements have also been studied to learn about various processes, such as moderately and highly volatile elements, which may provide insight into volatile delivery (Fig. 13b) and loss (e.g., Mahan et al., 2018b; Siebert et al., 2018; Vogel et al., 2018; Bouhifd et al., 2020; Jackson et al., 2021); elements that are part of isotopic decay systems and may thus act as heat sources or be used to constrain the timing of core formation and other early Earth processes (e.g., Jackson et al., 2018; Jennings et al., 2021; Chidester et al., 2022); and highly siderophile elements, whose BSE abundances are thought to be very sensitive to late accretion (e.g., Mann et al., 2012; Suer et al., 2021).

5.2.3 Quantitative description of metal–silicate partitioning

The metal–silicate partitioning of an element M with non-zero valence n in the silicate melt results in the oxidation of iron via an exchange reaction:

$$\mathrm{MO}_{n/2} + \frac{n}{2}\mathrm{Fe} \leftrightarrow \mathrm{M} + \frac{n}{2}\mathrm{FeO} \tag{19}$$

The behavior of element M may be described by a metal–silicate partition coefficient D_M:

$$D_\mathrm{M} = \frac{X_\mathrm{M}^{met}}{X_{\mathrm{MO}_{n/2}}^{sil}} \tag{20}$$

where X_M^{met} is the mole fraction of M in the metallic melt and $X_{\mathrm{MO}_{n/2}}^{sil}$ is the mole fraction of its oxide in the silicate melt. Sometimes D is expressed in terms of wt% instead of mole fractions, and sometimes the denominator is written as the abundance of the element M instead of its oxide, especially if its valence n is zero or unknown or if it can have multiple values (e.g., $D_\mathrm{M} = C_\mathrm{M}^{met}/C_\mathrm{M}^{sil}$, where C_M^{met} and C_M^{sil} are the concentrations in wt% of M in the metal and silicate, respectively).

Alternatively, the partitioning behavior of element M may be described by an exchange coefficient K_D^M:

$$K_D^\mathrm{M} = \frac{D_\mathrm{M}}{{D_\mathrm{Fe}}^{n/2}} \tag{21}$$

which has the advantage of normalizing out the effects of oxygen fugacity if the valence n is known. This is because the oxygen fugacity in log units relative to the iron–wüstite buffer (ΔIW) is related to the partition coefficient of iron (D_Fe):

$$\Delta\mathrm{IW} \approx 2\log\frac{X_\mathrm{FeO}^{sil}}{X_\mathrm{Fe}^{met}} = -2\log D_\mathrm{Fe} \tag{22}$$

under the approximation of ideality.

Either D_M (equation 20) or K_D^M (equation 21) may be parameterized as a function of many experimental variables, depending on the element's sensitivity to each variable, such as:

$$D_\mathrm{M} \text{ or } K_D^\mathrm{M} = a + \frac{b}{T} + \frac{c \cdot P}{T} + ... \tag{23}$$

with possible additional terms for the light element composition of the metallic melt (e.g., $d \cdot \log(1 - X_{\mathrm{S}}^{met})$ for sulfur), the structure/composition of the silicate melt (e.g., $d{\cdot}$NBO/T, where NBO/T is the number of non-bridging oxygen atoms per tetrahedrally-coordinated cation, a measure of the degree of polymerization of the silicate melt), and/or oxygen fugacity (e.g., $d \cdot \Delta$IW, only used with D_{M}).

For example, the metal–silicate partitioning behavior of carbon has been described as:

$$\begin{aligned} \log_{10} D_{\mathrm{C}} &= \log_{10}\left(\frac{C_{\mathrm{C}}^{met}}{C_{\mathrm{C}}^{sil}}\right) \\ &= 1.5(7) + \frac{3000(1100)}{T} - \frac{240(60)\cdot P}{T} + 9.6(14)\cdot\log_{10}(1 - X_{\mathrm{S}}^{met}) \\ &\quad - 20(9)\cdot\log_{10}(1 - X_{\mathrm{O}}^{met}) - 0.12(4)\cdot\mathrm{NBO/T} - 0.24(9)\cdot\Delta\mathrm{IW} \end{aligned} \tag{24}$$

with T in kelvin, P in GPa, and fO_2 in $\log_{10}$ units relative to IW (Fischer et al., 2020; cf. Blanchard et al., 2022). Equation 24 indicates that carbon becomes less siderophile (lower D_{C}) with increasing P, X_{S}^{met}, NBO/T, or fO_2, or with decreasing X_{O}^{met}. Below ~15 GPa, carbon becomes less siderophile with increasing T, but this trend reverses at higher pressures. Equation 24 is shown compared to experimental data on carbon metal–silicate partitioning in Fig. 15.

5.3 Conditions and timing of core formation from geochemical modeling

Core formation is an extremely complex process that inherently must be greatly simplified in numerical models. These models are typically based on a small number of parameters that approximate the physical conditions of core formation, describing the depth (P and T) and redox conditions of metal–silicate equilibration, extent of metal and silicate equilibration, and sometimes other factors such as the bulk compositions of Earth's building blocks (especially when considering volatile elements) and the timing of accretion and differentiation (especially when considering isotopic decay) (Fig. 13).

5.3.1 Observational constraints on core formation

These model parameters describing the conditions of core formation are constrained by requiring the models to reproduce various aspects of modern-day geochemistry, including the observed BSE composition in terms of major, minor, and trace elements (Table 4) and bulk planetary fO_2 (defined as $\Delta\mathrm{IW} \approx 2\log\frac{X_{\mathrm{FeO}}^{mantle}}{X_{\mathrm{Fe}}^{core}}$, similar to equation 22 for an individual reaction). Geophysical properties, such as Earth's core mass fraction (Table 1) (e.g., Rubie et al., 2015a; Fischer et al., 2017; Chidester et al., 2022) and core density and sound velocities (Section 4) (e.g., Badro et al., 2015), are sometimes also used as constraints.

Additional insight can come from the BSE's isotopic composition, such as in the Hf–W system. Hf is lithophile and W is moderately siderophile, so they are efficiently separated by core formation, and ^{182}Hf decays into ^{182}W with a half-life of 8.9 Myr, making this system an excellent probe of the core formation process. The Hf/W ratio (of a sample, reservoir, or body, for example) can be described in terms of mole fractions of stable isotopes compared to those in chondrites:

$$f^{\mathrm{Hf/W}} = \frac{(X^{180\mathrm{Hf}}/X^{184\mathrm{W}})_{sample}}{(X^{180\mathrm{Hf}}/X^{184\mathrm{W}})_{chondrites}} - 1 \tag{25}$$

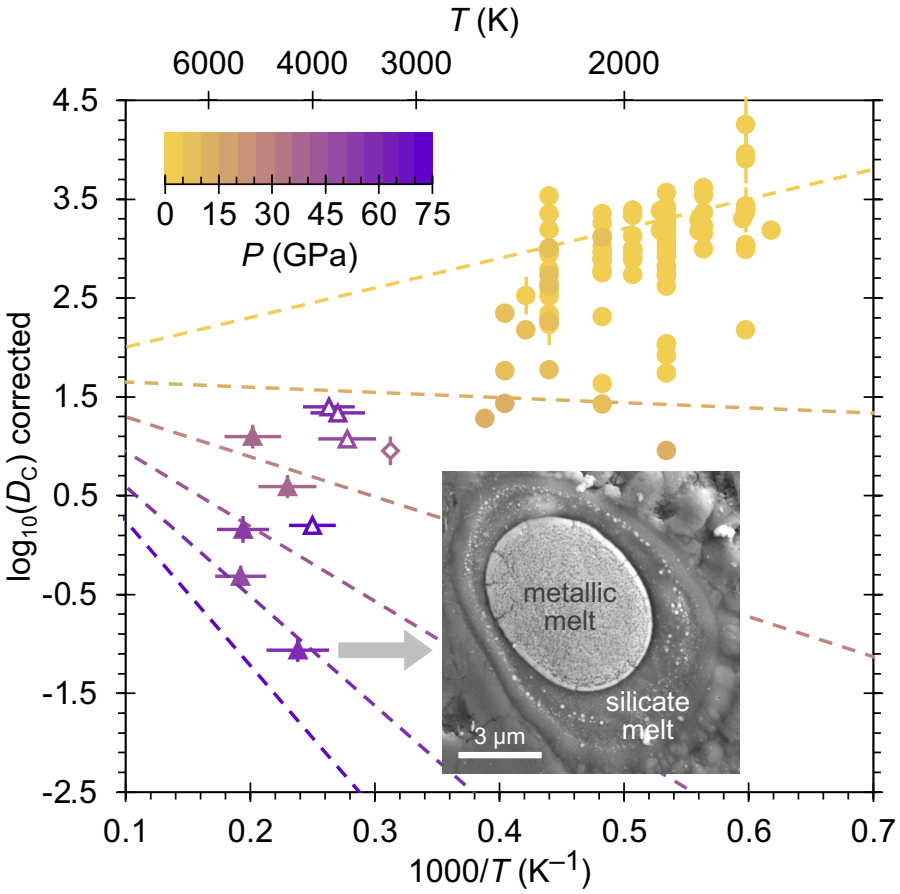

Fig. 15: Metal–silicate partitioning behavior of carbon as a function of pressure and temperature. Filled symbols indicate literature data that were used to parameterize the partitioning of C (equation 24), with filled circles showing LVP data (Dasgupta et al., 2013; Chi et al., 2014; Stanley et al., 2014; Armstrong et al., 2015; Li et al., 2015, 2016; Grewal et al., 2019b; Malavergne et al., 2019) and filled triangles showing LH-DAC data (Fischer et al., 2020). Open symbols are data not used in the fit; the open diamond is an ab initio calculation (Zhang and Yin, 2012), and the open triangles are LH-DAC data (Blanchard et al., 2022). To better show the effects of pressure and temperature on C partitioning, the data plotted here have been corrected using the fitted coefficients in equation 24 to eliminate variations caused by other variables; values of D_C in this figure have all been corrected to arbitrary values of $X_O = X_S = 0$, NBO/T = 2.6, and fO_2 = IW–2.2 to make it easier to visually compare the data. Dashed lines show the fit (equation 24) for these values of X_O, X_S, NBO/T, and fO_2, calculated at pressures of 0, 15, 30, 45, 60, and 75 GPa. Inset: secondary electron image of an LH-DAC experiment recovered from 59(10) GPa and 4200(400) K (Fischer et al., 2020).

equal to approximately 17(4) for the BSE (e.g., Kleine and Walker, 2017). A sample's W isotopic composition can be expressed as a ^{182}W anomaly, defined using epsilon notation:

$$\epsilon_{182\mathrm{W}} = \left[\frac{(X^{182\mathrm{W}}/X^{184\mathrm{W}})_{sample}}{(X^{182\mathrm{W}}/X^{184\mathrm{W}})_{BSE}} - 1 \right] \times 10^4 \tag{26}$$

which is $\equiv 0$ for the BSE (e.g., Yin et al., 2002). While the Hf–W isotopic system is often thought of as a chronometer, it is sensitive to both the timing and conditions of core formation (e.g., Nimmo and Agnor, 2006). The application of these equations to understanding the timing of Earth's core formation is discussed in Section 5.3.8.

5.3.2 Equilibration pressure

In multi-stage core formation models, the metal–silicate equilibration pressure following an impact (P_{equil}) is commonly approximated as being a fixed fraction (f_P) of Earth's core–mantle boundary pressure (or depth) at that time (P_{CMB}), such that the equilibration pressure increases monotonically as the Earth grows:

$$P_{equil} = f_P \cdot P_{CMB} \tag{27}$$

(Rubie et al., 2011). This approach is able to reproduce Earth's mantle composition for $f_P \approx 0.4-0.75$, or equivalently, a maximum P_{equil} of $\sim 45-100$ GPa at the end of Earth's growth (e.g., Wade and Wood, 2005; Rubie et al., 2011, 2015a; Badro et al., 2015; Fischer et al., 2017; Fischer and Nimmo, 2018; Olson et al., 2022) (Fig. 16).

When equilibration depth is instead determined from a melt-scaling law coupled with N-body simulations (Section 5.1.2), it does tend to increase linearly throughout most of Earth's growth (with large stochastic variations due to accretion history), but that equilibration depth often remains fairly constant at its maximum value for the last ~30–40% of the core formation process (Gu et al., 2023) (Fig. 16). However, the exact depth of mantle melting depends on the assumed initial masses of Earth's impactors in the N-body simulations, which are poorly known. Future modeling studies of core formation may be able to utilize parameterizations of results like these to capture a more realistic P–T evolution without incorporating full melt-scaling calculations (e.g., Gu et al., 2024).

5.3.3 Equilibration temperature

The temperature of metal–silicate equilibration (T_{equil}) should be at or near the mantle liquidus temperature at each pressure, though there is some disagreement over the liquidus at lower mantle pressures (e.g., Fiquet et al., 2010; Andrault et al., 2011). Equilibration of the magma ocean with ponded metal at its base, or with rapidly equilibrating metal droplets that record a depth signature near its base (Section 5.1), should have occurred very close to the silicate liquidus. However, equilibration with falling metal droplets at shallower depths could have been farther from the liquidus (Rubie et al., 2011). Several studies have placed constraints on T_{equil}, often parameterizing it as a fixed temperature difference ($\Delta T_{equil-liq}$) from the liquidus temperature (T_{liq}) at each P_{equil} step:

$$T_{equil} = T_{liq}(P_{equil}) + \Delta T_{equil-liq} \tag{28}$$

(Rubie et al., 2011). Estimates of allowed values of $\Delta T_{equil-liq}$ range from approximately -400 to $+750$ K relative to the liquidus of Andrault et al. (2011) (e.g., Badro et al., 2015; Rubie et al., 2015a; Fischer et al., 2017; Mahan et al., 2018b; Olson et al., 2022) (Fig. 16).

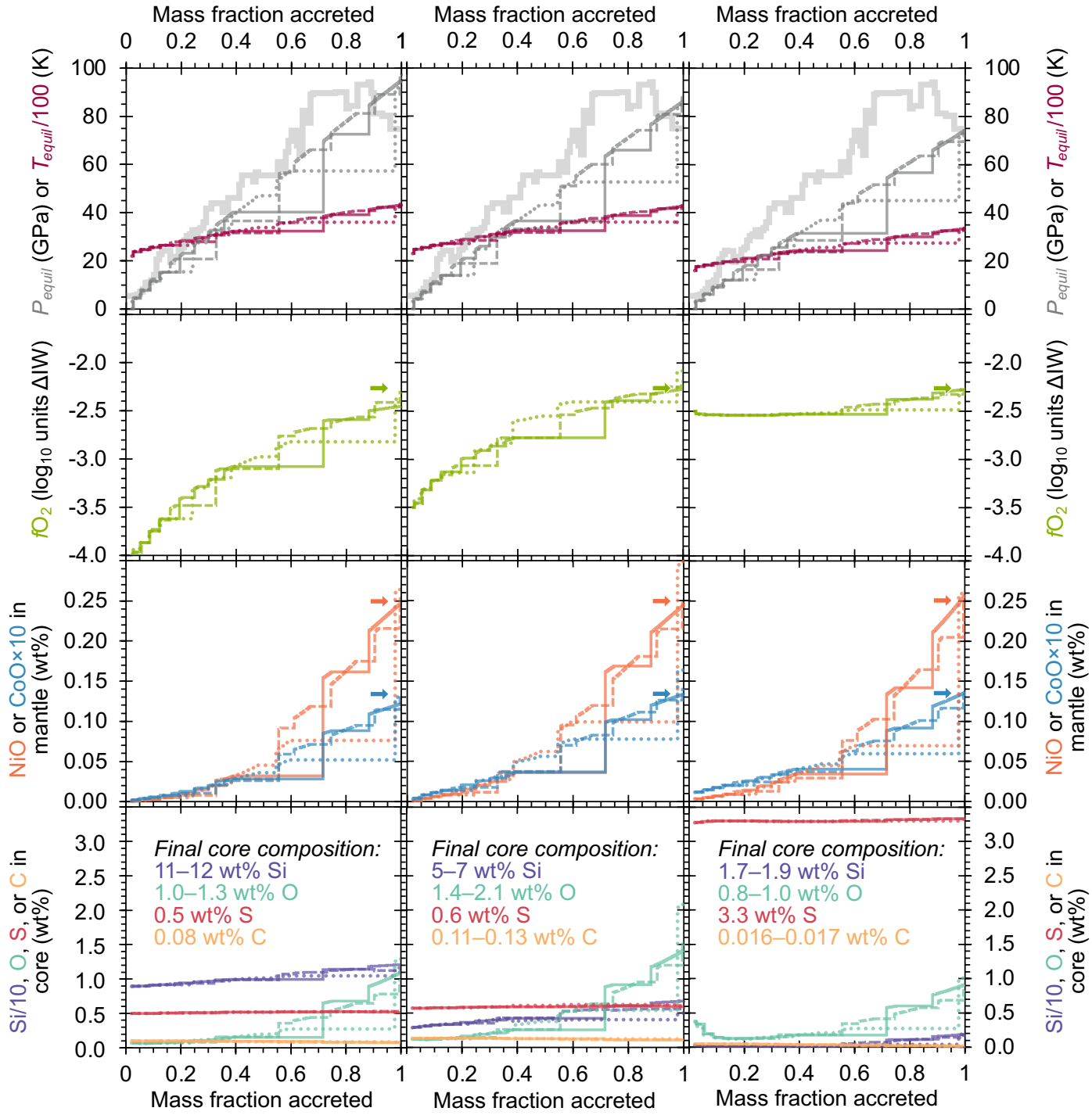

High Si example

f_P = 0.75
$\Delta T_{equil–liq}$ = +200 K
Initial fO_2 = IW–4 to IW–2 at 3 AU
k_{core} = 0.4
m_{sil} = 2× impactor's silicate
Bulk C = 0.15 wt%
Bulk S = 0.3 wt%

High O example

f_P = 0.65
$\Delta T_{equil–liq}$ = +300 K
Initial fO_2 = IW–3.5 to IW–2 at 2 AU
k_{core} = 0.5
m_{sil} = 1× impactor's silicate
Bulk C = 0.19 wt%
Bulk S = 0.3 wt%

High S example

f_P = 0.55
$\Delta T_{equil–liq}$ = –400 K
Initial fO_2 = IW–2.5
k_{core} = 1
m_{sil} = 2.5× impactor's silicate
Bulk C = 0.06 wt%
Bulk S = 1.6 wt%

Fig. 16 *(previous page)*: Three examples of evolving core formation conditions and chemistry during Earth's accretion, maximizing core silicon (left column), oxygen (middle column), or sulfur (right column) contents. Solid, dashed, and dotted lines are three different Earth analogue planets from the N-body simulations of Fischer and Ciesla (2014), each with a final mass of ∼1 Earth mass and final semimajor axis of ∼1 AU but with different provenance and temporal evolution. Arrows indicate actual Earth values (e.g., Table 4). Top row: P–T conditions of metal–silicate equilibration, compared to average equilibration pressures of 12 Earth analogues determined using a melt-scaling law (thicker transparent grey curve, from Gu et al., 2023). Second row: bulk Earth oxygen fugacity relative to the iron–wüstite buffer (calculated as $2 \log \frac{X_{FeO}^{mantle}}{X_{Fe}^{core}}$). Third row: trace element oxides in the mantle. Fourth row: light element composition of the core, with the ranges of final core compositions produced in the three Earth analogues. Bottom: model parameters used (see text for details). $\Delta T_{equil-liq}$ is the difference between the equilibration temperature (T_{equil}) and the silicate liquidus of Andrault et al. (2011) (equation 28). C and S contents refer to their abundances in the bulk Earth. Calculations were performed using a modified version of the model of Fischer et al. (2017), with partitioning parameterizations (e.g., equation 24) from Fischer et al. (2015, 2020) and Suer et al. (2017). See text for more details.

5.3.4 Redox conditions

Because metal–silicate partitioning frequently involves a change in valence state, the partitioning behaviors of many elements are very sensitive to redox conditions. Some studies have modeled Earth's core formation as occurring at a fixed fO_2, typically the modern bulk Earth value of ∼IW–2.3 (e.g., Siebert et al., 2012; Mahan et al., 2018b; Suer et al., 2021). However, the redox conditions of core formation most likely changed over the course of the Earth's growth, increasing due to the accretion of more oxidized materials from the outer Solar System at later times (e.g., Wetherill, 1990; O'Brien et al., 2014) and due to metal–silicate partitioning itself (equation 19), particularly the reduction of silicon from SiO_2 to Si metal and the corresponding oxidation of Fe metal to FeO at high P–T, increasing fO_2 relative to the IW buffer (e.g., Javoy, 1995; Rubie et al., 2011). Furthermore, Wade and Wood (2005) and other studies have argued that the mantle's composition can only be reproduced in multi-stage models if fO_2 increased over time.

It is now common practice to impose a changing fO_2 history during Earth's growth, usually from reduced to oxidized but sometimes from oxidized to reduced. For example, previous studies report successful models with initial fO_2 ranging from ∼IW–4 (Wade and Wood, 2005; Siebert et al., 2012) to ∼IW–1 (Siebert et al., 2013; Badro et al., 2015), evolving up or down to its present-day value, indicating that many fO_2 paths may match the Earth's mantle composition (Wood et al., 2006). This approach can be problematic, however, because it does not necessarily ensure consistency with metal–silicate partitioning effects or guarantee conservation of oxygen atoms.

Alternatively, the pioneering work of Rubie et al. (2011) developed a method for "self-consistent" oxygen fugacity evolution, in which the redox conditions of core formation are recalculated with each impact based on metal–silicate partitioning and mass balance considerations instead of arbitrarily imposed. This self-consistent fO_2 evolution method (Rubie et al., 2011) has been adopted in several subsequent studies (e.g., Rubie et al., 2015a; Fischer et al., 2015, 2017; Chidester et al., 2022; Shi et al., 2022; Gu et al., 2023, 2024). This approach is indeed more self-consistent and avoids violations of the mass balance of oxygen, and only requires one (or variable) initial oxidation state(s) of accreted material to be specified, but is more computationally expensive and difficult to implement relative to an imposed redox evolution. Self-consistent redox calculations typically result in an evolution from reduced to oxidized, with Fischer et al. (2015) showing that it is impossible to achieve a substantial decrease in fO_2 over time using this

approach. In general, more oxidation occurs when Earth's building blocks are initially more reduced and/or when metal–silicate partitioning occurs at more extreme P–T (Fig. 16). This method can match the Earth's modern bulk fO_2 if most of Earth's building blocks were initially reduced (approximately IW–4 to IW–2.5), with outer Solar System materials often assumed to be more oxidized.

5.3.5 Extent of metal equilibration

The fraction of incoming metal that equilibrates with each impact (k_{core}) is typically modeled as being constant throughout the Earth's accretion. This is probably unrealistic, with variations likely due to differences in impactor size and impact geometry (Section 5.1.3). However, this approximation helps to reduce the number of parameters in core formation models, and may provide an effective average of the k_{core} values that Earth experienced.

A few studies (e.g., Rubie et al., 2011; Suer et al., 2017; Mahan et al., 2018b; Gu et al., 2023, 2024) have implemented more realistic treatments of k_{core}, using different values for embryo versus planetesimal impacts or using parameterizations of k_{core} derived from fluid dynamics experiments. On the other hand, many studies have not considered any partial equilibration of the metal, implicitly assuming $k_{core} = 1$ (e.g., Wade and Wood, 2005; Fischer et al., 2015; Badro et al., 2015). Rubie et al. (2015a) and Fischer et al. (2017) tested different values of k_{core} to see which could most successfully reproduce the mantle's elemental composition, finding ranges of 0.7–1 and 0.2–1, respectively (e.g., Fig. 16).

Tighter constraints may be placed by requiring the models to reproduce the mantle's Hf–W ratio and isotopic composition (Eqs. 25–26), with Rudge et al. (2010) finding $k_{core} = 0.36$ and Nimmo et al. (2010) finding $k_{core} = 0.3$–0.8, for example. There are tradeoffs between the effects of k_{core} and core formation timing on the Earth's mantle $\epsilon_{182\mathrm{W}}$; Fischer and Nimmo (2018) concluded that any $k_{core} > 0.2$ can match the mantle's $\epsilon_{182\mathrm{W}}$ for some formation timescale, but an independent constraint on timing can result in tighter constraints on k_{core}. For example, requiring the Earth's last giant impact to occur at >65 Ma (Jacobson et al., 2014) would lead to an upper bound of $k_{core} < 0.55$ (Fischer and Nimmo, 2018), whereas the more rapid accretion rates in the Grand Tack scenario would require $k_{core} \geq 0.6$ (Zube et al., 2019).

5.3.6 Extent of silicate equilibration

The extent of silicate equilibration in each impact may be expressed as the fraction of the Earth's mantle that equilibrates (typically with a constant value in the range $0 < k_{mantle} \leq 1$) or as the mass of equilibrating silicates (m_{sil}, often expressed in terms of the impactor's mass so that larger impacts result in more silicate melting/equilibration). As with k_{core}, many studies have not considered partial equilibration of the mantle, equivalent to assuming $k_{mantle} = 1$ (e.g., Wade and Wood, 2005; Nimmo et al., 2010; Rubie et al., 2011; Siebert et al., 2012, 2013). The ability of core formation models to reproduce the mantle's elemental composition is less sensitive to the amount of equilibrating silicate than to other model parameters, so that any degree of silicate equilibration is plausible whether expressed as m_{sil} (Fischer et al., 2017) or as a fixed fraction of each impact-generated magma ocean (Gu et al., 2023), though Fischer and Nimmo (2018) found that some constraints may be placed on m_{sil} using the Hf–W system. A few studies (e.g., Rubie et al., 2015a; Suer et al., 2017; Mahan et al., 2018b) have implemented parameterizations for the extent of silicate equilibration based on fluid dynamics experiments (e.g., Deguen et al., 2011, 2014; Section 5.1). This approach may not affect the model's ability to match the Earth's composition, which can be adequately matched using a constant k_{mantle} or m_{sil}, but it can be useful in reducing the number of model parameters.

5.3.7 Bulk volatile abundances

The bulk compositions of Earth's building blocks are also an important model parameter, especially when considering volatile elements. Some studies have assumed constant volatile contents for C (Fischer et al., 2020), S (Suer et al., 2017), or H (Tagawa et al., 2021) throughout accretion, for example. For these elements, this strategy should provide an upper bound on their core abundances (e.g., Fig. 16), because more volatile-rich material from the outer Solar System tends to be accreted preferentially later in N-body simulations (e.g., Raymond et al., 2006; O'Brien et al., 2014), when the higher P–T of Earth's interior causes these elements to become less siderophile. In the extreme case of these elements only being added to the Earth during late accretion, after core formation ceased, they would not be present in the core at all.

Other studies have used multiple initial compositions, with more volatile-rich material originating in the outer Solar System (if using N-body simulations) or being added only near the end of accretion (if using an artificial mass evolution), usually with higher volatile contents coinciding with higher initial redox states of accreted materials. This type of variable volatile accretion is important in making core formation models more realistic, but it results in more model parameters that cannot be uniquely resolved.

The variable(s) defining volatile delivery in core formation models (initial volatile contents and one or more times when, or semimajor axes where, the volatile content changes) may be constrained by only adopting values that can reproduce the BSE's modern-day abundances of these elements. For example, Rubie et al. (2015a) found that the BSE's water content can be matched if accreted material from outside 6–7 AU contained 20 wt% water ice, though there are significant uncertainties in the BSE's inventories of H and other volatiles (e.g., Marty, 2012). Rubie et al. (2016) and Jennings et al. (2021) used similar models for S and C, while Blanchard et al. (2022) used four different initial C contents, for differentiated and undifferentiated bodies inside and outside of 4.5 AU. Many studies based on a continuous growth curve looking at volatiles such as S (Suer et al., 2017; Huang et al., 2021), H (Clesi et al., 2018; Tagawa et al., 2021), and Zn (Mahan et al., 2018b) find the best match to the Earth if more volatile-rich materials are added towards the end of accretion, consistent with the later accretion of more oxidized, volatile-rich material from the outer disk.

5.3.8 Timing of core formation

The timing of Earth's core formation can be investigated by coupling these models with an isotopic system like Hf–W (Eqs. 25–26). A more detailed discussion of this approach and its implications may be found in Kleine and Nimmo (this volume). In brief, a single-stage core formation model with full metal–silicate equilibration provides the earliest time at which core formation could have ended (Halliday et al., 1996), which yields a timescale of ∼30 Ma (Kleine et al., 2002; Schoenberg et al., 2002; Yin et al., 2002). However, studies that use exponential growth curves or those from N-body simulations have reported wide ranges of allowable core formation timescales, due primarily to the additional dependence of the Hf–W system on the degree of metal–silicate equilibration (e.g., Nimmo and Agnor, 2006; Dahl and Stevenson, 2010; Rudge et al., 2010). For example, Fischer and Nimmo (2018) found that Earth's $\epsilon_{182\mathrm{W}}$ can be matched for Moon-forming impact timescales spanning at least ∼10–175 Ma, depending on other model parameters.

More extensive metal–silicate equilibration (higher k_{core}, the fraction of impactor core that equilibrates, and higher k_{mantle} or m_{sil}, the fraction or mass, respectively, of silicate material that equilibrates) reduces $\epsilon_{182\mathrm{W}}$, so that lower degrees of equilibration require later core formation timescales to match the Earth's $\epsilon_{182\mathrm{W}}$. If independent constraints can be placed on either the extent of metal–silicate equilibration or the timing of core formation, this tradeoff can be exploited to constrain other model parameters. For

example, if $k_{core} = 0.55$ and $m_{sil} \geq 4\times$ the impactor's silicate mass, then Earth's core formation most likely ended at >50 Ma (Fischer and Nimmo, 2018).

Of course, there are other approaches to constraining the timing of Earth's formation in addition to Hf–W core formation modeling, such as dating terrestrial and lunar geological materials with various isotopic systems (e.g., Touboul et al., 2007; Valley et al., 2014; Borg et al., 2015) or modeling accretion dynamics with N-body simulations (e.g., O'Brien et al., 2006; Morishima et al., 2010; Chambers, 2013). A more complete picture of Earth's formation timeline may be obtained through the synthesis of these various approaches (e.g., Halliday, 2000; Lammer et al., 2021).

5.3.9 Limits on insights into core formation conditions

While core formation modeling can put some constraints on these parameters (P_{equil}, $\Delta T_{equil-liq}$, spatially- or temporally-varying fO_2, k_{core}, k_{mantle} or m_{sil}, bulk volatile contents, core formation timescale), it is difficult to obtain a unique solution due to strong tradeoffs between most parameters (Fischer et al., 2017; Fischer and Nimmo, 2018). Fig. 16 shows the evolving core formation conditions and core and mantle compositions for three Earth analogues, for three example combinations of model parameters. All three sets of parameters result in a good match to the BSE's FeO, NiO, CoO, S, and C contents but imply very different core formation conditions, bulk Earth volatile contents, and core compositions (Section 5.4) for the Earth, and different redox distributions in the disk.

These tradeoffs can be visualized by plotting the abundances of two elements against each other, such as Si in the core and NiO in the mantle (Fig. 17). Model parameters that increase or decrease both core Si and mantle NiO contents together, such as f_P and $\Delta T_{equil-liq}$, change the depth (or P–T) signature of core formation based on the P and T dependencies of these elements' metal–silicate partitioning behaviors (equation 23). This category also includes k_{core} and m_{sil}, because the extent of metal–silicate equilibration determines whether the mantle today records more of a signature of core formation on Earth's smaller precursor bodies or one of re-equilibration at great depths in the Earth. On the other hand, changing the initial fO_2 distribution in the disk changes the redox signature of core formation, increasing core Si while decreasing mantle NiO (or vice versa). Model parameters that change the depth signature trade off with each other to some extent, especially f_P, k_{core}, and m_{sil}, which have similar effects on the (core Si)/(mantle NiO) ratio (similar slopes in Fig. 17). For example, increasing f_P can be largely compensated for by simultaneously decreasing k_{core}, resulting in very little change to the Earth's final composition and making it extremely difficult to uniquely constrain either parameter (Fischer et al., 2017). Other pairs of elements may exhibit different behaviors, but most lithophile elements in the core and siderophile elements in the mantle generally follow the trends shown in Fig. 17, with some variation in slopes.

Even if some constraints can be placed on a model parameter, the interpretation of this value can be challenging, as each parameter often encapsulates complicated and time-varying processes into a single number. While each parameter is usually treated as a constant in core formation models, in reality their values may have varied secularly over time, varied from impact to impact, varied spatially, and/or varied in other ways. For example, the efficiencies of some volatile delivery and loss mechanisms would have evolved with time as the Earth's mass increased (e.g., Tian, 2015), changing the effective abundances of volatiles added to the Earth. Stochastic variability in impactor mass and impact angle and velocity would have produced variations in the depth and geometry of melting from impact to impact (e.g., Abramov et al., 2012; Nakajima et al., 2021), leading to changes in f_P and k_{mantle} (Fig. 13). Maas et al. (2021) argued that the fragmentation and settling of impactors' metal would have exhibited variations with latitude on the Earth, leading to spatially-varying k_{core} and k_{mantle}.

There are many other simplifications made in core formation models. For example, it is typically

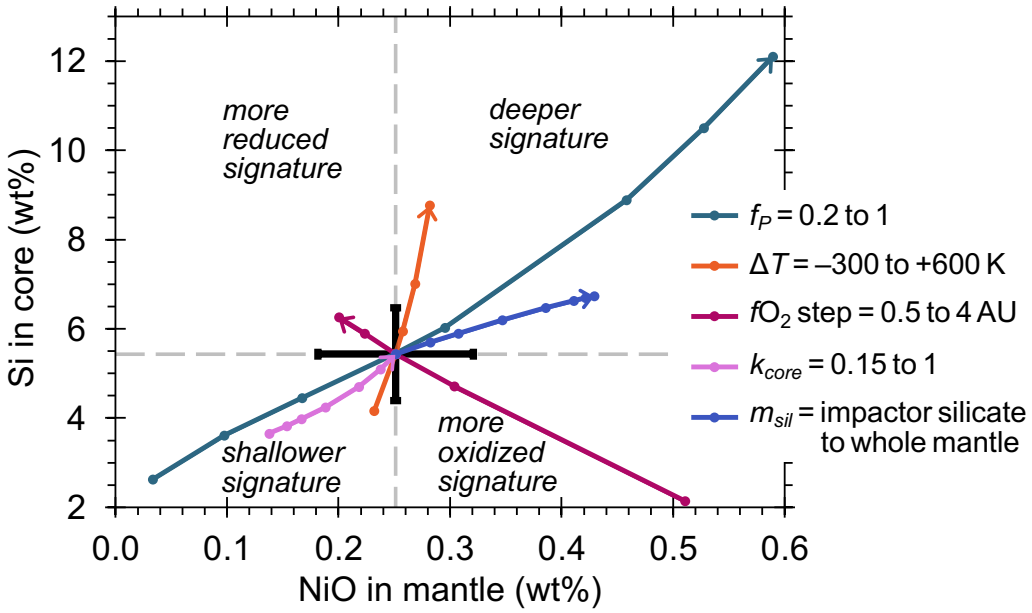

Fig. 17: Effects of varying five core formation model parameters on the Earth's core Si and mantle NiO abundances. All results are averages of 73 Earth analogues from the N-body simulations of Fischer and Ciesla (2014). Grey dashed lines are compositions from a reference set of model parameters that reproduces the BSE's composition: $f_P = 0.55$, $\Delta T_{equil-liq} = 0$, step function in initial fO_2 at 2 AU, $k_{core} = 1$, m_{sil} (mass of equilibrating silicate) = impactor's silicate mass. Black error bars represent the 2σ variability in our calculated compositions, due to variations in the provenance of accreted material in different N-body simulations. Colored curves show the effects of varying one model parameter at a time with the rest fixed at their reference values, with circles as calculated compositions, lines between them as guides to the eye, and arrows indicating the direction of increasing the parameter. $\Delta T_{equil-liq}$ is defined relative to the liquidus of Andrault et al. (2011). Initial fO_2 of Earth's building blocks is described by the location of a step from IW–3.5 to IW–1.5 with increasing semimajor axis (note that as this parameter increases, the average fO_2 of accreted materials decreases). Going from lower left to upper right is a signature of deeper (higher P–T) metal–silicate equilibration, while going from upper left to lower right is a signature of more oxidized conditions. Tradeoffs exist between model parameters, especially f_P, k_{core}, and m_{sil}, which produce Earth analogues with similar (core Si)/(mantle NiO) ratios (similar slopes). After Fischer et al. (2017).

assumed that all incoming metal is efficiently equilibrated and segregated into the core; if any portion of an emulsified impactor core remained stranded in the mantle, this would particularly affect the abundances of siderophile elements in the mantle. However, in general, the merits of incorporating more complex treatments of model parameters or processes are debatable; doing so would undoubtedly make these models more realistic, but it would likely involve an increase in the number of parameters, and it is already very difficult to constrain any parameter values while treating them as constants due to the tradeoffs between them. Constant parameter values may be thought of as effective averages over all of Earth's core formation, providing some first-order insight into this process.

5.4 Predictions of core light element abundances

The composition of the BSE (e.g., Table 4) can be reproduced by numerous combinations of core formation model parameters (Section 5.3.9), with this range of conditions corresponding to a range of possible core compositions. Fig. 16 shows examples of the final and time-evolving core compositions for three Earth analogue planets, for different sets of model parameters that all match the BSE's composition.

These results can be used to put approximate upper and lower bounds on the abundances of various light elements in the Earth's core.

5.4.1 Silicon and oxygen

The left column of Fig. 16 shows an example that maximizes the amount of silicon in the core, with relatively high values of f_P and $\Delta T_{equil-liq}$ and low initial fO_2. Silicon is particularly sensitive to these parameters, due to its partitioning being strongly dependent on T (e.g., Fischer et al., 2015) and its high valence. Using high values of f_P and $\Delta T_{equil-liq}$ can lead to very high abundances of FeO, NiO, and CoO in the BSE, but the BSE's observed composition can be recovered with a corresponding decrease in initial fO_2 (to some extent; if f_P and $\Delta T_{equil-liq}$ are too high and initial fO_2 if too low, the BSE's NiO/CoO and NiO/FeO ratios cannot be reproduced).

Exploiting this tradeoff as much as possible, we find that a maximum of ∼11–12 wt% Si in the core can be obtained while still matching the BSE's composition (Fig. 16, left column). On the other hand, with relatively low f_P and $\Delta T_{equil-liq}$ and high initial fO_2, the core only contains ∼1.7–1.9 wt% Si (Fig. 16, right column). These results indicate that there is a wide range of core Si contents that can result from core formation, but that silicon is always a major core light element in the Earth, present at the $\sim 10^0$–10^1 wt% level.

The middle column of Fig. 16 shows an example model run that maximizes the amount of oxygen in the core. As with silicon, core oxygen contents increase with core formation at higher P–T, though the partitioning behavior of O is significantly less sensitive to P–T than that of Si is (e.g., Fischer et al., 2015). Unlike silicon and most other lithophile elements, core O contents increase with increasing fO_2. This opposite trend in behavior makes it difficult to obtain very high core oxygen abundances. Increasing f_P or $\Delta T_{equil-liq}$ (or similarly, increasing k_{core} or m_{sil}) or increasing initial fO_2 all have the effect of increasing the amount of oxygen in the core, but they also all increase NiO, CoO, and FeO in the BSE, such that very high values cannot be used for all of these parameters simultaneously.

Given these constraints on core formation conditions from the BSE's composition, we find a maximum core oxygen abundance of ∼1.4–2.1 wt% (Fig. 16, middle column). Other combinations of model parameters can result in slightly lower core oxygen contents, down to <1 wt% (e.g., Fig. 16, right column). Oxygen does not exhibit as wide a range of core abundances as silicon does; it is generally always an important light element, present at the $\sim 10^{-1}$–10^0 wt% level, but it never reaches high enough abundances to dominate the core's light element budget. The final core composition typically contains more Si than O.

Previous studies have reported a range of core Si and O contents from core formation modeling. Those that used self-consistent fO_2 evolution (Section 5.3.4) predict Si and O abundances that are broadly compatible with these ranges, with more Si than O in the core (e.g., Rubie et al., 2011, 2015a; Fischer et al., 2015, 2017; Chidester et al., 2022; Gu et al., 2023). Multi-stage models with a prescribed fO_2 evolution yield similar trends in core Si and O contents, if they use either a constant fO_2 equal to its modern value or redox conditions that evolve from reduced to oxidized as the Earth grows (e.g., Ricolleau et al., 2011). On the other hand, multi-stage models that impose an fO_2 evolution from oxidized to reduced typically predict more O than Si in the core, with abundances in the ranges ∼2.7–5 wt% and ∼1.5–3.6 wt%, respectively (e.g., Siebert et al., 2013; Badro et al., 2015).

5.4.2 Sulfur and carbon

For volatile elements like S and C, results of core formation models are extremely sensitive to the assumed initial composition(s) of Earth's building blocks. Often, those compositions are chosen so that

the model reproduces the BSE's volatile contents. Core formation conditions that make these elements more siderophile result in lower BSE abundances, requiring higher bulk Earth volatile contents to match the BSE and maximizing their abundances in the core. In these calculations, we assume constant bulk C and S abundances for the Earth's building blocks and neglect any contribution from late accretion, which should also yield an upper bound on their core abundances (Section 5.3.7).

An example of this approach is shown in the right column of Fig. 16. Model parameters were chosen to approximately maximize the siderophility of sulfur based on its metal–silicate partitioning behavior (Suer et al., 2017), resulting in an upper bound on core sulfur of ∼3.3 wt%. Interestingly, this core S abundance is in excellent agreement with that estimated from geo-/cosmochemical constraints based on volatile depletion trends in NC meteorites (Section 3.4; Table 6). Parameters that lead to the highest core sulfur contents correspond to some of the lowest core Si and O contents. Conversely, model parameters that maximize core Si and O contents lead to the lowest levels of sulfur in the core. In these calculations, we found a lower bound of ∼0.5 wt% S in the core, though this number could be significantly lower if sulfur was preferentially accreted later in Earth's growth history and/or if late accretion contributed notably to the BSE's sulfur budget (Morgan, 1986; McDonough and Sun, 1995). Most literature studies on S partitioning also report core sulfur contents in this range (e.g., Boujibar et al., 2014; Suer et al., 2017; Mahan et al., 2018a; cf. Chidester et al., 2022). Overall, this suggests that Earth's core sulfur content is on the order of $\sim 10^{-1}$–10^{0} wt%, similar to or slightly lower than Si and O abundances, though lower levels of S may also be possible.

Core carbon contents are relatively high under core formation conditions that also lead to the highest core oxygen abundances (Fig. 16, middle column). Changes to model parameters can produce only slightly higher core C, with a maximum of ∼0.15 wt% in this example, similar to our estimate of 0.2 wt% from geo-/cosmochemical constraints (Table 4). Core carbon contents are lowest for conditions that maximize core S (Fig. 16, right column). Here we find a lower bound of ∼0.016–0.017 wt% C, though as with sulfur, this number is likely to be significantly lower when considering more realistic volatile delivery histories. These calculations use the metal–silicate partitioning parameterization for carbon from Fischer et al. (2020) (equation 24). Blanchard et al. (2022) reported more siderophile behavior for C, so using their parameterization instead with the same model should result in higher levels of core C; they report ∼0.13 wt% carbon in the core using a different modeling approach. Using first-principles calculations of carbon metal–silicate partitioning, Zhang and Yin (2012) concluded that the core could contain ∼0.1–0.7 wt% C. Therefore, carbon is most likely present in the Earth's core at the $\sim 10^{-2}$–10^{-1} wt% level, significantly lower than core Si, O, and S abundances, but higher or lower levels of core C may be plausible too.

Though S and especially C are probably not the single most abundant light element in the Earth's core, the core still represents the largest reservoir of these elements in the planet due to their siderophile partitioning behaviors. The ranges of core S and C reported here imply that the core contains ∼92–99% and ∼40–86%, respectively, of the Earth's budgets of these elements, consistent with our independent estimate of S in the core based on geo-/cosmochemistry (Section 3.6; Table 7). Understanding their core abundances is therefore critical to constraining the bulk Earth abundances of these elements, with implications for the nature of Earth's building blocks, habitability, and volatile delivery/loss processes.

5.4.3 Hydrogen

H was not included in the calculations shown in Fig. 16, but several previous studies have put constraints on its core abundance based on metal–silicate partitioning experiments and core formation calculations. In general, hydrogen is less well-studied than Si, O, S, and C, in large part due to experimental and analytical limitations on determining its partitioning behavior at extreme P–T, and more work is needed

to understand its behavior during Earth's core formation. For example, only one experimental study has been published on the metal–silicate partitioning of H above ∼20 GPa (Tagawa et al., 2021).

High P–T experimental studies on hydrogen partitioning generally fall into two groups: those that report strongly siderophile behavior and high core abundances of ∼3000–6000 ppm H (e.g., Okuchi, 1997; Tagawa et al., 2021), and those that report less siderophile or even lithophile behavior, with correspondingly lower core hydrogen abundances. For example, Clesi et al. (2018) predicted ∼60 ppm H in the core, and Malavergne et al. (2019) reported a wider possible range of ∼5–3000 ppm H. Several ab initio studies have also investigated the metal–silicate partitioning of hydrogen, with a similar extent of disagreement over its siderophility (Zhang and Yin, 2012; Li et al., 2020b; Yuan and Steinle-Neumann, 2020). The higher core H estimates on the order of $\sim 10^{-1}$ wt% would imply that hydrogen may be an important contributor to the core's density deficit, whereas the lower estimates of $\sim 10^{-4}$–10^{-3} wt% would mean that it does not play a major role.

There are a number of factors that may contribute to these discrepancies between experimental studies on hydrogen partitioning. It is very difficult to achieve high P–T conditions in H-bearing experiments, and to quantitatively determine the H abundances of the metallic and silicate melts after equilibration, due to the high diffusivity and volatility of hydrogen. Gaillard et al. (2022) proposed that different results for H partitioning could be partly due to differences in speciation in the silicate melt at different conditions, while Tagawa et al. (2021) suggested that the carbon content of the metal may play a role. Many experimental studies on the behavior of hydrogen are H-saturated, such that the hydrogen contents reported are actually solubilities, which may differ substantially from those resulting from partitioning under H-undersaturated conditions.

Furthermore, there is the possibility of extensive H loss from metallic iron following decompression and/or conversion to the bcc structure. Numerous studies have reported high solubilities of hydrogen in metallic iron at high P–T in the fcc, (d)hcp, or liquid phase, with little or no solubility at lower P–T in the bcc phase. For example, Iizuka-Oku et al. (2017) measured ∼0.6–0.7 wt% deuterium in fcc iron (equivalent to FeD_x with $x \approx 0.2$) using in situ neutron diffraction at high P–T, with no measurable deuterium in the metal of the recovered sample at ambient conditions, only vesicles (a common feature in decompressed FeH_x samples). Similarly, Machida et al. (2014) reported synthesizing fcc $FeD_{0.64}$ based on in situ neutron diffraction analyses at high P–T, with no detectable deuterization of Fe at lower T where the bcc structure is stable. Other studies have reported similar behavior using X-ray diffraction to determine the volume expansion of the Fe lattice in situ as an indicator of H content, or other approaches (e.g., Fukai and Suzuki, 1986; Okuchi, 1997; Ohtani et al., 2005; Shibazaki et al., 2009; Terasaki et al., 2012; Yuan et al., 2018; Kim et al., 2023). For example, Tagawa et al. (2021) reported the synthesis of hcp $FeH_{1.8}$ at 60 GPa and 4600 K, as well as fcc FeH_x with $x = 0.2$–0.5 at more moderate P–T. After subsequent decompression to atmospheric pressure, their sample exhibited the same lattice parameter as pure Fe, and it did not form FeH when compressed again, suggesting that the hydrogen escaped (Tagawa et al., 2021). It is well-documented that H has an extremely low solubility in Fe metal at low P–T, with Vrbek et al. (2015) finding that only a few ppm or less of hydrogen can be dissolved into steel at atmospheric pressure, for example.

It is possible that the studies reporting less siderophile behavior of H based on ex situ chemical analyses of run products at ambient conditions (Clesi et al., 2018; Malavergne et al., 2019) suffered from hydrogen loss from the metal. If so, their results would represent lower bounds on D_H and thus core H contents. However, even though high pressure phases of Fe can take in significant H, that does not necessarily mean that a molten iron alloy in equilibrium with a silicate melt under hydrogen-undersaturated conditions will take in significant H. As an analogy, the solubility of Si in liquid Fe is extremely high at high P–T (e.g., Edmund et al., 2022), but the Earth's core cannot contain tens of wt% silicon, despite its high abundance in the BSE, because Si is too lithophile (e.g., Bouhifd and Jephcoat, 2011; Ricolleau et al.,

2011; Tsuno et al., 2013; Fischer et al., 2015). The high observed solubility of H in iron thus provides an upper bound on the core's H content. There remains a great need for more metal–silicate partitioning data on H at very high P–T, with lower (undersaturated) bulk hydrogen contents and better in situ techniques for measuring H abundances.

Even if the metal–silicate partitioning behavior of hydrogen were perfectly understood, there would remain large uncertainties in core H content due to uncertainties over different mechanisms for hydrogen delivery to the Earth and incorporation into the core. As with other volatiles, we do not know exactly how much hydrogen the bulk Earth contains. If hydrogen was preferentially delivered later in Earth's accretion, it may have experienced different conditions of core formation (e.g., higher P–T); in the endmember scenario in which all of Earth's hydrogen was added only after core formation ceased (via late accretion), it would not have participated in core formation at all. For example, Rubie et al. (2015a) modeled the behavior of H during Earth's accretion and core formation, with a more volatile-rich outer disk. Despite treating H as infinitely siderophile, they found the best match to the BSE for model parameters that resulted in only ∼10–60 ppm H in the core (Rubie et al., 2015a). On the other hand, the model of Young et al. (2023), in which the Earth is built from bodies with H-rich primary atmospheres, is consistent with ∼0.5 wt% hydrogen in the Earth's core, making it the dominant contributor to the core's density deficit. Furthermore, even if the Earth's core formed with a low H content, several studies (e.g., Ohtani, 2021; Kim et al., 2023) have proposed that hydrous phases in subducted slabs could later transport H to the core due to its high diffusivity.

5.4.4 Other possible light elements

Francis Birch famously described the Earth's "pure iron" core as an "uncertain mixture of all the elements" (Birch, 1952). In addition to the most likely core light elements discussed above, there are many other elements whose abundances in the core are crucial to our understanding of various deep Earth processes, including Mg and other lithophile elements, and other volatiles like N and noble gases.

A few experimental studies on the metal–silicate partitioning of Mg have suggested that it becomes less lithophile at higher P–T (Badro et al., 2016; Du et al., 2019). The strong T-dependence of its solubility in Fe-rich metal has inspired the suggestion that MgO may have exsolved from the Earth's core during secular cooling and helped drive the geodynamo (e.g., O'Rourke and Stevenson, 2016). Based on their findings, Badro et al. (2018) suggest that the core could have contained ∼0.5 wt% Mg (or ∼0.8 wt% MgO) when it formed, decreasing to ∼0.3 wt% Mg in the present-day due to exsolution, in agreement with the compositions reported by Chidester et al. (2022). Other lithophile elements such as Al and Ca are likely present in the core in non-zero abundances too, but at lower abundances than Mg for the same core formation conditions (e.g., Chidester et al., 2022). If the core's magnesium abundance is on the order of $\sim 10^{-1}$ wt%, Mg would be only a minor contributor to the density deficit, but may be sufficiently abundant as to be an important energy source for the dynamo, especially before inner core crystallization.

Nitrogen partitioning is very sensitive to fO_2, with more siderophile behavior under more oxidized conditions. This behavior, similar to that of oxygen, is generally the opposite trend as seen with cations, consistent with N dissolving in the silicate melt as N^{3-} (Libourel et al., 2003). Combined with the dependencies of nitrogen partitioning on other variables, previous studies have found that N becomes more siderophile toward the later stages of Earth's growth (e.g., Dalou et al., 2017; Grewal et al., 2019a; Jackson et al., 2021). An ab initio study of N partitioning (Zhang and Yin, 2012) reported that the Earth's core should contain on the order of ∼1s–10s ppm ($\sim 10^{-4}$–10^{-3} wt%) nitrogen, with most experimental studies (e.g., Grewal et al., 2019a; Speelmanns et al., 2019; Shi et al., 2022) reporting slightly higher core N abundances of ∼10s–100s ppm ($\sim 10^{-3}$–10^{-2} wt%), or possibly even higher (Grewal

et al., 2019a). These values are broadly consistent with independent geochemical estimates (e.g., 75 ppm; Table 4). As with carbon (Section 5.4.2), it is unlikely that nitrogen is sufficiently abundant in the Earth's core to affect its density or other physical properties, but the core is likely the largest reservoir of N in the planet.

The metal–silicate partitioning behaviors of helium and other noble gases have been investigated using both experimental and computational approaches (e.g., Matsuda et al., 1993; Zhang and Yin, 2012; Bouhifd et al., 2013, 2020; Yuan and Steinle-Neumann, 2021), though experimental data are lacking at Earth's core formation conditions. There is some disagreement over their partition coefficients at high P–T, which may be due to the unique experimental challenges posed by such highly volatile elements; for example, they might be degassed from samples during depressurization, making it difficult to accurately determine their partition coefficients. Given their lithophile behaviors and low abundances in the BSE, noble gases are unlikely to contribute significantly to the density or other physical properties of Earth's core, but they may be present in suffuciently high abundances as to influence the isotopic compositions of ocean island basalts originating near the core–mantle boundary (e.g., Herzberg et al., 2013). Other elements, such as phosphorus (e.g., Righter et al., 2010; Siebert et al., 2011; Ikuta et al., 2024), have also been investigated, but are similarly unlikely to be dominant light elements in Earth's core.

5.4.5 Summary and outlook

Here we have focused on assessing the possible ranges of light element abundances in the Earth's core as a result of core formation, as a way to constrain the core's composition. However, many other groups of elements are likely present in the core in sufficiently high abundances as to be important to other processes. For example, the metal–silicate partitioning behaviors of Th, U, and K have been widely studied to constrain their roles in the core's thermal budget (e.g., Gessmann and Wood, 2002; Corgne et al., 2007; Malavergne et al., 2007; Blanchard et al., 2017; Faure et al., 2020; Chidester et al., 2022), and knowledge of the core abundances of moderately and highly volatile elements can help elucidate the Earth's volatile depletion trend and its origins (e.g., Mahan et al., 2018a,b; Siebert et al., 2018; Vogel et al., 2018; Bouhifd et al., 2020).

Table 12 summarizes our constraints on the core's light element composition based on high P–T metal–silicate partitioning experiments and numerical modeling of core formation. Si, O, and S are all likely present at wt% levels in Earth's core, with more silicon than oxygen. The next most-abundant light elements (Table 12) are likely C and H, with smaller amounts of other elements. We cannot establish minimum core abundances for volatile elements that may have partly been delivered to the Earth during late accretion; in the limit that the entire BSE inventories of these elements came from late accretion, they would not be present in the core at all. Furthermore, not all combinations of light element abundances shown in Table 12 are plausible; for example, the model parameters that maximize the core's S content result in the lowest Si and O contents (Fig. 16).

Some candidate core light elements will likely benefit from more metal–silicate partitioning experiments. For example, the two published studies on carbon partitioning in an LH-DAC disagree somewhat (Fischer et al., 2020; Blanchard et al., 2022), the only study on H partitioning at these P–T (Tagawa et al., 2021) should be verified, and the partitioning of nitrogen should be studied to higher P–T (Jackson et al., 2021). But for most light elements, the dominant uncertainties in their core abundances come from either uncertainties in the mechanisms of core formation (Section 5.3) and/or uncertainties in the timing and mechanisms of volatile delivery and loss (Section 5.3.7). Insights into the mechanisms of core formation from different types of studies (Section 5.1) may be incorporated into these core formation models (e.g., Rubie et al., 2015a; Gu et al., 2023) to make them more realistic without introducing a large number of model parameters. Volatile depletions can be better understood through the study of late accretion,

Table 12: **Constraints on light element abundances in the Earth's core from metal–silicate partitioning experiments and core formation modeling**

Element	Range expected in core[1]	References
Si	∼1.7–12 wt%	Fischer et al. (2015); this study
O	∼0.8–2.1 wt%	Fischer et al. (2015); this study
S	∼0–3.3 wt%[2]	Suer et al. (2017); this study
C	∼0–0.15 wt%[2]	Fischer et al. (2020); this study
H	∼0–0.6 wt%[2,3]	e.g., Rubie et al. (2015a); Clesi et al. (2018); Malavergne et al. (2019); Tagawa et al. (2021)

[1] Not all combinations of light elements within these ranges are possible. For example, higher pressures of equilibration and more reducing conditions increase core Si but decrease O and S.
[2] Minimum values cannot be established for volatile elements due to uncertainties in the contributions from late accretion.
[3] It may be possible for core H to increase later in Earth history via reactions with subducted slabs at the CMB (e.g., Ohtani, 2021).

the volatile contents of Earth's building blocks, and loss due to impacts, magma ocean outgassing and crystallization, hydrodynamic escape, etc.

5.5 Constraints on core composition from metal–silicate stable isotope fractionation

The isotopic composition of the bulk silicate Earth is often used to understand the nature of the Earth's building blocks and how this accreted material may have changed over time (e.g., Fitoussi and Bourdon, 2012; Dauphas, 2017; Dauphas et al., 2024). In particular, some studies have found that the BSE has ratios of $^{34}S/^{32}S$ and $^{30}Si/^{28}Si$ that are different from those of chondritic meteorites (Georg et al., 2007; Fitoussi et al., 2009; Labidi et al., 2013). If the bulk Earth has a chondritic isotopic composition for these elements, their non-chondritic ratios in the BSE may be due to metal–silicate isotopic fractionation during core formation. A detailed understanding of the isotopic compositions of the BSE and chondrites, combined with experimental or theoretical results on metal–silicate isotopic fractionation, can then be used to constrain the abundances of these elements in the Earth's core. At present, this approach bears considerable uncertainty, due in part to the lack of experimental data at appropriately high P–T.

Labidi et al. (2016) performed experiments on S isotopic fractionation during core formation, finding that it is a "viable hypothesis" to explain the BSE's S isotopes, though the exact magnitude of fractionation (and thus the required S content of the core) remains unknown due to pressure effects. Mahan et al. (2017) investigated Zn isotopic fractionation to estimate the Zn content of the core. Assuming a chondritic S/Zn ratio, they found an upper bound of 6.3 ± 1.9 wt% S in Earth's core.

More work has been done on the isotopic fractionation of silicon during core formation than that of any other candidate core light element. While these studies disagree on the exact magnitude of the expected fractionation, most conclude that there must be at least a few weight percent of Si in the core, and possibly an unrealistically high amount (e.g., Shahar et al., 2009, 2011; Armytage et al., 2011; Zambardi et al., 2013; Hin et al., 2014). While these results are consistent with Si being an important core light element, more work is needed to understand the variations between studies, pressure effects, and nature of Earth's building blocks before this method can provide a tighter constraint on core Si abundance.

Shahar et al. (2016) showed that the extent of Fe isotopic fractionation during core formation at high

P–T depends on which light elements are present. They argued that if the bulk Earth has chondritic Fe isotopes, H and C cannot be the dominant light elements in the core, because their presence at those levels would have caused a large Fe isotopic fractionation during core formation that is not observed. However, Liu et al. (2017) found that none of the candidate core light elements have a large enough effect on iron isotopic fractionation to be resolvable using this approach.

6 Future opportunities in geoneutrino science

Advances in science often accompany developments in technologies. This concept is particularly true for advances in understanding the physical and chemical state of the Earth's core at its initial and current conditions, since the core is the most remote and inaccessible part of the planet. Here we review a few possibilities for future advances in our understanding of the core based on new technologies using geoneutrinos.

Neutrino science offers another entirely different realm of technology development. In 2005, particle physicists first detected the Earth's emission of geoneutrinos (electron antineutrinos emitted during β^- decay) (Araki et al., 2005; McDonough, 2005). Over the ensuing two decades of research, great strides have been made, new detectors have begun counting or are about to begin counting, and tighter constraints are being placed on the radiogenic power of the Earth (McDonough and Watanabe, 2023).

Two significant issues remain with respect to the detection of geoneutrinos: (1) the inability to measure geoneutrinos emitted from the potassium decay chains; and (2) existing detectors are directionless — that is, they are incapable of identifying the direction from which the dominant signal is derived. Great research efforts are being invested in both problems. Recently, particle physicists have proposed and tested a new method for detecting geoneutrinos emitted from the potassium decay chains (Cabrera et al., 2023). Although further development is needed, this new technology shows considerable promise. Second, the nuclear reactor industry is the major driving force in making detectors directionally capable. There is considerable usefulness in being able to point back to a specific reactor location as the source emitter of specific electron antineutrinos. In geoscience, a directional detector would vastly improve our spatial insights into the strength of the signal from the crust versus the mantle. Also, such detectors could examine the likelihood of the core being a host for K, Th, and/or U.

In other neutrino spectrometry studies, particle physicists have been developing technologies to sense the Earth's electron density and matter density state of the planet (Donini et al., 2019). Geoneutrino studies focus on the detection of 1.8–3.3 MeV antineutrinos. Neutrino oscillation studies use 2–8 GeV neutrinos to sense the electron density state of the Earth's interior (Rott et al., 2015; Maderer et al., 2023). Neutrino absorption studies use $\geq$10 TeV neutrinos to sense the mass density state of the Earth's interior (Van Elewyck et al., 2021). These latter high energy neutrinos are products of high energy cosmic ray–air collisions in the atmosphere or of interstellar sources of cosmic rays that interact with matter during their transit through the Universe.

Neutrino oscillation spectroscopy is sensitive to the electron density state of matter: Z/A, where Z is the atomic number (i.e., number of protons, n_p) and A is the atomic mass or total number of nucleons. Therefore, this technique is most sensitive to the Earth's hydrogen content ($Z/A = 1/1 = 1$) at a given depth and less sensitive to every other element, which have Z/A values of $\sim$0.5. Neutrinos are sensitive to the effects of Earth's matter during their planetary transit inside the Earth (i.e., during such transits, a neutrino repeatedly oscillates from the electron to muon to tau states). This electron sensitivity is due to a neutrino's coherent and forward scattering with ambient electrons. Only electrons are relevant for oscillation tomography, given their presence inside the Earth.

The number of electrons (n_e) inside the Earth (or any other given matter) is its electron fraction:

$E_f = \frac{\#\ of\ electrons}{gram} = \sum(WF_i \times Z_i/A_i)$, where WF_i is the weight fraction of element i and $n_e = n_p$ for electrically neutral materials. However, because of their compositional differences, the core and mantle have different electron fractions. For a typical oscillation analysis, assuming the compositional model given in Table 6, we have $(Z/A)_{core} = 0.4611$ and $(Z/A)_{mantle} = 0.4923$. By comparison, the core model envisaged by Young et al. (2023), with ~0.5 wt% H, has a $(Z/A)_{core} = 0.4708$ and $(Z/A)_{mantle} = 0.4921$. These Z/A estimates can be tested with high-precision oscillation data to evaluate the chemical composition of the Earth, specifically testing models for the hydrogen content of the core (Rott et al., 2015; Maderer et al., 2023). However, these analyses will take another 50 years or less to come to fruition, even with the benefit of combining signals from multiple instruments, given future instrument construction and development and the necessary exposure time (i.e., for flux of 2–8 GeV neutrinos and zenith angles >147°).

Neutrinos are known to only interact via the weak and gravity forces. However, at high energies (≥1 GeV), because the cross section of a neutrino is dominated by deep inelastic scattering, neutrino–nucleon interactions become possible. It has been demonstrated that neutrino interaction cross sections correlate with their increasing energy (measured up to 980 TeV neutrinos) and are scattered (i.e., absorbed) due to the presence of matter (Andeen et al., 2017; Reno, 2023). Therefore, sensing the mass density state of the Earth requires neutrinos with energies ≥10 TeV. At these energies we have neutrino absorption spectroscopy, which measures the attenuated flux of high-energy neutrinos taking long paths through the Earth (i.e., zenith angles >147°) versus others following shorter paths.

Currently, there are only long term (~50 year time frame or less) prospects from neutrino absorption spectroscopy for insights into the properties of the core, which include: core mass, planet mass, depth to the core–mantle boundary, and perhaps more. Current estimates place the core's mass at $(1.93 \pm 0.04) \times 10^{24}$ kg, based on Earth's mass and moment of inertia. Early results from about a decade of IceCube data show promise, as this independent estimate already offers about ±15% uncertainty on the mass of the core (Upadhyay et al., 2023).

These and other results from such neutrino studies are essentially free and on the horizon, as physicists will continue to extract all of the physics results possible from these massive experiments. Moreover, because of the phenomenal science that has come from this field in recent years and how it has created a new field of science, particle astrophysics, many new and bigger instruments are being built, developed, and planned, offering many fruitful opportunities for collaborations between the Earth science and neutrino communities.

It has been suggested that the Earth's Fe–Ni-rich inner core could be a superionic hydride, possibly also containing silicon, oxygen, and/or carbon (He et al., 2022; Wang et al., 2021b; Sun et al., 2023). A superionic alloy simultaneously possess the properties of a liquid and a solid, with the non-hydrogen components defining an organized crystalline structure while hydrogen is free-floating within this lattice (Cavazzoni et al., 1999). Hydrogen is the driving element for the superionic behavior, as it is the fastest diffusing element, an attribute needed for reaching this superionic state. Moreover, its mobility in a high P–T iron hydride allows hydrogen to be in a superionic state, where it can be a superionic conductor that is as conductive as is typical of metals. The existence of phases in a superionic state in the inner core would be consistent with its low shear velocity and density compared to an Fe–Ni alloy. If the inner core is comprised of a superionic compound (He et al., 2022; Wang et al., 2021b; Sun et al., 2023), that would indicate that the bulk core has a high hydrogen content. Thus, future evaluation of a superionic inner core awaits critical tomography measurements of the planet's neutrino oscillation spectra.

7 Conclusions

The Earth's large metallic core is an Fe–Ni–light element alloy. It is crucial to understand the identities and abundances of the core's light elements (e.g., Si, O, S, C, H), because doing so would dramatically improve our understanding of dynamo generation, accretion and core formation, volatile delivery/loss, the core's thermal structure (and thus heat flux into the mantle), the Earth's bulk composition, and many other important properties and processes in the deep Earth. Here we have summarized results from several different approaches for constraining core composition. While a huge amount of progress has been made in recent decades, significant uncertainties and inconsistencies remain.

A geochemical approach to constraining the core's composition (Section 3) involves comparing the compositions of the BSE and the bulk Earth, which is based on a refractory element enriched chondritic composition, with the difference between them indicating the composition of the core. This approach is particularly useful for sulfur, because it provides a unique way to estimate the amounts of volatile elements like S in the bulk Earth. Since S is also siderophile, constraining its abundance in the core depends strongly on having a reliable estimate of the bulk Earth's composition, including for volatiles. Using the volatile depletion trends of NC meteorites (Fig. 5), the core can contain ∼3.3 wt% S.

Mineral physics experiments and calculations can also help constrain the core's composition. Comparing the seismologically-determined density structure of the core with the densities of iron and Fe–light element alloys (Section 4.1) provides constraints on how much of each light element is needed to match the core density deficit. For example, this approach yields maximum outer core abundances (the amount of each light element needed to match the core density if it is the sole light element) of ∼7.9–8.8 wt% Si, ∼6.6–7.2 wt% O, ∼9.9–15.8 wt% S, ∼6.1–8.8 wt% C, or ∼0.4–2.2 wt% H (Table 10). A similar calculation could be performed based on seismic velocities (Section 4.2); however, there are not many experimental sound velocity measurements at core pressures or temperatures, with most data from 300 K, so any comparison to the core requires large extrapolations and assumptions about thermal effects. These mineral physics approaches are limited by uncertainties in the properties of the core, pure Fe, and iron alloys. There are only limited experimental data on the properties of liquids at outer core conditions or on solids at the extreme P–T of the inner core, and there are significant uncertainties in experimental measurements of P and T. Future studies could benefit from continuing to push these measurements to higher P–T, improving techniques to study liquids, and investigating ternary or higher-order alloys.

A third mineral physics approach is based on liquidus phase relations (Section 4.3): the core's composition must crystallize a denser (Fe-rich) liquidus phase, and it must produce a compositional difference between the solid and liquid that is consistent with the core's ICB density contrast. Considering binary and ternary systems, some oxygen may be required in order to crystallize an Fe-rich inner core. To explain the ICB density contrast, it appears that some O and/or C is necessary, but they likely partition too strongly into the liquid, such that other light elements (Si, S, and/or H) are also required. Future advances may come from more data at higher P–T and from more data in general, especially for multicomponent systems. Robust density and/or velocity data for multicomponent solid and liquid alloys are required to compare compositional measurements to seismological observables. Mineral physics data on other core properties can also provide compositional constraints (Section 4.4); for example, the inner core's high Poisson's ratio may require the presence of C, H, and/or Si.

Alternatively, insights into core composition can come from considering how much of each light element should have gone into the core during its formation, by combining models of core formation with metal–silicate partitioning data (Section 5). Core formation is a complex process; while considerable advances have been made in understanding this process, it is inherently greatly simplified in models. Considering a wide range of parameter space with self-consistent fO_2 evolution, the core may contain ∼2–12 wt% Si, ∼0.8–2.1 wt% O, ∼0–3.3 wt% S, and ∼0–0.15 wt% C (Table 12; note that not all combinations

within these ranges are possible). Future studies will benefit from an improved understanding of Earth's accretion, core formation, volatile delivery/loss, and bulk volatile contents, as well as more metal–silicate partitioning data at higher P–T and improved analytical techniques to better understand these experiments (especially for C and H).

We emphasize that the various approaches used here to constrain the core's light element composition are completely independent of each other and are based on different types of data. The maximum amount of each light element in the core reported in Table 10 is based solely on density. This provides an upper bound for each light element, and a rough guide to how much total light element the core should contain, but otherwise does not indicate whether the core contains more C or Si, for example. On the other hand, the allowed range of each light element in the core reported in Table 12 is based solely on metal–silicate partitioning and core formation modeling, and not all combinations of light element abundances within these ranges are possible. This approach provides some insight into which light elements should be more abundant than others (e.g., more Si than C), but does not take into consideration any geophysical properties of the core. The actual composition of the core must be consistent with all of these constraints simultaneously. We hope that as our understanding of the geochemistry, mineral physics, and formation of the core continue to improve, future studies will be able to further narrow the range of possible core compositions consistent with all available constraints until a unique solution can be obtained.

Geoneutrinos offer an exciting prospect for new constraints on core composition in the future, especially for hydrogen (Section 6). Recent and upcoming studies on the cores of other planetary bodies may also offer insights into cores in general. For example, returning to decades-old Apollo seismic data, complemented with more recent satellite data, has provided better constraints on the depth and nature of the lunar core (Weber et al., 2011). A multi-year deployment of a Martian seismometer has yielded significant insights into the depth, density, and nature of the core of Mars (Irving et al., 2023; Khan et al., 2023; Samuel et al., 2023). NASA's Messenger mission to Mercury has provided evidence for a liquid iron-rich core and the possible presence of a solid inner core (Smith et al., 2012). The next two decades promises to be equally exciting for the studies of Earth and planetary cores.

While the composition of Earth's core remains uncertain, many recent advances have allowed for narrowing down the range of possible compositions and considering more realistic, multicomponent core alloys. Combining multiple independent constraints, such as those based on geochemistry/cosmochemistry, various mineral physics approaches, and core formation, may provide unique insights into Earth's core composition. Such a multi-pronged approach may ultimately be necessary to narrow down the range of possible compositions for this enigmatic yet critically important central region of our planet.

Author Contributions: RAF and WFM contributed to the conceptualization and investigation of this project. RAF and WFM wrote and edited this manuscript, with Sections 1–3 and 6 principally written by WFM and Sections 4–5 and 7 by RAF. Both authors have read and approved this manuscript.

Acknowledgments: We are grateful to Eiji Ohtani and Bill White for their detailed and thoughtful reviews of this chapter, and to Catherine Chauvel for her editorial handling and patience. We thank Miaki Ishii, Francis Nimmo, Andy Campbell, Jesse Gu, Stéphane Labrosse, Ved Lekić, and Eiji Ohtani for helpful discussions. RAF was partially supported by a NASA Emerging Worlds grant (80NSSC21K0388) and an NSF CSEDI grant (EAR-2054912). WFM gratefully acknowledges the NSF for support (grant EAR-2050374).

References

Abramov, O., Wong, S.M., Kring, D.A., 2012. Differential melt scaling for oblique impacts on terrestrial planets. Icarus 218, 906–916.

Alexander, C.M.O., 2019a. Quantitative models for the elemental and isotopic fractionations in chondrites: The carbonaceous chondrites. Geochimica et Cosmochimica Acta 254, 277–309. doi:10.1016/j.gca.2019.02.008.

Alexander, C.M.O., 2019b. Quantitative models for the elemental and isotopic fractionations in the chondrites: The non-carbonaceous chondrites. Geochimica et Cosmochimica Acta 254, 246–276. doi:10.1016/j.gca.2019.01.026.

Alfè, D., Gillan, M.J., Price, G.D., 2000. Constraints on the composition of the Earth's core from *ab initio* calculations. Nature 405, 172–175.

Alfè, D., Gillan, M.J., Price, G.D., 2002a. Composition and temperature of the Earth's core constrained by combining *ab initio* calculations and seismic data. Earth and Planetary Science Letters 195, 91–98.

Alfè, D., Gillan, M.J., Price, G.D., 2002b. *Ab initio* chemical potentials of solid and liquid solutions and the chemistry of the Earth's core. Journal of Chemical Physics 116, 7127–7136.

Alfè, D., Price, G.D., Gillan, M.J., 2002c. Iron under Earth's core conditions: Liquid-state thermodynamics and high-pressure melting curve from *ab initio* calculations. Physical Review B 65, 165118.

Allègre, C.J., Poirier, J.P., Humler, E., Hofmann, A.W., 1995. The chemical composition of the Earth. Earth and Planetary Science Letters 134, 515–526. doi:10.1016/0012-821X(95)00123-T.

An, Y., Ding, H., Chen, Z., Shen, W., Jiang, W., 2023. Inner core static tilt inferred from intradecadal oscillation in the Earth's rotation. Nature Communications 14, 8130.

Andeen, K., Collaboration, I., et al., 2017. Measurement of the multi-TeV neutrino interaction cross-section with IceCube using Earth absorption. Nature 551, 596–600.

Anderson, O., Isaak, D., 2002. Another look at the core density deficit of Earth's outer core. Physics of the Earth and Planetary Interiors 131, 19–27.

Andrault, D., Bolfan-Casanova, N., Lo Nigro, G., Bouhifd, M.A., Garbarino, G., Mezouar, M., 2011. Solidus and liquidus profiles of chondritic mantle: Implication for melting of the Earth across its history. Earth and Planetary Science Letters 304, 251–259.

Andrault, D., Fiquet, G., Itié, J.P., Richet, P., Gillet, P., Häusermann, D., Hanfland, M., 1998. Thermal pressure in the laser-heated diamond-anvil cell: An X-ray diffraction study. European Journal of Mineralogy 10, 931–940.

Antonangeli, D., Komabayashi, T., Occelli, F., Borissenko, E., Walters, A.C., Fiquet, G., Fei, Y., 2012. Simultaneous sound velocity and density measurements of hcp iron up to 93 GPa and 1100 K: An experimental test of the Birch's law at high temperature. Earth and Planetary Science Letters 331–332, 210–214.

Antonangeli, D., Merkel, S., Farber, D.L., 2006. Elastic anisotropy in hcp metals at high pressure and the sound wave anisotropy of the Earth's inner core. Geophysical Research Letters 33, L24303.

Antonangeli, D., Morard, G., Paolasini, L., Garbarino, G., Murphy, C.A., Edmund, E., Decremps, F., Fiquet, G., Bosak, A., Mezouar, M., Fei, Y., 2018. Sound velocities and density measurements of solid hcp-Fe and hcp-Fe–Si (9 wt.%) alloy at high pressure: Constraints on the Si abundance in the Earth's inner core. Earth and Planetary Science Letters 482, 446–453.

Antonangeli, D., Ohtani, E., 2015. Sound velocity of hcp-Fe at high pressure: experimental constraints, extrapolations and comparison with seismic models. Progress in Earth and Planetary Science 2, 3.

Anzellini, S., Dewaele, A., Mezouar, M., Loubeyre, P., Morard, G., 2013. Melting of iron at Earth's inner core boundary based on fast x-ray diffraction. Science 340, 464–466.

Araki, T., Enomoto, S., Furuno, K., Gando, Y., Ichimura, K., Ikeda, H., Inoue, K., Kishimoto, Y., Koga, M., Koseki, Y., Maeda, T., Mitsui, T., Motoki, M., Nakajima, K., Ogawa, H., Ogawa, M., Owada, K., Ricol, J.S., Shimizu, I., Shirai, J., Suekane, F., Suzuki, A., Tada, K., Takeuchi, S., Tamae, K., Tsuda, Y., Watanabe, H., Busenitz, J., Classen, T., Djurcic, Z., Keefer, G., Leonard, D., Piepke, A., Yakushev, E., Berger, B.E., Chan, Y.D., Decowski, M.P., Dwyer, D.A., Freedman, S.J., Fujikawa, B.K., Goldman, J., Gray, F., Heeger, K.M., Hsu, L., Lesko, K.T., Luk, K.B., Murayama, H., O'Donnell, T., Poon, A.W.P., Steiner, H.M., Winslow, L.A., Mauger, C., McKeown, R.D., Vogel, P., Lane, C.E., Miletic, T., Guillian, G., Learned, J.G., Maricic, J., Matsuno, S., Pakvasa, S., Horton-Smith, G.A., Dazeley, S., Hatakeyama, S., Rojas, A., Svoboda, R., Dieterle, B.D., Detwiler, J., Gratta, G., Ishii, K., Tolich, N., Uchida, Y., Batygov, M., Bugg, W., Efremenko, Y., Kamyshkov, Y., Kozlov, A., Nakamura, Y., Karwowski, H.J., Markoff, D.M., Nakamura, K., Rohm, R.M., Tornow, W., Wendell, R., Chen, M.J., Wang, Y.F., Piquemal, F., 2005. Experimental investigation of geologically produced antineutrinos with KamLAND. Nature 436, 499–503. doi:10.1038/nature03980.

Arevalo Jr, R., McDonough, W.F., 2008. Tungsten geochemistry and implications for understanding the Earth's interior. Earth and Planetary Science Letters 272, 656–665.

Armstrong, L.S., Hirschmann, M.M., Stanley, B.D., Falksen, E.G., Jacobsen, S.D., 2015. Speciation and solubility of reduced C–O–H–N volatiles in mafic melt: Implications for volcanism, atmospheric evolution, and deep volatile cycles in the terrestrial planets. Geochimica et Cosmochimica Acta 171, 283–302.

Armytage, R.M.G., Georg, R.B., Savage, P.S., Williams, H.M., Halliday, A.N., 2011. Silicon isotopes in meteorites and planetary core formation. Geochimica et Cosmochimica Acta 75, 3662–3676.

Asplund, M., Grevesse, N., Sauval, A.J., Scott, P., 2009. The chemical composition of the Sun. Annual Review of Astronomy and Astrophysics 47, 481–522.

Badro, J., Aubert, J., Hirose, K., Nomura, R., Blanchard, I., Borensztajn, S., Siebert, J., 2018. Magnesium partitioning between Earth's mantle and core and its potential to drive an early exsolution geodynamo. Geophysical Research Letters 45, 13,240–13,248.

Badro, J., Brodholt, J.P., Piet, H., Siebert, J., Ryerson, F.J., 2015. Core formation and core composition from coupled geochemical and geophysical constraints. Proceedings of the National Academy of Sciences 112, 12310–12314.

Badro, J., Côté, A., Brodholt, J.P., 2014. A seismologically consistent compositional model of Earth's core. Proceedings of the National Academy of Sciences 111, 7542–7545.

Badro, J., Fiquet, G., Guyot, F., Gregoryanz, E., Occelli, F., Antonangeli, D., d'Astuto, M., 2007. Effect of light elements on the sound velocities in solid iron: Implications for the composition of Earth's core. Earth and Planetary Science Letters 254, 233–238.

Badro, J., Siebert, J., Nimmo, F., 2016. An early geodynamo driven by exsolution of mantle components from Earth's core. Nature 536, 326–328.

Ballmer, M.D., Houser, C., Hernlund, J.W., Wentzcovitch, R.M., Hirose, K., 2017. Persistence of strong silica-enriched domains in the Earth's lower mantle. Nature Geoscience 10, 236–240.

Becker, H., Horan, M., Walker, R., Gao, S., Lorand, J.P., Rudnick, R., 2006. Highly siderophile element composition of the Earth's primitive upper mantle: constraints from new data on peridotite massifs and xenoliths. Geochimica et Cosmochimica Acta 70, 4528–4550.

Belonoshko, A.B., Ahuja, R., Johansson, B., 2003. Stability of the body-centred-cubic phase of iron in the Earth's inner core. Nature 424, 1032–1034.

Belonoshko, A.B., Fu, J., Bryk, T., Simak, S.I., Mattesini, M., 2019. Low viscosity of the Earth's inner core. Nature communications 10, 2483.

Belonoshko, A.B., Simak, S.I., Olovsson, W., Vekilova, O.Y., 2022. Elastic properties of body-centered cubic iron in Earth's inner core. Physical Review B 105, L180102.

Birch, F., 1947. Finite elastic strain of cubic crystals. Physical Review 71, 809–824.

Birch, F., 1952. Elasticity and constitution of the Earth's interior. Journal of Geophysical Research 57, 227–286. doi:10.1029/JZ057i002p00227.

Birch, F., 1961. The velocity of compressional waves in rocks to 10 kilobars, part 2. Journal of Geophysical Research 66, 2199–2224.

Blanchard, I., Rubie, D.C., Jennings, E.S., Franchi, I.A., Zhao, X., Petitgirard, S., Miyajima, N., Jacobson, S.A., Morbidelli, A., 2022. The metal–silicate partitioning of carbon during Earth's accretion and its distribution in the early solar system. Earth and Planetary Science Letters 580, 117374.

Blanchard, I., Siebert, J., Borensztajn, S., Badro, J., 2017. The solubility of heat-producing elements in Earth's core. Geochemical Perspectives Letters 5, 1–5.

van Boekel, R., Min, M., Leinert, C., Waters, L., Richichi, A., Chesneau, O., Dominik, C., Jaffe, W., Dutrey, A., Graser, U., et al., 2004. The building blocks of planets within the 'terrestrial'region of protoplanetary disks. Nature 432, 479–482.

Bommannavar, A., Chow, P., Ferry, R., Hrubiak, R., Humble, F., Kenney-Benson, C., Lv, M., Meng, Y., Park, C., Popov, D., Rod, E., Somayazulu, M., Shen, G., Smith, D., Smith, J., Xiao, Y., Velisavljevic, N., 2022. Overview of HPCAT and capabilities for studying minerals and various other materials at high-pressure conditions. Physics and Chemistry of Minerals 49, 36.

Bono, R.K., Tarduno, J.A., Nimmo, F., Cottrell, R.D., 2019. Young inner core inferred from Ediacaran ultra-low geomagnetic field intensity. Nature Geoscience 12, 143–147.

Borg, L.E., Gaffney, A.M., Shearer, C.K., 2015. A review of lunar chronology revealing a preponderance of 4.34–4.37 Ga ages. Meteoritics and Planetary Science 50, 715–732.

Bouchet, J., Bottin, F., Antonangeli, D., Morard, G., 2022. Sound velocities and thermodynamical properties of hcp iron at high pressure and temperature. Journal of Physics: Condensed Matter 34, 344002.

Bouchet, J., Mazevet, S., Morard, G., Guyot, F., Musella, R., 2013. *Ab initio* equation of state of iron up to 1500 GPa. Physical Review B 87, 094102.

Bouhifd, M.A., Jephcoat, A.P., 2011. Convergence of Ni and Co metal–silicate partition coefficients in the deep magma-ocean and coupled silicon–oxygen solubility in iron melts at high pressures. Earth and Planetary Science Letters 307, 341–348.

Bouhifd, M.A., Jephcoat, A.P., Heber, V.S., Kelley, S.P., 2013. Helium in Earth's early core. Nature Geoscience 6, 982–986.

Bouhifd, M.A., Jephcoat, A.P., Porcelli, D., Kelley, S.P., Marty, B., 2020. Potential of Earth's core as a reservoir for noble gases: Case for helium and neon. Geochemical Perspective Letters 15, 15–18.

Boujibar, A., Andrault, D., Bouhifd, M.A., Bolfan-Casanova, N., Devidal, J.L., Trcera, N., 2014. Metal–silicate partitioning of sulphur, new experimental and thermodynamic constraints on planetary accretion. Earth and Planetary Science Letters 391, 42–54.

Bouwman, J., Lawson, W., Juhász, A., Dominik, C., Feigelson, E., Henning, T., Tielens, A., Waters, L., 2010. The protoplanetary disk around the M4 star RECX 5: witnessing the influence of planet formation? The Astrophysical Journal Letters 723, L243.

Brandon, A.D., Snow, J.E., Walker, R.J., Morgan, J.W., Mock, T.D., 2000. ^{190}Pt–^{186}Os and ^{187}Re–^{187}Os systematics of abyssal peridotites. Earth and Planetary Science Letters 177, 319–335.

Brandon, A.D., Walker, R.J., Morgan, J.W., Norman, M.D., Prichard, H.M., 1998. Coupled ^{186}Os and ^{187}Os evidence for core-mantle interaction. Science 280, 1570–1573.

Brennan, M.C., Fischer, R.A., Couper, S., Miyagi, L., Antonangeli, D., Morard, G., 2021. High-pressure deformation of iron–nickel–silicon alloys and implications for Earth's inner core. Journal of Geophysical Research: Solid Earth 126, e2020JB021077.

Brenner, A.R., Fu, R.R., Kylander-Clark, A.R.C., Hudak, G.J., Foley, B.J., 2022. Plate motion and a dipolar geomagnetic field at 3.25 Ga. Proceedings of the National Academy of Sciences 119, e2210258119.

Cabrera, A., Chen, M., Mantovani, F., Serafini, A., Strati, V., Apilluelo, J., Asquith, L., Beney, J., Bezerra, T., Bongrand, M., et al., 2023. Probing Earth's Missing Potassium using the Unique Antimatter Signature of Geoneutrinos. arXiv e-prints , arXiv–2308.

Canup, R.M., 2004. Simulations of a late lunar-forming impact. Icarus 168, 433–456.

Cao, A., Romanowicz, B., 2004. Constraints on density and shear velocity contrasts at the inner core boundary. Geophysical Journal International 157, 1146–1151.

Carter, P.J., Stewart, S.T., 2022. Did Earth eat its leftovers? Impact ejecta as a component of the late veneer. The Planetary Science Journal 3, 83.

Cavazzoni, C., Chiarotti, G., Scandolo, S., Tosatti, E., Bernasconi, M., Parrinello, M., 1999. Superionic and metallic states of water and ammonia at giant planet conditions. Science 283, 44–46.

Chambat, F., Ricard, Y., Valette, B., 2010. Flattening of the Earth: further from hydrostaticity than previously estimated. Geophysical Journal International 183, 727–732.

Chambers, J.E., 2013. Late-stage planetary accretion including hit-and-run collisions and fragmentation. Icarus 224, 43–56.

Chen, B., Lai, X., Li, J., Liu, J., Zhao, J., Bi, W., Alp, E.E., Hu, M.Y., Xiao, Y., 2018. Experimental constraints on the sound velocities of cementite Fe_3C to core pressures. Earth and Planetary Science Letters 494, 164–171.

Chi, H., Dasgupta, R., Duncan, M.S., Shimizu, N., 2014. Partitioning of carbon between Fe-rich alloy melt and silicate melt in a magma ocean—implications for the abundance and origin of volatiles in Earth, Mars, and the Moon. Geochimica et Cosmochimica Acta 139, 447–471.

Chidester, B.A., Lock, S., Swadba, K.E., Rahman, Z., Righter, K., Campbell, A.J., 2022. The lithophile element budget of Earth's core. Geochemistry, Geophysics, Geosystems 23, e2021GC009986.

Clesi, V., Bouhifd, M.A., Bolfan-Casanova, N., Manthilake, G., Schiavi, F., Raepsaet, C., Bureau, H., Khodja, H., Andrault, D., 2018. Low hydrogen contents in the cores of terrestrial planets. Science Advances 4, e1701876.

Corgne, A., Keshav, S., Fei, Y., McDonough, W.F., 2007. How much potassium is in the Earth's core? New insights from partitioning experiments. Earth and Planetary Science Letters 256, 567–576. doi:10.1016/j.epsl.2007.02.012.

Corgne, A., Keshav, S., Wood, B.J., McDonough, W.F., Fei, Y., 2008. Metal–silicate partitioning and constraints on core composition and oxygen fugacity during Earth accretion. Geochimica et Cosmochimica Acta 72, 574–589.

Corgne, A., Siebert, J., Badro, J., 2009. Oxygen as a light element: A solution to single-stage core formation. Earth and Planetary Science Letters 288, 108–114.

Dahl, T.W., Stevenson, D.J., 2010. Turbulent mixing of metal and silicate during planet accretion – And interpretation of the Hf–W chronometer. Earth and Planetary Science Letters 295, 177–186.

Dalou, C., Hirschmann, M.M., von der Handt, A., Mosenfelder, J., Armstrong, L.S., 2017. Nitrogen and carbon fractionation during core–mantle differentiation at shallow depth. Earth and Planetary Science Letters 458, 141–151.

Dasgupta, R., Chi, H., Shimizu, N., Buono, A.S., Walker, D., 2013. Carbon solution and partitioning between metallic and silicate melts in a shallow magma ocean: Implications for the origin and distribution of terrestrial carbon. Geochimica et Cosmochimica Acta 102, 191–212.

Dauphas, N., 2017. The isotopic nature of the Earth's accreting material through time. Nature 541, 521–524.

Dauphas, N., Hopp, T., Nesvorný, D., 2024. Bayesian inference on the isotopic building blocks of Mars and Earth. Icarus 408, 115805.

Dauphas, N., Pourmand, A., 2011. Hf–W–Th evidence for rapid growth of Mars and its status as a planetary embryo. Nature 473, 489–492. doi:10.1038/nature10077.

Davies, C.J., Stegman, D.R., Dumberry, M., 2014. The strength of gravitational core-mantle coupling. Geophysical Research Letters 41, 3786–3792.

de Koker, N., Steinle-Neumann, G., Vlček, V., 2012. Electrical resistivity and thermal conductivity of liquid Fe alloys at high P and T, and heat flux in Earth's core. Proceedings of the National Academy of Sciences 109, 4070–4073.

Deguen, R., 2012. Structure and dynamics of Earth's inner core. Earth and Planetary Science Letters 333–334, 211–225.

Deguen, R., Landeau, M., Olson, P., 2014. Turbulent metal–silicate mixing, fragmentation, and equilibration in magma oceans. Earth and Planetary Science Letters 391, 274–287.

Deguen, R., Olson, P., Cardin, P., 2011. Experiments on turbulent metal-silicate mixing in a magma ocean. Earth and Planetary Science Letters 310, 303–313.

Deuss, A., 2014. Heterogeneity and anisotropy of Earth's inner core. Annual Review of Earth and Planetary Sciences 42, 103–126.

Dewaele, A., Loubeyre, P., Occelli, F., Mezouar, M., Dorogokupets, P.I., Torrent, M., 2006. Quasihydrostatic equation of state of iron above 2 Mbar. Physical Review Letters 97, 215504.

Donini, A., Palomares-Ruiz, S., Salvado, J., 2019. Neutrino tomography of Earth. Nature Physics 15, 37–40.

Dorogokupets, P., Dymshits, A., Litasov, K., Sokolova, T., 2017. Thermodynamics and Equations of State of Iron to 350 GPa and 6000 K. Scientific reports 7, 1–11.

Dorogokupets, P.I., Oganov, A.R., 2007. Ruby, metals, and MgO as alternative pressure scales: A semiempirical description of shock-wave, ultrasonic, x-ray, and thermochemical data at high temperatures and pressures. Physical Review B 75, 024115.

Dreibus, G., Palme, H., 1996. Cosmochemical constraints on the sulfur content in the Earth's core. Geochimica et Cosmochimica Acta 60, 1125–1130. doi:10.1016/0016-7037(96)00028-2.

Driscoll, P., Davies, C., 2023. The "New Core Paradox:" Challenges and Potential Solutions. Journal of Geophysical Research: Solid Earth , e2022JB025355.

Du, Z., Boujibar, A., Driscoll, P., Fei, Y., 2019. Experimental constraints on an MgO exsolution-driven geodynamo. Geophysical Research Letters 46, 7379–7385.

Dubrovinsky, L., Dubrovinskaia, N., Narygina, O., Kantor, I., Kuznetzov, A., Prakapenka, V., Vitos, L., Johansson, B., Mikhaylushkin, A., Simak, S., et al., 2007. Body-centered cubic iron-nickel alloy in Earth's core. Science 316, 1880–1883.

Dumberry, M., Bloxham, J., 2002. Inner core tilt and polar motion. Geophysical Journal International 151, 377–392.

Dziewonski, A.M., Anderson, D.L., 1981. Preliminary Reference Earth Model. Physics of the Earth and Planetary Interiors 25, 297–356. doi:10.1016/0031-9201(81)90046-7.

Edmund, E., Antonangeli, D., Decremps, F., Miozzi, F., Morard, G., Boulard, E., Clark, A.N., Ayrinhac, S., Gauthier, M., Morand, M., Mezouar, M., 2019. Velocity-density systematics of Fe-5wt%Si: Constraints on Si content in the Earth's inner core. Journal of Geophysical Research: Solid Earth 124, 3436–3447.

Edmund, E., Morard, G., Baron, M.A., Rivoldini, A., Yokoo, S., Boccato, S., Hirose, K., Pakhomova, A., Antonangeli, D., 2022. The Fe-FeSi phase diagram at Mercury's core conditions. Nature Communications 13, 387.

Elkins-Tanton, L.T., 2008. Linked magma ocean solidification and atmospheric growth for Earth and Mars. Earth and Planetary Science Letters 271, 181–191.

Elkins-Tanton, L.T., 2012. Magma oceans in the inner Solar System. Annual Review of Earth and Planetary Sciences 40, 113–139.

Farcy, B., Arevalo Jr, R., McDonough, W., 2020. K/U of the MORB Source and Silicate Earth. Journal of Geophysical Research: Solid Earth 125, e2020JB020245.

Faure, P., Bouhifd, M.A., Boyet, M., Manthilake, G., Clesi, V., Devidal, J.L., 2020. Uranium and thorium partitioning in the bulk silicate Earth and the oxygen content of Earth's core. Geochimica et Cosmochimica Acta 275, 83–98.

Fei, H., Ballmer, M.D., Faul, U., Walte, N., Cao, W., Katsura, T., 2023. Variation in bridgmanite grain size accounts for the mid-mantle viscosity jump. Nature , 1–6.

Fei, Y., Murphy, C., Shibazaki, Y., Shahar, A., Huang, H., 2016. Thermal equation of state of hcp-iron: Constraint on the density deficit of Earth's solid inner core. Geophysical Research Letters 43, 6837–6843.

Fiquet, G., Auzende, A.L., Siebert, J., Corgne, A., Bureau, H., Ozawa, H., Garbarino, G., 2010. Melting of peridotite to 140 gigapascals. Science 329, 1516–1518.

Fiquet, G., Badro, J., Gregoryanz, E., Fei, Y., Occelli, F., 2009. Sound velocity in iron carbide (Fe_3C) at high pressure: Implications for the carbon content of the Earth's inner core. Physics of the Earth and Planetary Interiors 172, 125–129.

Fischer, R.A., 2016. Melting of Fe alloys and the thermal structure of the core, in: Terasaki, H., Fischer, R.A. (Eds.), Deep Earth: Physics and Chemistry of the Lower Mantle and Core. John Wiley & Sons, Inc, Washington DC. volume 217 of *Geophysical Monograph Series* of *Geophysical Monograph Series*. chapter 1, pp. 1–12. doi:doi.org/10.1002/9781118992487.ch1.

Fischer, R.A., Campbell, A.J., 2015. The axial ratio of hcp Fe and Fe–Ni–Si alloys to the conditions of Earth's inner core. American Mineralogist 100, 2718–2724.

Fischer, R.A., Campbell, A.J., Caracas, R., Reaman, D.M., Dera, P., Prakapenka, V.B., 2012. Equation of state and phase diagram of Fe–16Si alloy as a candidate component of Earth's core. Earth and Planetary Science Letters 357–358, 268–276.

Fischer, R.A., Campbell, A.J., Caracas, R., Reaman, D.M., Heinz, D.L., Dera, P., Prakapenka, V.B., 2014. Equations of state in the Fe-FeSi system at high pressures and temperatures. Journal of Geophysical Research: Solid Earth 119, 2810–2827.

Fischer, R.A., Campbell, A.J., Ciesla, F.J., 2017. Sensitivities of Earth's core and mantle compositions to accretion and differentiation processes. Earth and Planetary Science Letters 458, 252–262.

Fischer, R.A., Campbell, A.J., Reaman, D.M., Miller, N.A., Heinz, D.L., Dera, P., Prakapenka, V.B., 2023. Phase relations in the Fe–FeSi system at high pressures and temperatures. Earth and Planetary Science Letters 373, 54–64.

Fischer, R.A., Campbell, A.J., Shofner, G.A., Lord, O.T., Dera, P., Prakapenka, V.B., 2011. Equation of state and phase diagram of FeO. Earth and Planetary Science Letters 304, 496–502.

Fischer, R.A., Ciesla, F.J., 2014. Dynamics of the terrestrial planets from a large number of N-body simulations. Earth and Planetary Science Letters 392, 28–38.

Fischer, R.A., Cottrell, E., Hauri, E., Lee, K.K.M., Le Voyer, M., 2020. The carbon content of Earth and its core. Proceedings of the National Academy of Sciences 117, 8743–8749.

Fischer, R.A., Nakajima, Y., Campbell, A.J., Frost, D.J., Harries, D., Langenhorst, F., Miyajima, N., Pollok, K., Rubie, D.C., 2015. High pressure metal–silicate partitioning of Ni, Co, V, Cr, Si, and O. Geochimica et Cosmochimica Acta 167, 177–194.

Fischer, R.A., Nimmo, F., 2018. Effects of core formation on the Hf–W isotopic composition of the Earth and dating of the Moon-forming impact. Earth and Planetary Science Letters 499, 257–265.

Fischer, R.A., Nimmo, F., O'Brien, D.P., 2018. Radial mixing and Ru–Mo isotope systematics under different accretion scenarios. Earth and Planetary Science Letters 482, 105–114.

Fischer-Gödde, M., Becker, H., Wombacher, F., 2010. Rhodium, gold and other highly siderophile element abundances in chondritic meteorites. Geochimica et Cosmochimica Acta 74, 356–379.

Fischer-Gödde, M., Becker, H., Wombacher, F., 2011. Rhodium, gold and other highly siderophile elements in orogenic peridotites and peridotite xenoliths. Chemical Geology 280, 365–383.

Fitoussi, C., Bourdon, B., 2012. Silicon isotope evidence against an enstatite chondrite Earth. Science 335, 1477–1480.

Fitoussi, C., Bourdon, B., Kleine, T., Oberli, F., Reynolds, B.C., 2009. Si isotope systematics of meteorites and terrestrial peridotites: implications for Mg/Si fractionation in the solar nebula and for Si in the Earth's core. Earth and Planetary Science Letters 287, 77–85.

Fleck, J.R., Rains, C.L., Weeraratne, D.S., Nguyen, C.T., Brand, D.M., Klein, S.M., McGehee, J.M., Rincon, J.M., Martinez, C., Olson, P.L., 2018. Iron diapirs entrain silicates to the core and initiate thermochemical plumes. Nature Communications 9, 71.

French, S.W., Romanowicz, B., 2015. Broad plumes rooted at the base of the Earth's mantle beneath major hotspots. Nature 525, 95–99.

Frost, D.A., Lasbleis, M., Chandler, B., Romanowicz, B., 2021. Dynamic history of the inner core constrained by seismic anisotropy. Nature Geoscience 14, 531–535.

Fukai, Y., Suzuki, T., 1986. Iron-water reaction under high pressure and its implication in the evolution of the Earth. Journal of Geophysical Research 91, 9222–9230.

Fukao, Y., Obayashi, M., 2013. Subducted slabs stagnant above, penetrating through, and trapped below the 660 km discontinuity. Journal of Geophysical Research: Solid Earth 118, 5920–5938.

Gaillard, F., Malavergne, V., Bouhifd, M.A., Rogerie, G., 2022. A speciation model linking the fate of carbon and hydrogen during core – magma ocean equilibration. Earth and Planetary Science Letters 577, 117266.

Garnero, E.J., McNamara, A.K., Shim, S.H., 2016. Continent-sized anomalous zones with low seismic velocity at the base of Earth's mantle. Nature Geoscience 9, 481–489.

Georg, R.B., Halliday, A.N., Schauble, E.A., Reynolds, B.C., 2007. Silicon in the Earth's core. Nature 447, 1102–1106.

Gessmann, C.K., Wood, B.J., 2002. Potassium in the Earth's core? Earth and Planetary Science Letters 200, 63–78.

Gleason, A.E., Mao, W.L., Zhao, J.Y., 2013. Sound velocities for hexagonally close-packed iron compressed hydrostatically to 136 GPa from phonon density of states. Geophysical Research Letters 40, 1–5.

Golabek, G.J., Gerya, T.V., Kaus, B.J.P., Ziethe, R., Tackley, P.J., 2009. Rheological controls on the terrestrial core formation mechanism. Geochemistry, Geophysics, Geosystems 10, 11.

Golabek, G.J., Schmeling, H., Tackley, P.J., 2008. Earth's core formation aided by flow channelling instabilities induced by iron diapirs. Earth and Planetary Science Letters 271, 24–33.

Gomi, H., Ohta, K., Hirose, K., Labrosse, S., Caracas, R., Verstraete, M.J., Hernlund, J.W., 2013. The high conductivity of iron and thermal evolution of the Earth's core. Physics of the Earth and Planetary Interiors 224, 88–103.

Grewal, D.S., Dasgupta, R., Holmes, A.K., Costin, G., Li, Y., Tsuno, K., 2019a. The fate of nitrogen during core-mantle separation on Earth. Geochimica et Cosmochimica Acta 251, 87–115.

Grewal, D.S., Dasgupta, R., Sun, C., Tsuno, K., Costin, G., 2019b. Delivery of carbon, nitrogen, and sulfur to the silicate Earth by a giant impact. Science Advances 5, eaau3669.

Gu, J.T., Fischer, R.A., Brennan, M.C., Clement, M.S., Jacobson, S.A., Kaib, N.A., O'Brien, D.P., Raymond, S.N., 2023. Comparisons of the core and mantle compositions of Earth analogs from different terrestrial planet formation scenarios. Icarus 394, 115425.

Gu, J.T., Peng, B., Ji, X., Zhang, J., Yang, H., Hoyos, S., Hirschmann, M.M., Kite, E.S., Fischer, R.A., 2024. Composition of Earth's initial atmosphere and fate of accreted volatiles set by core formation and magma ocean redox evolution. Earth and Planetary Science Letters 629, 118618.

Gubbins, D., Masters, T.G., Jacobs, J.A., 1979. Thermal evolution of the Earth's core. Geophysical Journal International 59, 57–99.

Halliday, A., Rehkämper, M., Lee, D.C., Yi, W., 1996. Early evolution of the Earth and Moon: new constraints from Hf–W isotope geochemistry. Earth and Planetary Science Letters 142, 75–89.

Halliday, A.N., 2000. Terrestrial accretion rates and the origin of the Moon. Earth and Planetary Science Letters 176, 17–30.

Hamano, K., Abe, Y., Genda, H., 2013. Emergence of two types of terrestrial planets on solidification of magma ocean. Nature 497, 607–610.

Hasegawa, M., Hirose, K., Oka, K., Ohishi, Y., 2021. Liquidus phase relations and solid-liquid partitioning in the Fe-Si-C system under core pressures. Geophysical Research Letters 48, e2021GL092681.

He, Y., Sun, S., Kim, D.Y., Jang, B.G., Li, H., Mao, H.k., 2022. Superionic iron alloys and their seismic velocities in Earth's inner core. Nature 602, 258–262.

Hellmann, J.L., Kruijer, T.S., Van Orman, J.A., Metzler, K., Kleine, T., 2019. Hf-W chronology of ordinary chondrites. Geochimica et Cosmochimica Acta 258, 290–309.

Herzberg, C., Asimow, P.D., Ionov, D.A., Vidito, C., Jackson, M.G., Geist, D., 2013. Nickel and helium evidence for melt above the core–mantle boundary. Nature 493, 393–397.

Hilton, C.D., Ash, R.D., Walker, R.J., 2022. Chemical characteristics of iron meteorite parent bodies. Geochimica et Cosmochimica Acta 318, 112–125.

Hin, R.C., Fitoussi, C., Schmidt, M.W., Bourdon, B., 2014. Experimental determination of the Si isotope fractionation factor between liquid metal and liquid silicate. Earth and Planetary Science Letters 387, 55–66.

Hirose, K., Wood, B., Vočadlo, L., 2021. Light elements in the Earth's core. Nature Reviews Earth & Environment 2, 645–658.

Höink, T., Schmalzl, J., Hansen, U., 2006. Dynamics of metal–silicate separation in a terrestrial magma ocean. Geochemistry, Geophysics, Geosystems 7, 9.

Hu, X., Fei, Y., Yang, J., Cai, Y., Ye, S., Qi, M., Liu, F., Zhang, M., 2019. Phase stability and thermal equation of state of iron carbide Fe_3C to 245 GPa. Geophysical Research Letters 46, 11,018–11,024.

Huang, D., Siebert, J., Badro, J., 2021. High pressure partitioning behavior of Mo and W and late sulfur delivery during Earth's core formation. Geochimica et Cosmochimica Acta 310, 19–31.

Huang, H., Leng, C., Wang, Q., Young, G., Liu, X., Wu, Y., Xu, F., Fei, Y., 2019. Equation of state for shocked Fe-8.6 wt% Si up to 240 GPa and 4,670 K. Journal of Geophysical Research: Solid Earth 124, 8300–8312.

Huang, Q., Schmerr, N.C., King, S.D., Kim, D., Rivoldini, A., Plesa, A.C., Samuel, H., Maguire, R.R., Karakostas, F., Lekić, V., et al., 2022. Seismic detection of a deep mantle discontinuity within Mars by InSight. Proceedings of the National Academy of Sciences 119, e2204474119.

Huang, Y., Chubakov, V., Mantovani, F., Rudnick, R.L., McDonough, W.F., 2013. A reference Earth

model for the heat-producing elements and associated geoneutrino flux. Geochemistry, Geophysics, Geosystems 14, 2003–2029. doi:10.1002/ggge.20129.

Humayun, M., Qin, L., Norman, M.D., 2004. Geochemical evidence for excess iron in the mantle beneath Hawaii. Science 306, 91–94.

Ichikawa, H., Tsuchiya, T., Tange, Y., 2014. The P-V-T equation of state and thermodynamic properties of liquid iron. Journal of Geophysical Research: Solid Earth 119, 240–252.

Iizuka-Oku, R., Yagi, T., Gotou, H., Okuchi, T., Hattori, T., Sano-Furukawa, A., 2017. Hydrogenation of iron in the early stage of Earth's evolution. Nature Communications 8, 14096.

Ikuta, D., Ohtani, E., Fukui, H., Sakai, T., Ishikawa, D., Baron, A.Q., 2022. Sound velocity of hexagonal close-packed iron to the Earth's inner core pressure. Nature Communications 13, 7211.

Ikuta, D., Ohtani, E., Fukui, H., Sakamaki, T., Heid, R., Ishikawa, D., Baron, A.Q., 2023. Density deficit of Earth's core revealed by a multimegabar primary pressure scale. Science advances 9, eadh8706.

Ikuta, D., Ohtani, E., Hirao, N., 2021a. Two-phase mixture of iron–nickel–silicon alloys in the Earth's inner core. Communications Earth & Environment 2, 225.

Ikuta, D., Ohtani, E., Hirao, N., 2021b. Two-phase mixture of iron–nickel–silicon alloys in the Earth's inner core. Communications Earth & Environment 2, 225.

Ikuta, N., Sakamoto, N., Tagawa, S., Hirose, K., Tsutsumi, Y., Yokoo, S., Yurimoto, H., 2024. Pressure dependence of metal–silicate partitioning explains the mantle phosphorus abundance. Scientific Reports 14, 1194.

Ireland, T.J., Arevalo Jr, R., Walker, R.J., McDonough, W.F., 2009. Tungsten in Hawaiian picrites: A compositional model for the sources of Hawaiian lavas. Geochimica et Cosmochimica Acta 73, 4517–4530.

Irving, J.C., Lekić, V., Durán, C., Drilleau, M., Kim, D., Rivoldini, A., Khan, A., Samuel, H., Antonangeli, D., Banerdt, W.B., et al., 2023. First observations of core-transiting seismic phases on Mars. Proceedings of the National Academy of Sciences 120, e2217090120.

Irving, J.C.E., Cottaar, S., Lekić, V., 2018. Seismically determined elastic parameters for Earth's outer core. Science Advances 4, eaar2538.

Ishii, M., Dziewoński, A.M., 2002. The innermost inner core of the Earth: Evidence for a change in anisotropic behavior at the radius of about 300 km. Proceedings of the National Academy of Sciences 99, 14026–14030.

Jackson, C.R.M., Bennett, N.R., Du, Z., Cottrell, E., Fei, Y., 2018. Early episodes of high-pressure core formation preserved in plume mantle. Nature 553, 491–495.

Jackson, C.R.M., Cottrell, E., Du, Z., Bennett, N.R., Fei, Y., 2021. High pressure redistribution of nitrogen and sulfur during planetary stratification. Geochemical Perspective Letters 18, 37–42.

Jacobson, S.A., Morbidelli, A., Raymond, S.N., O'Brien, D.P., Walsh, K.J., Rubie, D.C., 2014. Highly siderophile elements in Earth's mantle as a clock for the Moon-forming impact. Nature 508, 84–87.

Jaupart, C., Labrosse, S., Lucazeau, F., Mareschal, J.C., 2015. Temperatures, heat, and energy in the mantle of the Earth, in: Schubert, G. (Ed.), Treatise on Geophysics (Second Edition). Elsevier, Oxford. volume 7, pp. 223–270. doi:10.1016/B978-0-444-53802-4.00126-3.

Javoy, M., 1995. The integral enstatite chondrite model of the Earth. Geophysical Research Letters 22, 2219–2222. doi:10.1029/95GL02015.

Javoy, M., Kaminski, E., Guyot, F., Andrault, D., Sanloup, C., Moreira, M., Labrosse, S., Jambon, A., Agrinier, P., Davaille, A., Jaupart, C., 2010. The chemical composition of the Earth: Enstatite chondrite models. Earth and Planetary Science Letters 293, 259–268. doi:10.1016/j.epsl.2010.02.033.

Jeanloz, R., Wenk, H.R., 1988. Convection and anisotropy of the inner core. Geophysical Research Letters 15, 72–75.

Jeffreys, H., Bullen, K., 1940. Seismological tables, Brit. Assoc. Adv. Sci., London .

Jennings, E.S., Jacobson, S.A., Rubie, D.C., Nakajima, Y., Vogel, A.K., Rose-Weston, L.A., Frost, D.J., 2021. Metal–silicate partitioning of W and Mo and the role of carbon in controlling their abundances in the bulk silicate earth. Geochimica et Cosmochimica Acta 293, 40–69.

Johansen, A., Ronnet, T., Bizzarro, M., Schiller, M., Lambrechts, M., Nordlund, Å., Lammer, H., 2021. A pebble accretion model for the formation of the terrestrial planets in the Solar System. Science Advances 7, eabc0444.

Kallemeyn, G.W., Rubin, A.E., Wang, D., Wasson, J.T., 1989. Ordinary chondrites: Bulk compositions, classification, lithophile-element fractionations and composition-petrographic type relationships. Geochimica et Cosmochimica Acta 53, 2747–2767.

Kallemeyn, G.W., Wasson, J.T., 1981. The compositional classification of chondrites—I. The carbonaceous chondrite groups. Geochimica et Cosmochimica Acta 45, 1217–1230.

Kallemeyn, G.W., Wasson, J.T., 1986. Compositions of enstatite (EH3, EH4, 5 and EL6) chondrites: Implications regarding their formation. Geochimica et Cosmochimica Acta 50, 2153–2164.

Kamada, S., Ohtani, E., Fukui, H., Sakai, T., Terasaki, H., Takahashi, S., Shibazaki, Y., Tsutsui, S., Baron, A.Q.R., Hirao, N., Ohishi, Y., 2014. The sound velocity measurements of Fe_3S. American Mineralogist 99, 98–101.

Kamada, S., Terasaki, H., Ohtani, E., Sakai, T., Kikegawa, T., Ohishi, Y., Hirao, N., Sata, N., Kondo, T., 2010. Phase relationships of the Fe–FeS system in conditions up to the Earth's outer core. Earth and Planetary Science Letters 294, 94–100.

Karato, S., Murthy, V.R., 1997. Core formation and chemical equilibrium in the Earth—I. Physical considerations. Physics of the Earth and Planetary Interiors 100, 61–79.

Katsura, T., 2022. A revised adiabatic temperature profile for the mantle. Journal of Geophysical Research: Solid Earth 127, e2021JB023562.

Kemper, J., Khan, A., Helffrich, G., van Driel, M., Giardini, D., 2023. Self-consistent models of Earth's mantle and core from long-period seismic and tidal constraints. Geophysical Journal International 235, 690–717.

Kendall, J.D., Melosh, H.J., 2016. Differentiated planetesimal impacts into a terrestrial magma ocean: Fate of the iron core. Earth and Planetary Science Letters 448, 24–33.

Kennett, B.L.N., Engdahl, E.R., 1991. Traveltimes for global earthquake location and phase identification. Geophysical Journal International 105, 429–465.

Kennett, B.L.N., Engdahl, E.R., Buland, R., 1995. Constraints on seismic velocities in the Earth from traveltimes. Geophysical Journal International 122, 108–124.

Khan, A., Huang, D., Durán, C., Sossi, P.A., Giardini, D., Murakami, M., 2023. Evidence for a liquid silicate layer atop the Martian core. Nature 622, 718–723.

Kim, T., O'Rourke, J.G., Lee, J., Chariton, S., Prakapenka, V., Husband, R.J., Giordano, N., Liermann, H.P., Shim, S.H., Lee, Y., 2023. A hydrogen-enriched layer in the topmost outer core sourced from deeply subducted water. Nature Geoscience 16, 1208–1214.

Kleine, T., Münker, C., Mezger, K., Palme, H., 2002. Rapid accretion and early core formation on asteroids and the terrestrial planets from Hf–W chronometry. Nature 418, 952–955.

Kleine, T., Nimmo, F., this volume. Origin of the Earth, in: Treatise on Geochemistry, 3rd edition.

Kleine, T., Walker, R.J., 2017. Tungsten isotopes in planets. Annual Review of Earth and Planetary Sciences 45, 389–417.

Koelemeijer, P., 2021. Toward Consistent Seismological Models of the Core–Mantle Boundary Landscape, in: Marquardt, H., Ballmer, M., Cottaar, S., Konter, J. (Eds.), Mantle Convection and Surface Expressions. American Geophysical Union, Washington DC. volume 263 of *Geophysical Monograph Series* of *Geophysical Monograph Series*. chapter 9, pp. 229–255. doi:10.1002/9781119528609.ch9.

Komabayashi, T., 2014. Thermodynamics of melting relations in the system Fe-FeO at high pressure: Implications for oxygen in the Earth's core. Journal of Geophysical Research: Solid Earth 119, 4164–4177.

Komabayashi, T., Fei, Y., 2010. Internally consistent thermodynamic database for iron to the Earth's core conditions. Journal of Geophysical Research 115, B03202.

Konôpková, Z., McWilliams, R.S., Gómez-Pérez, N., Goncharov, A.F., 2016. Direct measurement of thermal conductivity in solid iron at planetary core conditions. Nature 534, 99–101.

Koot, L., Dumberry, M., 2011. Viscosity of the Earth's inner core: Constraints from nutation observations. Earth and Planetary Science Letters 308, 343–349.

Koper, K.D., Dombrovskaya, M., 2005. Seismic properties of the inner core boundary from PKiKP/P amplitude ratios. Earth and Planetary Science Letters 237, 680–694.

Koper, K.D., Pyle, M.L., 2004. Observations of *PKiKP/PcP* amplitude ratios and implications for Earth structure at the boundaries of the liquid core. Journal of Geophysical Research 109, B03301.

Kraus, R.G., Hemley, R.J., Ali, S.J., Belof, J.L., Benedict, L.X., Bernier, J., Braun, D., Cohen, R., Collins, G.W., Coppari, F., et al., 2022. Measuring the melting curve of iron at super-earth core conditions. Science 375, 202–205.

Kruijer, T.S., Burkhardt, C., Budde, G., Kleine, T., 2017. Age of Jupiter inferred from the distinct genetics and formation times of meteorites. Proceedings of the National Academy of Sciences 114, 6712–6716. doi:10.1073/pnas.1704461114.

Kuwayama, Y., Morard, G., Nakajima, Y., Hirose, K., Baron, A.Q.R., Kawaguchi, S.I., Tsuchiya, T., Ishikawa, D., Hirao, N., Ohishi, Y., 2020. Equation of state of liquid iron under extreme conditions. Physical Review Letters 124, 165701.

Labidi, J., Cartigny, P., Moreira, M., 2013. Non-chondritic sulphur isotope composition of the terrestrial mantle. Nature 501, 208–211.

Labidi, J., Shahar, A., Le Losq, C., Hillgren, V.J., Mysen, B.O., Farquhar, J., 2016. Experimentally determined sulfur isotope fractionation between metal and silicate and implications for planetary differentiation. Geochimica et Cosmochimica Acta 175, 181–194.

Labrosse, S., Poirier, J.P., Le Mouël, J.L., 2001. The age of the inner core. Earth and Planetary Science Letters 190, 111–123.

Laio, A., Bernard, S., Chiarotti, G.L., Scandolo, S., Tosatti, E., 2000. Physics of iron at Earth's core conditions. Science 287, 1027–1030.

Lammer, H., Brasser, R., Johansen, A., Scherf, M., Leitzinger, M., 2021. Formation of Venus, Earth and Mars: Constrained by isotopes. Space Science Reviews 217, 7.

Landeau, M., Aubert, J., Olson, P., 2017. The signature of inner-core nucleation on the geodynamo. Earth and Planetary Science Letters 465, 193–204.

Landeau, M., Deguen, R., Phillips, D., Neufeld, J.A., Lherm, V., Dalziel, S.B., 2021. Metal-silicate mixing by large Earth-forming impacts. Earth and Planetary Science Letters 564, 116888.

Landeau, M., Fournier, A., Nataf, H.C., Cébron, D., Schaeffer, N., 2022. Sustaining Earth's magnetic dynamo. Nature Reviews: Earth & Environment 3, 255–269.

Larimer, J.W., Bartholomay, M., 1979. The role of carbon and oxygen in cosmic gases: some applications to the chemistry and mineralogy of enstatite chondrites. Geochimica et Cosmochimica Acta 43, 1455–1466.

Lay, T., Hernlund, J., Buffett, B.A., 2008. Core–mantle boundary heat flow. Nature geoscience 1, 25–32.

Li, J., Agee, C.B., 1996. Geochemistry of mantle–core differentiation at high pressure. Nature 381, 686–689.

Li, J., Fei, Y., Mao, H.K., Hirose, K., Shieh, S.R., 2001. Sulfur in the Earth's inner core. Earth and Planetary Science Letters 193, 509–514.

Li, J., Wu, Q., Li, J., Xue, T., Tan, Y., Zhou, X., Zhang, Y., Xiong, Z., Gao, Z., Sekine, T., 2020a. Shock melting curve of iron: A consensus on the temperature at the Earth's inner core boundary. Geophysical Research Letters 47, e2020GL087758.

Li, Y., Dasgupta, R., Tsuno, K., 2015. The effects of sulfur, silicon, water, and oxygen fugacity on carbon solubility and partitioning in Fe-rich alloy and silicate melt systems at 3 GPa and 1600°C: Implications for core–mantle differentiation and degassing of magma oceans and reduced planetary mantles. Earth and Planetary Science Letters 415, 54–66.

Li, Y., Dasgupta, R., Tsuno, K., Monteleone, B., Shimizu, N., 2016. Carbon and sulfur budget of the silicate Earth explained by accretion of differentiated planetary embryos. Nature Geoscience 9, 781–785.

Li, Y., Voĉadlo, L., Alfè, D., Brodholt, J., 2018. Mg partitioning between solid and liquid iron under the Earth's core conditions. Physics of the Earth and Planetary Interiors 274, 218–221.

Li, Y., Voĉadlo, L., Alfè, D., Brodholt, J., 2019. Carbon partitioning between the Earth's inner and outer core. Journal of Geophysical Research: Solid Earth 124, 12,812–12,824.

Li, Y., Voĉadlo, L., Sun, T., Brodholt, J.P., 2020b. The Earth's core as a reservoir of water. Nature Geoscience 13, 453–458.

Li, Z., Scandolo, S., 2022. Elasticity and viscosity of hcp iron at Earth's inner core conditions from machine learning-based large-scale atomistic simulations. Geophysical Research Letters 49, e2022GL101161.

Libourel, G., Marty, B., Humbert, F., 2003. Nitrogen solubility in basaltic melt. Part I. Effect of oxygen fugacity. Geochimica et Cosmochimica Acta 67, 4123–4135.

Lin, J.F., Fei, Y., Sturhahn, W., Zhao, J., Mao, H.K., Hemley, R.J., 2004. Magnetic transition and sound velocities of Fe_3S at high pressure: implications for Earth and planetary cores. Earth and Planetary Science Letters 226, 33–40.

Lin, J.F., Sturhahn, W., Zhao, J., Shen, G., Mao, H.K., Hemley, R.J., 2005. Sound velocities of hot dense iron: Birch's law revisited. Science 308, 1892–1894.

Lin, J.R., Gerya, T.V., Tackley, P.J., Yuen, D.A., Golabek, G.J., 2009. Numerical modeling of protocore destabilization during planetary accretion: Methodology and results. Icarus 204, 732–748.

Liu, J., Dauphas, N., Roskosz, M., Hu, M.Y., Yang, H., Bi, W., Zhao, J., Alp, E.E., Hu, J.Y., Lin, J.F., 2017. Iron isotopic fractionation between silicate mantle and metallic core at high pressure. Nature Communications 8, 14377.

Liu, J., Lin, J.F., Alatas, A., Hu, M.Y., Zhao, J., Dubrovinsky, L., 2016. Seismic parameters of hcp-Fe alloyed with Ni and Si in the Earth's inner core. Journal of Geophysical Research: Solid Earth 121, 610–623.

Lodders, K., 2003. Solar system abundances and condensation temperatures of the elements. The Astrophysical Journal 591, 1220–1247. doi:10.1086/375492.

Lodders, K., 2020. Solar elemental abundances. Oxford Research Encyclopedia of Planetary Science URL: https://doi.org/10.1093/acrefore/9780190647926.013.145, doi:10.1093/acrefore/9780190647926.013.145.

Lucazeau, F., 2019. Analysis and mapping of an updated terrestrial heat flow data set. Geochemistry, Geophysics, Geosystems 20, 4001–4024.

Luo, F., Cheng, Y., Chen, X.R., Cai, L.C., Jing, F.Q., 2011. The melting curves and entropy of iron under high pressure. Journal of Chemical & Engineering Data 56, 2063–2070.

Maas, C., Manske, L., Wünnemann, K., Hansen, U., 2021. On the fate of impact-delivered metal in a terrestrial magma ocean. Earth and Planetary Science Letters 554, 116680.

Machida, A., Saitoh, H., Sugimoto, H., Hattori, T., Sano-Furukawa, A., Endo, N., Katayama, Y., Iizuka, R., Sato, T., Matsuo, M., Orimo, S.I., Aoki, K., 2014. Site occupancy of interstitial deuterium atoms in face-centred cubic iron. Nature Communications 5, 5063.

Maderer, L., Kaminski, E., Coelho, J.A., Bourret, S., Van Elewyck, V., 2023. Unveiling the outer core composition with neutrino oscillation tomography. Frontiers in Earth Science 11, 1008396.

Magg, E., Bergemann, M., Serenelli, A., Bautista, M., Plez, B., Heiter, U., Gerber, J.M., Ludwig, H.G., Basu, S., Ferguson, J.W., et al., 2022. Observational constraints on the origin of the elements-IV. Standard composition of the Sun. Astronomy & Astrophysics 661, A140.

Mahan, B., Siebert, J., Blanchard, I., Badro, J., Kubik, E., Sossi, P., Moynier, F., 2018a. Investigating Earth's formation history through copper and sulfur metal-silicate partitioning during core-mantle differentiation. Journal of Geophysical Research: Solid Earth 123, 8349–8363.

Mahan, B., Siebert, J., Blanchard, I., Borensztajn, S., Badro, J., Moynier, F., 2018b. Constraining compositional proxies for Earth's accretion and core formation through high pressure and high temperature Zn and S metal-silicate partitioning. Geochimica et Cosmochimica Acta 235, 21–40.

Mahan, B., Siebert, J., Pringle, E.A., Moynier, F., 2017. Elemental partitioning and isotopic fractionation of Zn between metal and silicate and geochemical estimation of the S content of the Earth's core. Geochimica et Cosmochimica Acta 196, 252–270.

Malavergne, V., Bureau, H., Raepsaet, C., Gaillard, F., Poncet, M., Surblé, S., Sifré, D., Shcheka, S., Fourdrin, C., Deldicque, D., Khodja, H., 2019. Experimental constraints on the fate of H and C during planetary core-mantle differentiation. Implications for the Earth. Icarus 321, 473–485.

Malavergne, V., Tarrida, M., Combes, R., Bureau, H., Jones, J., Schwandt, C., 2007. New high-pressure and high-temperature metal/silicate partitioning of U and Pb: Implications for the cores of the Earth and Mars. Geochimica et Cosmochimica Acta 71, 2637–2655.

Mann, U., Frost, D.J., Rubie, D.C., Becker, H., Audétat, A., 2012. Partitioning of Ru, Rh, Pd, Re, Ir and Pt between liquid metal and silicate at high pressures and high temperatures - Implications for the origin of highly siderophile element concentrations in the Earth's mantle. Geochimica et Cosmochimica Acta 84, 593–613.

Marquardt, H., Thomson, A.R., 2020. Experimental elasticity of Earth's deep mantle. Nature Reviews: Earth & Environment 1, 455–469.

Martorell, B., Brodholt, J., Wood, I.G., Vočadlo, L., 2013a. The effect of nickel on the properties of iron at the conditions of Earth's inner core: *Ab initio* calculations of seismic wave velocities of Fe–Ni alloys. Earth and Planetary Science Letters 365, 143–151.

Martorell, B., Vočadlo, L., Brodholt, J., Wood, I.G., 2013b. Strong premelting effect in the elastic properties of hcp-Fe under inner-core conditions. Science 342, 466–468.

Marty, B., 2012. The origins and concentrations of water, carbon, nitrogen and noble gases on Earth. Earth and Planetary Science Letters 313–314, 56–66.

Mashino, I., Miozzi, F., Hirose, K., Morard, G., Sinmyo, R., 2019. Melting experiments on the Fe–C binary system up to 255 GPa: Constraints on the carbon content in the Earth's core. Earth and Planetary Science Letters 515, 135–144.

Masters, G., Gubbins, D., 2003. On the resolution of density within the Earth. Physics of the Earth and Planetary Interiors 140, 159–167. doi:10.1016/j.pepi.2003.07.008.

Masters, T., Shearer, P., 1995. Seismic models of the Earth: Elastic and anelastic. Global Earth Physics: a handbook of physical constants 1, 88–103.

Matsuda, J., Sudo, M., Ozima, M., Ito, K., Ohtaka, O., Ito, E., 1993. Noble gas partitioning between metal and silicate under high pressures. Science 259, 788–790.

McCoy, T.J., Walker, R., Goldstein, J., Yang, J., McDonough, W., Rumble, D., Chabot, N., Ash, R., Corrigan, C.M., Michael, J., et al., 2011. Group IVA irons: New constraints on the crystallization and cooling history of an asteroidal core with a complex history. Geochimica et Cosmochimica Acta 75, 6821–6843.

McDonough, W.F., 2005. Ghosts from within. Nature 436, 467–468.

McDonough, W.F., 2014. Compositional model for the Earth's core, in: Carlson, R.W. (Ed.), The Mantle and Core. Elsevier, Oxford. volume 3 of *Treatise on Geochemistry (Second Edition)*. chapter 16, pp. 559–577. doi:10.1016/B978-0-08-095975-7.00215-1. editors-in-chief H. D. Holland and K. K. Turekian.

McDonough, W.F., 2016. The composition of the lower mantle and core, in: Terasaki, H., Fischer, R.A. (Eds.), Deep Earth: Physics and Chemistry of the Lower Mantle and Core. John Wiley & Sons, Inc, Washington DC. volume 217 of *Geophysical Monograph Series* of *Geophysical Monograph Series*. chapter 12, pp. 143–159. doi:10.1002/9781118992487.ch12.

McDonough, W.F., Sun, S.s., 1995. The composition of the Earth. Chemical Geology 120, 223–253. doi:10.1016/0009-2541(94)00140-4.

McDonough, W.F., Šrámek, O., Wipperfurth, S.A., 2020. Radiogenic power and geoneutrino luminosity of the Earth and other terrestrial bodies through time. Geochemistry, Geophysics, Geosystems 21, e2019GC008865. doi:10.1029/2019GC008865.

McDonough, W.F., Watanabe, H., 2023. Neutrino geoscience: review, survey, future prospects, in: Nakagawa, T., Tsuchiya, T., Satish-Kumar, M., George Helffrich, G. (Eds.), Core-Mantle Co-Evolution: An Interdisciplinary Approach. John Wiley & Sons, Inc, Washington DC. volume 276 of *Geophysical Monograph Series* of *Geophysical Monograph Series*. chapter 1, pp. 1–16. doi:10.1002/9781119526919.

McDonough, W.F., Yoshizaki, T., 2021. Terrestrial planet compositions controlled by accretion disk magnetic field. Progress in Earth and Planetary Science 8, 39. doi:10.1186/s40645-021-00429-4.

Miyagi, L., Kunz, M., Knight, J., Nasiatka, J., Voltolini, M., Wenk, H.R., 2008. In situ phase transformation and deformation of iron at high pressure and temperature. Journal of Applied Physics 104, 103510.

Montagner, J.P., Kennett, B., 1996. How to reconcile body-wave and normal-mode reference Earth models. Geophysical Journal International 125, 229–248.

Morard, G., Antonangeli, D., Bouchet, J., Rivoldini, A., Boccato, S., Miozzi, F., Boulard, E., Bureau, H., Mezouar, M., Prescher, C., Chariton, S., Greenberg, E., 2022. Structural and electronic transitions in liquid FeO under high pressure. Journal of Geophysical Research: Solid Earth 127, e2022JB025117.

Morard, G., Nakajima, Y., Andrault, D., Antonangeli, D., Auzende, A.L., Boulard, E., Cervera, S., Clark, A.N., Lord, O.T., Siebert, J., Svitlyk, V., Garbarino, G., Mezouar, M., 2017. Structure and density of Fe-C liquid alloys under high pressure. Journal of Geophysical Research: Solid Earth 122, 7813–7823.

Morelli, A., Dziewonski, A.M., 1993. Body wave traveltimes and a spherically symmetric P- and S-wave velocity model. Geophysical Journal International 112, 178–194.

Morelli, A., Dziewonski, A.M., Woodhouse, J.H., 1986. Anisotropy of the inner core inferred from *PKIKP* travel times. Geophysical Research Letters 13, 1545–1548.

Morgan, J.W., 1986. Ultramafic xenoliths: clues to Earth's late accretionary history. Journal of Geophysical Research: Solid Earth 91, 12375–12387.

Mori, Y., Ozawa, H., Hirose, K., Sinmyo, R., Tateno, S., Morard, G., Oshishi, Y., 2017. Melting experiments on Fe–Fe_3S system to 254 GPa. Earth and Planetary Science Letters 464, 135–141.

Morishima, R., Stadel, J., Moore, B., 2010. From planetesimals to terrestrial planets: N-body simulations including the effects of nebular gas and giant planets. Icarus 207, 517–535.

Morrison, R.A., Jackson, J.M., Shurhahn, W., Zhang, D., Greenberg, E., 2018. Equations of state and anisotropy of Fe-Ni-Si alloys. Journal of Geophysical Research: Solid Earth 123, 4647–4675.

Morrison, R.A., Jackson, J.M., Sturhahn, W., Zhao, J., Toellner, T.S., 2019. High pressure thermoe-

lasticity and sound velocities of Fe-Ni-Si alloys. Physics of the Earth and Planetary Interiors 294, 106268.

Mundl, A., Touboul, M., Jackson, M.G., Day, J.M., Kurz, M.D., Lekic, V., Helz, R.T., Walker, R.J., 2017. Tungsten-182 heterogeneity in modern ocean island basalts. Science 356, 66–69.

Murphy, C.A., Jackson, J.M., Sturhahn, W., 2013. Experimental constraints on the thermodynamics and sound velocities of hcp-Fe to core pressures. Journal of Geophysical Research: Solid Earth 118, 1999–2016.

Nakajima, M., Golabek, G.J., Wünnemann, K., Rubie, D.C., Burger, C., Melosh, H.J., Jacobson, S.A., Manske, L., Hull, S.D., 2021. Scaling laws for the geometry of an impact-induced magma ocean. Earth and Planetary Science Letters 568, 116983.

Nakajima, Y., Imada, S., Hirose, K., Komabayashi, T., Ozawa, H., Tateno, S., Tsutsui, S., Kuwayama, Y., Baron, A.Q.R., 2015. Carbon-depleted outer core revealed by sound velocity measurements of liquid iron–carbon alloy. Nature Communications 6, 8942.

Nakajima, Y., Takahashi, E., Sata, N., Nishihara, Y., Hirose, K., Funakoshi, K.I., Ohishi, Y., 2011. Thermoelastic property and high-pressure stability of Fe_7C_3: Implication for iron-carbide in the Earth's core. American Mineralogist 96, 1158–1165.

Nikolaou, A., Katyal, N., Tosi, N., Godolt, M., Grenfell, J.L., Rauer, H., 2019. What factors affect the duration and outgassing of the terrestrial magma ocean? The Astrophysical Journal 875, 11.

Nimmo, F., 2007. Energetics of the Core, in: Schubert, G. (Ed.), Treatise on Geophysics. Elsevier, Oxford. volume 8. chapter 2, pp. 31–65. doi:10.1016/B978-044452748-6.00128-0.

Nimmo, F., 2015. Thermal and Compositional Evolution of the Core, in: Schubert, G. (Ed.), Treatise on Geophysics. Elsevier, Oxford. volume 9. chapter 8, pp. 201–219. doi:10.1016/B978-0-444-53802-4.00160-3.

Nimmo, F., Agnor, C.B., 2006. Isotopic outcomes of N-body accretion simulations: Constraints on equilibration processes during large impacts from Hf/W observations. Earth and Planetary Science Letters 243, 26–43.

Nimmo, F., O'Brien, D.P., Kleine, T., 2010. Tungsten isotopic evolution during late-stage accretion: Constraints on Earth–Moon equilibration. Earth and Planetary Science Letters 292, 363–370.

Nishihara, Y., Doi, S., Tsujino, N., Yamazaki, D., Matsukage, K.N., Tsubokawa, Y., Yoshino, T., Thomson, A.R., Higo, Y., Tange, Y., 2023. Rheology of hexagonal close-packed (hcp) iron. Journal of Geophysical Research: Solid Earth 128, e2022JB026165.

O'Brien, D.P., Morbidelli, A., Levison, H.F., 2006. Terrestrial planet formation with strong dynamical friction. Icarus 184, 39–58.

O'Brien, D.P., Walsh, K.J., Morbidelli, A., Raymond, S.N., Mandell, A.M., 2014. Water delivery and giant impacts in the 'Grand Tack' scenario. Icarus 239, 74–84.

Ohta, K., Hirose, K., 2021. The thermal conductivity of the Earth's core and implications for its thermal and compositional evolution. National Science Review 8, nwaa303.

Ohta, K., Kuwayama, Y., Hirose, K., Shimizu, K., Ohishi, Y., 2016. Experimental determination of the electrical resistivity of iron at Earth's core conditions. Nature 534, 95–98.

Ohtani, E., 2021. Hydration and dehydration in Earth's interior. Annual Review of Earth and Planetary Sciences 49, 253–278.

Ohtani, E., Hirao, N., Kondo, T., Ito, M., Kikegawa, T., 2005. Iron-water reaction at high pressure and temperature, and hydrogen transport into the core. Physics and Chemistry of Minerals 32, 77–82.

Ohtani, E., Shibazaki, Y., Sakai, T., Mibe, K., Fukui, H., Kamada, S., Sakamaki, T., Seto, Y., Tsutsui, S., Baron, A.Q.R., 2013. Sound velocity of hexagonal close-packed iron up to core pressures. Geophysical Research Letters 40, 5089–5094.

Oka, K., Hirose, K., Tagawa, S., Kidokoro, Y., Nakajima, Y., Kuwayama, Y., Morard, G., Coudurier, N., Fiquet, G., 2019. Melting in the Fe-FeO system to 204 GPa: Implications for oxygen in Earth's core. American Mineralogist 104, 1603–1607.

Oka, K., Ikuta, N., Tagawa, S., Hirose, K., Ohishi, Y., 2022. Melting experiments on Fe-O-H and Fe-H: Evidence for eutectic melting in Fe-FeH and implications for hydrogen in the core. Geophysical Research Letters 49, e2022GL099420.

Okuchi, T., 1997. Hydrogen partitioning into molten iron at high pressure: Implications for Earth's core. Science 278, 1781–1784.

Olson, P., Sharp, Z., Garai, S., 2022. Core segregation during pebble accretion. Earth and Planetary Science Letters 587, 117537.

Ono, S., 2013. Equation of state and elasticity of B2-type FeSi: Implications for silicon in the inner core. Physics of the Earth and Planetary Interiors 224, 32–37.

O'Rourke, J.G., Stevenson, D.J., 2016. Powering Earth's dynamo with magnesium precipitation from the core. Nature 529, 387–389.

Ozawa, H., Hirose, K., Tateno, S., Sata, N., Ohishi, Y., 2010. Phase transition boundary between B1 and B8 structures of FeO up to 210 GPa. Physics of the Earth and Planetary Interiors 179, 157–163.

Ozawa, H., Hirose, K., Yonemitsu, K., Ohishi, Y., 2016. High-pressure melting experiments on Fe–Si alloys and implications for silicon as a light element in the core. Earth and Planetary Science Letters 456, 47–54.

Palme, H., O'Neill, H.S.C., 2014. Cosmochemical estimates of mantle composition, in: Carlson, R.W. (Ed.), The Mantle and Core. Elsevier, Oxford. volume 3 of *Treatise on Geochemistry (Second Edition)* of *Treatise on Geochemistry (Second Edition)*. chapter 1, pp. 1–39. doi:10.1016/B978-0-08-095975-7.00201-1. editors-in-chief H. D. Holland and K. K. Turekian.

Pham, T.S., Tkalčić, H., 2023. Up-to-fivefold reverberating waves through the Earth's center and distinctly anisotropic innermost inner core. Nature Communications 14, 754.

Piani, L., Marrocchi, Y., Rigaudier, T., Vacher, L.G., Thomassin, D., Marty, B., 2020. Earth's water may have been inherited from material similar to enstatite chondrite meteorites. Science 369, 1110–1113.

Pierru, R., Pison, L., Mathieu, A., Gardés, E., Garbarino, G., Mezouar, M., Hennet, L., Andrault, D., 2022. Solidus melting of pyrolite and bridgmanite: Implication for the thermochemical state of the Earth's interior. Earth and Planetary Science Letters 595, 117770.

Poirier, J.P., 1994. Light elements in the Earth's outer core: A critical review. Physics of the Earth and Planetary Interiors 85, 319–337. doi:10.1016/0031-9201(94)90120-1.

Pozzo, M., Davies, C., Gubbins, D., Alfè, D., 2013. Transport properties for liquid silicon-oxygen-iron mixtures at Earth's core conditions. Physical Review B 87, 014110.

Pozzo, M., Davies, C., Gubbins, D., Alfè, D., 2014. Thermal and electrical conductivity of solid iron and iron–silicon mixtures at Earth's core conditions. Earth and Planetary Science Letters 393, 159–164.

Pradhan, G.K., Fiquet, G., Siebert, J., Auzende, A.L., Morard, G., Antonangeli, D., Garbarino, G., 2015. Melting of MORB at core–mantle boundary. Earth and Planetary Science Letters 431, 247–255.

Prakapenka, V.B., Kubo, A., Kuznetsov, A., Laskin, A., Shkurikhin, O., Dera, P., Rivers, M.L., Sutton, S.R., 2008. Advanced flat top laser heating system for high pressure research at GSECARS: application to the melting behavior of germanium. High Pressure Research 28, 225–235.

Prescher, C., Dubrovinsky, L., Bykova, E., Kupenko, I., Glazyrin, K., Kantor, A., McCammon, C., Mookherjee, M., Nakajima, Y., Miyajima, N., Sinmyo, R., Cerantola, V., Dubrovinskaia, N., Prakapenka, V., Rüffer, R., Chumakov, A., Hanfland, M., 2015. High Poisson's ratio of Earth's inner core explained by carbon alloying. Nature Geoscience 8, 220–223.

Raymond, S.N., Quinn, T., Lunine, J.I., 2006. High-resolution simulations of the final assembly of Earth-like planets I. Terrestrial accretion and dynamics. Icarus 183, 265–282.

Reagan, M.M., Gleason, A.E., Liu, J., Krawczynski, M.J., Van Orman, J.A., Mao, W.L., 2018. The effect of nickel on the strength of iron nickel alloys: Implications for the Earth's inner core. Physics of the Earth and Planetary Interiors 283, 43–47.

Reno, M.H., 2023. High-energy to ultrahigh-energy neutrino interactions. Annual Review of Nuclear and Particle science 73, 181–204.

Ricolleau, A., Fei, Y., Corgne, A., Siebert, J., Badro, J., 2011. Oxygen and silicon contents of Earth's core from high pressure metal–silicate partitioning experiments. Earth and Planetary Science Letters 310, 409–421.

Righter, K., 2003. Metal–silicate partitioning of siderophile elements and core formation in the early Earth. Annual Review of Earth and Planetary Sciences 31, 135–174.

Righter, K., 2011. Prediction of metal–silicate partition coefficients for siderophile elements: An update and assessment of PT conditions for metal–silicate equilibrium during accretion of the Earth. Earth and Planetary Science Letters 304, 158–167.

Righter, K., Pando, K.M., Danielson, L., Lee, C.T., 2010. Partitioning of Mo, P and other siderophile elements (Cu, Ga, Sn, Ni, Co, Cr, Mn, V, and W) between metal and silicate melt as a function of temperature and silicate melt composition. Earth and Planetary Science Letters 291, 1–9.

Ringwood, A., Kato, T., Hibberson, W., Ware, N., 1990. High-pressure geochemistry of Cr, V and Mn and implications for the origin of the Moon. Nature 347, 174–176.

Ringwood, A.E., 1991. Phase transformations and their bearing on the constitution and dynamics of the mantle. Geochimica et Cosmochimica Acta 55, 2083–2110.

Ritterbex, S., Tsuchiya, T., 2020. Viscosity of hcp iron at Earth's inner core conditions from density functional theory. Scientific Reports 10, 6311.

Robson, A.J.S., Romanowicz, B., 2019. New normal mode constraints on bulk inner core velocities and density. Physics of the Earth and Planetary Interiors 295, 106310.

Rott, C., Taketa, A., Bose, D., 2015. Spectrometry of the Earth using neutrino oscillations. Scientific reports 5, 15225.

Rubie, D.C., Frost, D.J., Mann, U., Asahara, Y., Nimmo, F., Tsuno, K., Kegler, P., Holzheid, A., Palme, H., 2011. Heterogeneous accretion, composition and core–mantle differentiation of the Earth. Earth and Planetary Science Letters 301, 31–42.

Rubie, D.C., Jacobson, S.A., 2016. Mechanisms and geochemical models of core formation, in: Terasaki, H., Fischer, R.A. (Eds.), Deep Earth: Physics and Chemistry of the Lower Mantle and Core. John Wiley & Sons, Inc, Washington DC. volume 217 of *Geophysical Monograph Series* of *Geophysical Monograph Series*. chapter 14, pp. 181–190. doi:10.1002/9781118992487.ch14.

Rubie, D.C., Jacobson, S.A., Morbidelli, A., O'Brien, D.P., Young, E.D., de Vries, J., Nimmo, F., Palme, H., Frost, D.J., 2015a. Accretion and differentiation of the terrestrial planets with implications for the compositions of early-formed Solar System bodies and accretion of water. Icarus 248, 89–108.

Rubie, D.C., Laurenz, V., Jacobson, S.A., Morbidelli, A., Palme, H., Vogel, A.K., Frost, D.J., 2016. Highly siderophile elements were stripped from Earth's mantle by iron sulfide segregation. Science 353, 1141–1144.

Rubie, D.C., Melosh, H.J., Reid, J.E., Liebske, C., Righter, K., 2003. Mechanisms of metal–silicate equilibration in the terrestrial magma ocean. Earth and Planetary Science Letters 205, 239–255.

Rubie, D.C., Nimmo, F., Melosh, H.J., 2015b. Formation of the Earth's core, in: Schubert, G. (Ed.), Treatise on Geophysics. Elsevier, Oxford. volume 9. chapter 3, pp. 43–79. doi:10.1016/B978-0-444-53802-4.00160-3.

Rudge, J.F., Kleine, T., Bourdon, B., 2010. Broad bounds on Earth's accretion and core formation constrained by geochemical models. Nature Geoscience 3, 439–443.

Rudnick, R.L., Gao, S., 2014. Composition of the continental crust, in: Holland, H.D., Turekian, K.K. (Eds.), Treatise on Geochemistry (Second Edition). Elsevier, Oxford, pp. 1–51. doi:10.1016/B978-0-08-095975-7.00301-6.

Russell, S., Irving, J.C., Cottaar, S., 2022. Seismic visibility of melt at the core-mantle boundary from PKKP diffracted waves. Earth and Planetary Science Letters 595, 117768.

Sakai, F., Hirose, K., Morard, G., 2023. Partitioning of silicon and sulfur between solid and liquid iron under core pressures: Constraints on Earth's core composition. Earth and Planetary Science Letters 624, 118449.

Sakai, F., Hirose, K., Umemoto, K., 2022. Melting experiments on Fe-C-O to 200 GPa; liquidus phase constraints on core composition. Geochemical Perspectives Letters 22, 1–4.

Sakairi, T., Sakamaki, T., Ohtani, E., Fukui, H., Kamada, S., Tsutsui, S., Uchiyama, H., Baron, A.Q.R., 2018. Sound velocity measurements of hcp Fe-Si alloy at high pressure and high temperature by inelastic X-ray scattering. American Mineralogist 103, 85–90.

Sakamaki, T., Ohtani, E., Fukui, H., Kamada, S., Takahashi, S., Sakairi, T., Takahata, A., Sakai, T., Tsutsui, S., Ishikawa, D., Shiraishi, R., Seto, Y., Tsuchiya, T., Baron, A.Q.R., 2016. Constraints on Earth's inner core composition inferred from measurements of the sound velocity of hcp-iron in extreme conditions. Science Advances 2, e1500802.

Sammon, L.G., McDonough, W.F., 2022. Quantifying earth's radiogenic heat budget. Earth and Planetary Science Letters 593, 117684.

Samuel, H., 2012. A re-evaluation of metal diapir breakup and equilibration in terrestrial magma oceans. Earth and Planetary Science Letters 313–314, 105–114.

Samuel, H., Drilleau, M., Rivoldini, A., Xu, Z., Huang, Q., Garcia, R.F., Lekić, V., Irving, J.C., Badro, J., Lognonné, P.H., et al., 2023. Geophysical evidence for an enriched molten silicate layer above Mars's core. Nature 622, 712–717.

Schoenberg, R., Kamber, B.S., Collerson, K.D., Eugster, O., 2002. New W-isotope evidence for rapid terrestrial accretion and very early core formation. Geochimica et Cosmochimica Acta 66, 3151–3160.

Shahar, A., Hillgren, V.J., Young, E.D., Fei, Y., Macris, C.A., Deng, L., 2011. High-temperature Si isotope fractionation between iron metal and silicate. Geochimica et Cosmochimica Acta 75, 7688–7697.

Shahar, A., Schauble, E.A., Caracas, R., Gleason, A.E., Reagan, M.M., Xiao, Y., Shu, J., Mao, W., 2016. Pressure-dependent isotopic composition of iron alloys. Science 352, 580–582.

Shahar, A., Ziegler, K., Young, E.D., Ricolleau, A., Schauble, E.A., Fei, Y., 2009. Experimentally determined Si isotope fractionation between silicate and Fe metal and implications for Earth's core formation. Earth and Planetary Science Letters 288, 228–234.

Shannon, M.C., Agee, C.B., 1998. Percolation of core melts at lower mantle conditions. Science 280, 1059–1061.

Shearer, P., Masters, G., 1990. The density and shear velocity contrast at the inner core boundary. Geophysical Journal International 102, 491–498.

Shen, G., Wang, Y., Dewaele, A., Wu, C., Fratanduono, D.E., Eggert, J., Klotz, S., Dziubek, K.F., Loubeyre, P., Fat'yanov, O.V., et al., 2020. Toward an international practical pressure scale: A proposal for an ipps ruby gauge (IPPS-Ruby2020). High Pressure Research 40, 299–314.

Shen, Z., Ai, Y., He, Y., Jiang, M., 2016. Using pre-critical PKiKP–PcP phases to constrain the regional structures of the inner core boundary beneath East Asia. Physics of the Earth and Planetary Interiors 252, 37–48.

Shi, C.Y., Zhang, L., Yang, W., Liu, Y., Wang, J., Meng, Y., Andrews, J.C., Mao, W.L., 2013. Formation of an interconnected network of iron melt at Earth's lower mantle conditions. Nature Geoscience 6, 971–975.

Shi, L., Lu, W., Kagoshima, T., Sano, Y., Gao, Z., Du, Z., Liu, Y., Fei, Y., Li, Y., 2022. Nitrogen isotope evidence for Earth's heterogeneous accretion of volatiles. Nature Communications 13, 4769.

Shibazaki, Y., Ohtani, E., Fukui, H., Sakai, T., Kamada, S., Ishikawa, D., Tsutsui, S., Baron, A.Q.R., Nishitani, N., Hirao, N., Takemura, K., 2012. Sound velocity measurements in dhcp-FeH up to 70 GPa with inelastic X-ray scattering: Implications for the composition of the Earth's core. Earth and Planetary Science Letters 313–314, 79–85.

Shibazaki, Y., Ohtani, E., Terasaki, H., Suzuki, A., Funakoshi, K.I., 2009. Hydrogen partitioning between iron and ringwoodite: Implications for water transport into the Martian core. Earth and Planetary Science Letters 287, 463–470.

Siebert, J., Badro, J., Antonangeli, D., Ryerson, F.J., 2012. Metal–silicate partitioning of Ni and Co in a deep magma ocean. Earth and Planetary Science Letters 321–322, 189–197.

Siebert, J., Badro, J., Antonangeli, D., Ryerson, F.J., 2013. Terrestrial accretion under oxidizing conditions. Science 339, 1194–1197.

Siebert, J., Corgne, A., Ryerson, F.J., 2011. Systematics of metal–silicate partitioning for many siderophile elements applied to Earth's core formation. Geochimica et Cosmochimica Acta 75, 1451–1489.

Siebert, J., Sossi, P.A., Blanchard, I., Mahan, B., Badro, J., Moynier, F., 2018. Chondritic Mn/Na ratio and limited post-nebular volatile loss of the Earth. Earth and Planetary Science Letters 485, 130–139.

Smith, D.E., Zuber, M.T., Phillips, R.J., Solomon, S.C., Hauck, S.A., Lemoine, F.G., Mazarico, E., Neumann, G.A., Peale, S.J., Margot, J.L., et al., 2012. Gravity field and internal structure of Mercury from MESSENGER. Science 336, 214–217.

Solomatov, V.S., 2000. Fluid dynamics of a terrestrial magma ocean, in: Canup, R.M., Righter, K. (Eds.), Origin of the Earth and Moon. University of Arizona Press, pp. 323–338.

Speelmanns, I.M., Schmidt, M.W., Liebske, C., 2019. The almost lithophile character of nitrogen during core formation. Earth and Planetary Science Letters 510, 186–197.

Stacey, J.S., Kramers, J.D., 1975. Approximation of terrestrial lead isotope evolution by a two-stage model. Earth and planetary science letters 26, 207–221.

Stanley, B.D., Hirschmann, M.M., Withers, A.C., 2014. Solubility of C–O–H volatiles in graphite-saturated Martian basalts. Geochimica et Cosmochimica Acta 129, 54–76.

Stixrude, L., Cohen, R.E., 1995. High-pressure elasticity of iron and anisotropy of Earth's inner core. Science 267, 1972–1975.

Suer, T.A., Siebert, J., Remusat, L., Day, J.M.D., Borensztajn, S., Doisneau, B., Fiquet, G., 2021. Reconciling metal–silicate partitioning and late accretion in the Earth. Nature Communications 12, 2913.

Suer, T.A., Siebert, J., Remusat, L., Menguy, N., Fiquet, G., 2017. A sulfur-poor terrestrial core inferred from metal–silicate partitioning experiments. Earth and Planetary Science Letters 469, 84–97.

Sun, S., He, Y., Yang, J., Lin, Y., Li, J., Kim, D.Y., Li, H., Mao, H.k., 2023. Superionic effect and anisotropic texture in Earth's inner core driven by geomagnetic field. Nature Communications 14, 1656.

Sze, E.K., van der Hilst, R.D., 2003. Core mantle boundary topography from short period PcP, PKP, and PKKP data. Physics of the Earth and Planetary Interiors 135, 27–46.

Tagawa, S., Gomi, H., Hirose, K., Ohishi, Y., 2022. High-temperature equation of state of FeH: Implications for hydrogen in Earth's inner core. Geophysical Research Letters 49, e2021GL096260.

Tagawa, S., Sakamoto, N., Hirose, K., Yokoo, S., Hernlund, J., Ohishi, Y., Yurimoto, H., 2021. Experimental evidence for hydrogen incorporation into Earth's core. Nature Communications 12, 2588.

Takafuji, N., Hirose, K., Ono, S., Xu, F., Mitome, M., Bando, Y., 2004. Segregation of core melts by permeable flow in the lower mantle. Earth and Planetary Science Letters 224, 249–257.

Takahashi, S., Ohtani, E., Ikuta, D., Kamada, S., Sakamaki, T., Hirao, N., Ohishi, Y., 2019a. Thermal equation of state of Fe_3C to 327 GPa and carbon in the core. Minerals 9, 744.

Takahashi, S., Ohtani, E., Sakamaki, T., Kamada, S., Fukui, H., Tsutsui, S., Uchiyama, H., Ishikawa, D., Hirao, N., Ohishi, Y., Baron, A.Q.R., 2019b. Sound velocity of Fe_3C at high pressure and high temperature determined by inelastic X-ray scattering. Comptes Rendus Geoscience 351, 190–196.

Tanaka, R., Sakamaki, T., Ohtani, E., Fukui, H., Kamada, S., Suzuki, A., Tsutsui, S., Uchiyama, H., Baron, A.Q.R., 2020. The sound velocity of wüstite at high pressures: implications for low-velocity anomalies at the base of the lower mantle. Progress in Earth and Planetary Science 7, 23.

Tanaka, S., Hamaguchi, H., 1997. Degree one heterogeneity and hemispherical variation of anisotropy in the inner core from PKP(BC)–PKP(DF) times. Journal of Geophysical Research 102, 2925–2938.

Tarduno, J.A., Cottrell, R.D., Bono, R.K., Oda, H., Davis, W.J., Fayek, M., Erve, O.v., Nimmo, F., Huang, W., Thern, E.R., et al., 2020. Paleomagnetism indicates that primary magnetite in zircon records a strong Hadean geodynamo. Proceedings of the National Academy of Sciences 117, 2309–2318.

Tarduno, J.A., Cottrell, R.D., Watkeys, M.K., Hofmann, A., Boubrovine, P.V., Mamajek, E.E., Liu, D., Sibeck, D.G., Neukirch, L.P., Usui, Y., 2010. Geodynamo, solar wind, and magnetopause 3.4 to 3.45 billion years ago. Science 327, 1238–1240.

Tateno, S., Hirose, K., Ohishi, Y., Tatsumi, Y., 2010. The structure of iron in Earth's inner core. Science 330, 359–361.

Tateno, S., Hirose, K., Sinmyo, R., Morard, G., Hirao, N., Ohishi, Y., 2018. Melting experiments on Fe–Si–S alloys to core pressures: Silicon in the core? American Mineralogist 103, 742–748.

Terasaki, H., Frost, D.J., Rubie, D.C., Langenhorst, F., 2005. The effect of oxygen and sulphur on the dihedral angle between Fe–O–S melt and silicate minerals at high pressure: Implications for Martian core formation. Earth and Planetary Science Letters 232, 379–392.

Terasaki, H., Frost, D.J., Rubie, D.C., Langenhorst, F., 2007. Interconnectivity of Fe–O–S liquid in polycrystalline silicate perovskite at lower mantle conditions. Physics of the Earth and Planetary Interiors 161, 170–176.

Terasaki, H., Ohtani, E., Sakai, T., Kamada, S., Asanuma, H., Shibazaki, Y., Hirao, N., Sata, N., Ohishi, Y., Sakamaki, T., Suzuki, A., Funakoshi, K.I., 2012. Stability of Fe–Ni hydride after the reaction between Fe–Ni alloy and hydrous phase (δ-AlOOH) up to 1.2 Mbar: Possibility of H contribution to the core density deficit. Physics of the Earth and Planetary Interiors 194–195, 18–24.

Thibault, Y., Walter, M.J., 1995. The influence of pressure and temperature on the metal-silicate partition coefficients of nickel and cobalt in a model C1 chondrite and implications for metal segregation in a deep magma ocean. Geochimica et Cosmochimica Acta 59, 991–1002.

Thompson, E.C., Chidester, B.A., Fischer, R.A., Myers, G.I., Heinz, D.L., Prakapenka, V.B., Campbell, A.J., 2016. Equation of state of pyrite to 80 GPa and 2400 K. American Mineralogist 101, 1046–1051.

Thompson, E.C., Davis, A.H., Bi, W., Zhao, J., Alp, E.E., Zhang, D., Greenberg, E., Prakapenka, V.B., Campbell, A.J., 2018. High-pressure geophysical properties of *fcc* phase FeH_x. Geochemistry, Geophysics, Geosystems 19, 305–314.

Thompson, S., Komabayashi, T., Breton, H., Suehiro, S., Glazyrin, K., Pakhomova, A., Ohishi, Y., 2020. Compression experiments to 126 GPa and 2500 K and thermal equation of state of Fe_3S: Implications for sulphur in the Earth's core. Earth and Planetary Science Letters 534, 116080.

Thompson, S., Sugimura-Komabayashi, E., Komabayashi, T., McGuire, C., Breton, H., Suehiro, S., Ohishi, Y., 2022. High-pressure melting experiments of Fe_3S and a thermodynamic model of the Fe–S liquids for the Earth's core. Journal of Physics: Condensed Matter 34, 394003.

Tian, F., 2015. Atmospheric escape from Solar System terrestrial planets and exoplanets. Annual Review of Earth and Planetary Sciences 43, 459–476.

Tkalčić, H., Kennett, B.L.N., Cormier, V.F., 2009. On the inner–outer core density contrast from PKiKP/PcP amplitude ratios and uncertainties caused by seismic noise. Geophysical Journal International 179, 425–443.

Tkalčić, H., Phạm, T.S., 2018. Shear properties of Earth's inner core constrained by a detection of J waves in global correlation wavefield. Science 362, 329–332.

Touboul, M., Kleine, T., Bourdon, B., Palme, H., Wieler, R., 2007. Late formation and prolonged differentiation of the Moon inferred from W isotopes in lunar metals. Nature 450, 1206–1209.

Trinquier, A., Birck, J.L., Allegre, C.J., 2007. Widespread ^{54}Cr heterogeneity in the inner solar system. The Astrophysical Journal 655, 1179. doi:10.1086/510360.

Trinquier, A., Elliott, T., Ulfbeck, D., Coath, C., Krot, A.N., Bizzarro, M., 2009. Origin of nucleosynthetic isotope heterogeneity in the solar protoplanetary disk. Science 324, 374–376. doi:10.1126/science.1168221.

Tsuchiya, T., Kawai, K., Wang, X., Ichikawa, H., Dekura, H., 2016. Temperature of the lower mantle and core based on *ab initio* mineral physics data, in: Terasaki, H., Fischer, R.A. (Eds.), Deep Earth: Physics and Chemistry of the Lower Mantle and Core. John Wiley & Sons, Inc, Washington DC. volume 217 of *Geophysical Monograph Series* of *Geophysical Monograph Series*. chapter 2, pp. 13–30. doi:10.1002/9781118992487.ch12.

Tsuno, K., Frost, D.J., Rubie, D.C., 2013. Simultaneous partitioning of silicon and oxygen into the Earth's core during early Earth differentiation. Geophysical Research Letters 40, 66–71.

Turcotte, D.L., Paul, D., White, W.M., 2001. Thorium-uranium systematics require layered mantle convection. Journal of Geophysical Research: Solid Earth 106, 4265–4276. doi:10.1029/2000JB900409.

Turneaure, S.J., Sharma, S.M., Gupta, Y., 2020. Crystal structure and melting of Fe shock compressed to 273 gpa: In situ x-ray diffraction. Physical Review Letters 125, 215702.

Umemoto, K., Hirose, K., 2015. Liquid iron-hydrogen alloys at outer core conditions by first-principles calculations. Geophysical Research Letters 42, 7513–7520.

Upadhyay, A., Kumar, A., Kumar Agarwalla, S., Dighe, A., 2023. Probing the properties of core-mantle boundary using atmospheric neutrino oscillation. International Workshop on Multi-messenger Tomography of the Earth , https://indico.in2p3.fr/event/30001/timetable/.

Valley, J.W., Cavosie, A.J., Ushikubo, T., Reinhard, D.A., Lawrence, D.F., Larson, D.J., Clifton, P.H., Kelly, T.F., Wilde, S.A., Moser, D.E., Spicuzza, M.J., 2014. Hadean age for a post-magma-ocean zircon confirmed by atom-probe tomography. Nature Geoscience 7, 219–223.

Van Elewyck, V., Coelho, J., Kaminski, E., Maderer, L., 2021. Probing the Earth's interior with neutrinos. Europhysics News 52, 19–21.

Van Orman, J.A., 2004. On the viscosity and creep mechanism of Earth's inner core. Geophysical Research Letters 31, L20606.

Vasin, R.N., Kunz, M., Wenk, H.R., Zepeda-Alarcon, E., 2023. Crystallographic texture formation in Fe-9wt%Si alloy during deformation and phase transition at high pressure. Geophysical Journal International 234, 790–806.

Vinet, P., Ferrante, J., Rose, J.H., Smith, J.R., 1987. Compressibility of solids. Journal of Geophysical Research 92, 9319–9325.

Vočadlo, L., Alfè, D., Gillan, M., Wood, I., Brodholt, J., Price, G.D., 2003a. Possible thermal and chemical stabilization of body-centred-cubic iron in the Earth's core. Nature 424, 536–539.

Vočadlo, L., Alfè, D., Gillan, M.J., Price, G.D., 2003b. The properties of iron under core conditions from first principles calculations. Physics of the Earth and Planetary Interiors 140, 101–125.

Vočadlo, L., Dobson, D.P., Wood, I.G., 2009. *Ab initio* calculations of the elasticity of hcp-Fe as a function of temperature at inner-core pressure. Earth and Planetary Science Letters 288, 534–538.

Vogel, A.K., Jennings, E.S., Laurenz, V., Rubie, D.C., Frost, D.J., 2018. The dependence of metal-silicate partitioning of moderately volatile elements on oxygen fugacity and Si contents of Fe metal: Implications for their valence states in silicate liquids. Geochimica et Cosmochimica Acta 237, 275–293.

Vrbek, K., Lamut, J., Marolt, M., Knap, M., 2015. Changes in hydrogen content during steelmaking. Archives of Metallurgy and Materials 60, 295–299.

de Vries, J., Nimmo, F., Melosh, H.J., Jacobson, S.A., Morbidelli, A., Rubie, D.C., 2016. Impact-induced melting during accretion of the Earth. Progress in Earth and Planetary Science 3, 7.

Wade, J., Wood, B.J., 2005. Core formation and the oxidation state of the Earth. Earth and Planetary Science Letters 236, 78–95.

Wakamatsu, T., Ohta, K., Yagi, T., Hirose, K., Ohishi, Y., 2018. Measurements of sound velocity in iron–nickel alloys by femtosecond laser pulses in a diamond anvil cell. Physics and Chemistry of Minerals 45, 589–595.

Walker, R.J., Morgan, J.W., Horan, M.F., 1995. Osmium-187 enrichment in some plumes: evidence for core-mantle interaction? Science 269, 819–822.

Walker, R.J., Mundl-Petermeier, A., Puchtel, I.S., Nicklas, R.W., Hellmann, J.L., Echeverría, L.M., Ludwig, K.D., Bermingham, K.R., Gazel, E., Devitre, C.L., et al., 2023. ^{182}W and ^{187}Os constraints on the origin of siderophile isotopic heterogeneity in the mantle. Geochimica et Cosmochimica Acta 363, 15–39.

Walsh, K.J., Morbidelli, A., Raymond, S.N., O'Brien, D.P., Mandell, A.M., 2011. A low mass for Mars from Jupiter's early gas-driven migration. Nature 475, 206–209. doi:10.1038/nature10201.

Walte, N.P., Rubie, D.C., Bons, P.D., Frost, D.J., 2011. Deformation of a crystalline aggregate with a small percentage of high-dihedral-angle liquid: Implications for core–mantle differentiation during planetary formation. Earth and Planetary Science Letters 305, 124–134.

Wang, L., Fei, Y., 2023. A partially equilibrated initial mantle and core indicated by stress-induced percolative core formation through a bridgmanite matrix. Science Advances 9, eade3010.

Wang, W., Li, Y., Brodholt, J.P., Vočadlo, L., Walter, M.J., Wu, Z., 2021a. Strong shear softening induced by superionic hydrogen in Earth's inner core. Earth and Planetary Science Letters 568, 117014.

Wang, W., Li, Y., Brodholt, J.P., Vočadlo, L., Walter, M.J., Wu, Z., 2021b. Strong shear softening induced by superionic hydrogen in Earth's inner core. Earth and Planetary Science Letters 568, 117014.

Warren, P.H., 2011. Stable-isotopic anomalies and the accretionary assemblage of the Earth and Mars: A subordinate role for carbonaceous chondrites. Earth and Planetary Science Letters 311, 93–100. doi:10.1016/j.epsl.2011.08.047.

Wasson, J.T., Kallemeyn, G.W., 1988. Compositions of chondrites. Philosophical Transactions of the Royal Society of London A: Mathematical, Physical and Engineering Sciences 325, 535–544. doi:10.1098/rsta.1988.0066.

Waszek, L., Deuss, A., 2015. Anomalously strong observations of *PKiKP/PcP* amplitude ratios on a global scale. Journal of Geophysical Research: Solid Earth 120, 5175–5190.

Waszek, L., Irving, J., Pham, T.S., Tkalčić, H., 2023. Seismic insights into Earth's core. Nature Communications 14, 6029.

Watanabe, K., Ohtani, E., Kamada, S., Sakamaki, T., Miyahara, M., Ito, Y., 2014. The abundance of potassium in the Earth's core. Physics of the Earth and Planetary Interiors 237, 65–72. doi:10.1016/j.pepi.2014.10.001.

Weber, R.C., Lin, P.Y., Garnero, E.J., Williams, Q., Lognonné, P., 2011. Seismic detection of the lunar core. science 331, 309–312.

Wenk, H.R., Matthies, S., Hemley, R.J., Mao, H.K., Shu, J., 2000. The plastic deformation of iron at pressures of the Earth's inner core. Nature 405, 1044–1047.

Wetherill, G.W., 1990. Formation of the Earth. Annual Review of Earth and Planetary Sciences 18, 205–256.

Wicks, J.K., Jackson, J.M., Sturhahn, W., Zhang, D., 2017. Sound velocity and density of magnesiowüstites: Implications for ultralow-velocity zone topography. Geophysical Research Letters 44, 2148–2158.

Williams, Q., 2018. The thermal conductivity of Earth's core: A key geophysical parameter's constraints and uncertainties. Annual Review of Earth and Planetary Sciences 46, 47–66.

Wipperfurth, S.A., Guo, M., Šrámek, O., McDonough, W.F., 2018. Earth's chondritic Th/U: Negligible fractionation during accretion, core formation, and crust–mantle differentiation. Earth and Planetary Science Letters 498, 196–202. doi:10.1016/j.epsl.2018.06.029.

Woo, J.M.Y., Brasser, R., Grimm, S.L., Timpe, M.L., Stadel, J., 2022. The terrestrial planet formation paradox inferred from high-resolution N-body simulations. Icarus 371, 114692.

Wood, B.J., Walter, M.J., Wade, J., 2006. Accretion of the Earth and segregation of its core. Nature 44, 825–833.

Yin, Q., Jacobsen, S.B., Yamashita, K., Blichert-Toft, J., Télouk, P., Albarède, F., 2002. A short timescale for terrestrial planet formation from Hf–W chronometry of meteorites. Nature 418, 949–952.

Yoder, C.F., 1995. Astrometric and geodetic properties of Earth and the Solar System. Global Earth Physics: A Handbook of Physical Constants 1, 1.

Yokoo, S., Edmund, E., Morard, G., Baron, M.A., Boccato, S., Decremps, F., Hirose, K., Pakhomova, A., Antonangeli, D., 2023. Composition-dependent thermal equation of state of B2 Fe-Si alloys at high pressure. American Mineralogist 108, 536–542.

Yokoo, S., Hirose, K., Sinmyo, R., Tagawa, S., 2019. Melting experiments on liquidus phase relations in the Fe-S-O ternary system under core pressures. Geophysical Research Letters 46, 5137–5145.

Yoshizaki, T., McDonough, W.F., 2020. The composition of Mars. Geochimica et Cosmochimica Acta 273, 137–162. doi:10.1016/j.gca.2020.01.011.

Yoshizaki, T., McDonough, W.F., 2021. Earth and Mars–distinct inner solar system products. Geochemistry 81, 125746. doi:10.1016/j.chemer.2021.125746.

Young, E.D., Shahar, A., Schlichting, H.E., 2023. Earth shaped by primordial H2 atmospheres. Nature 616, 306–311. doi:10.1038/s41586-023-05823-0.

Yuan, L., Ohtani, E., Ikuta, D., Kamada, S., Tsuchiya, J., Naohisa, H., Ohishi, Y., Suzuki, A., 2018. Chemical reactions between Fe and H_2O up to megabar pressures and implications for water storage in the Earth's mantle and core. Geophysical Research Letters 45, 1330–1338.

Yuan, L., Steinle-Neumann, G., 2020. Strong sequestration of hydrogen into the Earth's core during planetary differentiation. Geophysical Research Letters 47, e2020GL088303.

Yuan, L., Steinle-Neumann, G., 2021. The helium elemental and isotopic compositions of the Earth's core based on *ab initio* simulations. Journal of Geophysical Research: Solid Earth 126, e2021JB023106.

Zambardi, T., Poitrasson, F., Corgne, A., Méheut, M., Quitté, G., Anand, M., 2013. Silicon isotope variations in the inner solar system: Implications for planetary formation, differentiation and composition. Geochimica et Cosmochimica Acta 121, 67–83.

Zhang, Y., Hou, M., Driscoll, P., Salke, N.P., Liu, J., Greenberg, E., Prakapenka, V.B., Lin, J.F., 2021. Transport properties of Fe-Ni-Si alloys at Earth's core conditions: Insight into the viability of thermal and compositional convection. Earth and Planetary Science Letters 553, 116614.

Zhang, Y., Hou, M., Liu, G., Zhang, C., Prakapenka, V.B., Greenberg, E., Fei, Y., Cohen, R., Lin, J.F., 2020. Reconciliation of experiments and theory on transport properties of iron and the geodynamo. Physical Review Letters 125, 078501.

Zhang, Y., Sekine, T., He, H., Yu, Y., Liu, F., Zhang, M., 2014. Shock compression of Fe-Ni-Si system to 280 GPa: Implications for the composition of the Earth's outer core. Geophysical Research Letters 41, 4554–4559.

Zhang, Y., Yin, Q.Z., 2012. Carbon and other light element contents in the Earth's core based on first-principles molecular dynamics. Proceedings of the National Academy of Sciences 109, 19579–19583.

Zhou, T., Tarduno, J.A., Nimmo, F., Cottrell, R.D., Bono, R.K., Ibanez-Mejia, M., Huang, W., Hamilton, M., Kodama, K., Smirnov, A.V., et al., 2022. Early Cambrian renewal of the geodynamo and the origin of inner core structure. Nature Communications 13, 4161.

Ziethe, R., 2009. Settling of metal droplets in a terrestrial magma ocean: On the correction of the Stokes velocity. Planetary and Space Science 57, 306–317.

Zube, N.G., Nimmo, F., Fischer, R.A., Jacobson, S.A., 2019. Constraints on terrestrial planet formation timescales and equilibration processes in the Grand Tack scenario from Hf–W isotopic evolution. Earth and Planetary Science Letters 522, 210–218.

Zurkowski, C.C., Lavina, B., Brauser, N.M., Davis, A.H., Chariton, S., Tkachev, S., Greenberg, E., Prakapenka, V.B., Campbell, A.J., 2022. Pressure-induced $C23$–$C37$ transition and compression behavior of orthorhombic Fe_2S to Earth's core pressures and high temperatures. American Mineralogist 107, 1878–1885.